TEL AVIV UNIVERSITY
RAYMOND AND BEVERLY SACKLER
FACULTY OF EXACT SCIENCES
SCHOOL OF PHYSICS & ASTRONOMY

אוניברסיטת תל-אביב
הפקולטה למדעים מדוייקים
ע"ש ריימונד ובברלי סאקלר
בית הספר לפיסיקה ואסטרונומיה

J/ψ spin-alignment measurement in pp collisions at $\sqrt{s} = 8$ TeV with the ATLAS detector at the LHC

Thesis submitted for the degree “Doctor of Philosophy”

by

Yonathan Munwes

Submitted to the senate of Tel Aviv University

January 19, 2014

Supervisor:

Prof. Erez Etzion

This research was carried out under the supervision of Prof. Erez Etzion

Abstract

The J/ψ and Υ mesons were discovered about forty years ago [1–3]. Since then, the study of $q\bar{q}$ bound states provide significant input for the understanding of quantum chromodynamics (QCD). Although the J/ψ is one of the simplest systems in QCD, it is difficult to describe in detail its production mechanism. A measurement of the J/ψ spin-alignment could shed light on our understanding, and help to distinguish between the different proposed theoretical models.

A precise measurement of the spin-alignment of J/ψs decaying into two muons in pp collisions at a center of mass energy of $\sqrt{s} = 8$ TeV at the LHC is presented. This is the first measurement of this quantity at this energy regime. The current study is based on integrated luminosity of $14 fb^{-1}$ of data collected by the ATLAS experiment in 2012.

As an input for this analysis, a measurement of the production ratio of prompt to non-prompt J/ψ was done. From this measurement we extract the fractions of three physical processes in our signal region, the fraction of prompt J/ψs, non-prompt J/ψs (coming from B-decays) and non-J/ψ background. It was found that the fraction of prompt J/ψs decreases with the increase of p_{T}, where at low p_{T} it starts from 60% and decreases to 30% in the highest p_{T}. The fraction of the non-prompt J/ψ has the opposite behaviour, and the background is below 20% over the whole region.

The measurement of the prompt J/ψ spin-alignment was preformed in the two dimensional angular distribution ($cos\theta^*$ and ϕ^*) in bins of p_{T} and rapidity of the J/ψ. All three spin-alignment parameters, λ_{θ^*}, λ_{ϕ^*} and $\lambda_{\theta^*\phi^*}$ where measured.

The λ_{θ^*} was found to be consistent with zero (with respect to the total uncertainties) in the low p_{T} region, and positive (≈ 0.2) with the increase of J/ψ p_{T}. The other two parameters λ_{ϕ^*} and $\lambda_{\theta^*\phi^*}$ were found to be very small, with small uncertainties, where the λ_{ϕ^*} slightly increases with p_{T}, and $\lambda_{\theta^*\phi^*}$ is consistent with zero in most of the p_{T} spectrum.

The last part of this thesis describes the development of the small Thin Gap Chambers (sTGC) for the Phase-I ATLAS upgrade. It was developed and proposed to replace the small wheel of the ATLAS detector. This technology is based on the TGCs that are operated today in the ATLAS Muon Spectrometer and are used for triggering on high p_{T} muons in the ATLAS endcaps region. The new detector design was approved by the collaboration this year. This new detectors design will allow to maintain the full trigger acceptance and precise muon tracking at the highest LHC luminosities expected after the LHC upgrades.

Preface

The work presented in this thesis is composed of two parts. The first part is the study of the prompt J/ψ spin-alignment and the production ratio of prompt to non-prompt J/ψ in pp collisions in the ATLAS experiment at the LHC. For this measurement, I am examining the two dimensional angular distribution of the muon decay products coming from prompt and non-prompt J/ψs.

This measurement is very challenging and requires a very good understanding of various detector effects. This work is part of the studies preformed in the ATLAS BPhysics group. This Analysis lead by me, but for some studies the work was a joint effort. The main analyses that are described in chapter 4 - 8 performed by me, where the trigger efficiency study was done with Ben Weinert based on previous work of Yi Yang. The reconstruction efficiency study was preformed by Dr. Darren Price and Stefanos Leontsinis, and was validated by me. This analysis effort was started even before ATLAS took data, it was lead by Dr. Jonatan Ginzburg and Nir Amram under the supervision of Prof. Erez Etzion.

The second part is about the development of new Thin Gap Chamber (TGC) detector for the super LHC (sLHC). This work is done as part of a collaboration of three institutes in Israel (Tel-Aviv University, Weizmann Institute and the Technion-Israel Institute). I joined this project in 2008, and participated in several test beams and high radiation tests that are described in this thesis. I have designed and implemented the data acquisition, the online monitoring and performed various physics analyses in those tests.

Yonathan Munwes

Acknowledgements

I would like to express my deep gratitude to people who advised, supported and helped me to accomplish this work.

First and foremost I would like to thank my supervisor Prof. Erez Etzion. Erez accepted me as an M.Sc. student and guided me since. He taught me a lot, not only in work related subjects. His door was always open for question and he always made sure that I had all the necessary means to conduct the research. Erez is a role model, he demonstrates how to work effectively and at the same time keep an admirable healthy family life. He is the calmest and most optimistic person I know and it was a great pleasure to be his student.

I would like to thank Prof. Halina Abramowicz. I worked with Halina during the four years I was the head instructor of the physics laboratory for first year undergraduates. Halina has extensive knowledge in physics and data analysis and it was great opportunity to learn from her. She always gave me the feeling I'm welcome at her office and showed great interest in my work, my private life and family. In addition I want to thank her for all the good advises she gave me, not mentioning her help in finding me my next position.

Prof. Giora Mikenberg from Weizmann Institute. Giora is the group leader of the sTGC project. I had the chance to participate in several experiments with Giora and managed to learn from his rich experience in detectors and high energy physics. I had the opportunity to work closely with him on the physics analysis in the different test beams, and he always pushed and encourage me to work hard and to get better results.

Dr. Gideon Bella, who always find the time and patience to answer my endless questions. Gideon was involved in both parts of my thesis (ATLAS analysis and the detector R&D) and helped me to solve all kind of problems I have encounter during my work.

I want to give a special thank to Dr. Yan Benhammou. Yan, throughout my PhD, was like a second supervisor, I worked with him on a daily basis in the sTGC project and learned from him a lot. From Yan I gained all my knowledge in data acquisition, he gave me the tools for self-learning (RTFM) from the first moment we started working together. Yan always gave me the confidence to do things I was afraid to do (only cowards are afraid). He also taught me that sleeping is a waste of time and we can sleep on the plane on the way back home.

Meny Ben Moshe, for taking care of all of us, and making the lab (office) a second home. Meny always put your interest in before his own and helped in every aspect that was possible. He is one of the main reasons that our group feels like family. I spend a lot of time with Meny abroad, and will never forget the endless laughter we shared in those trips.

Special thanks are also given to the Tel Aviv University high energy physics group staff, Prof. Avner soffer and Prof. Gideon Alexander, for the fruitful discussions in the office and in the group meetings. Thanks to students with whom I shared an office in the past five years, for the knowledge we share, the moral support and the good friendship. Especially, Avi Gershon, Nimrod Taiblum, Dr. Nir Guttman, Dr. Noam Tal-Hod, Dr. Yiftah Sliver, Adi Ashkenazi, Daphna Peimer, Rotem Gorodeisky and Itamar Levy. I would also like to thank the people who worked with me in the Physics laboratory for first year undergraduate, Kobi Barkan, Mike Karpove, Lavi Apple and Ziv Rotman, for all the help to make the course better.

The ATLAS BPhsyics analysis team and especially Prof. Sandro Palestini (CERN), who was the group convener until the end of 2013 and to Dr. Darren Price (University of Manchester), the Onia sub-group convener. Dr. James Catmore (University of Oslo), Dr. Vato Kartvelishvili (Lancaster University), James William Walder (Lancaster University), Andrew Stephen Chisholm(University of Birmingham), for all the help in different aspect of the analysis. Special thanks to Nir Amram who started the effort for this measurement and pass me the first knowledge in the different analysis tools.

To all my Colleagues in the sTGC project, especially Mr. Meir Shoa, Mr. Boris Yankovski, Dr. Dimitry Milstien, Dr. Amit Klier and Mr. Nachman Lupu for the effort to make the project a success. Special thanks to Dr. Vladimir Smakhtin from Weizmann Institute. Vladimir has an extensive knowledge in physics and detectors. I shared a lot of working hours with him at the lab and at the different experiments. It was amazing to see the way he thinks, even more amazing the way he tackle Physics problems, the systematic manner, and how he solves everything in five minutes.

The management, the senior academic staff, the secretariat and staff of the School of physics and astronomy in Tel Aviv University, for all the professional and cheerful help over the ten happy years I have spent at the University.

I would like to thank my wife Sagit, my daughter Emma and my mother Lili for all the support during all these years. Sagit started this journey with me, more than ten years ago.

She gave me all the support and space in order to succeed. Sagit always encourages me to be better and I'm thankful to her for that. I couldn't done it without her.

Finally, I want to dedicate this work to my father who passed away in the middle of this work. Since I was a little boy he always believed in me and encouraged me to push my limits. He showed great interest in every field or hobby I chose and learned every detail in it. He always made me feel he was proud of me and I'm grateful I had such a father.

Contents

Chapter 1.

Introduction

The J/ψ meson is a bound state of a charm quark and a charm antiquark ($c\bar{c}$) known as charmonium. It is the first excited state of charmonium with a rest mass of 3096.9 GeV and a mean life time of $7.2 \times 10^{-21} s$. The J/ψ was discovered independently by two research groups, one at Stanford Linear Accelerator Center, and one at Brookhaven National Laboratory [1, 2]. The discovery was announced on 11 November 1974.

Our present understanding of quarkonium production is rather limited, despite the multitude of experimental data accumulates over more than 30 years. At the mid 1990's CDF measured the p_{T} differential J/ψ direct production cross-section to be around 50 times higher than the available expectations, based on leading order calculations made in the scope of the Color Singlet Model (CSM). The non-relativistic QCD (NRQCD) [4], where quarkonium can produce as quark pairs, succeeded in describing the measurements, however these calculations depend on non-pertubative parameters (long distance color octet matrix elements) which have been freely adjusted to the data, thereby decreasing the impact of the resulting agreement between data and calculations. More recently, calculations of next-to-leading-order (NLO) QCD corrections to colour-singlet quarkonium production showed an important increase of the high-p_{T} rate, significantly decreasing the colour-octet component needed to reproduce the quarkonium production cross-sections measured at the Tevatron [5]. Higher order corrections to CSM (next-to-next-to-leading-order) compared with the latest ATLAS results (see Figure 1.1) showed a vast improvement compared to the NLO, but still not describing well the data, especially at higher momentum.

It is clear that differential cross-section are insufficient information to ensure further progress in our understanding of quarkonium production. Experimental studies of the polarization of $J^{PC} = 1^{--}$ quarkonium states, which decay into lepton pairs will provide useful complementary information.

Different theoretical approaches lead to very different expected polarizations:

- NRQCD dominated by color-octet predict that at higher p_T, direct J/ψs are produced almost fully transversely polarized $J_Z = \pm 1$ (with respect to their own momentum direction-the helicity frame)
- NLO calculation of color-singlet predict that these states show a strong longitudinal polarization component $J_Z = 0$

From experimentalist's perspective it should be relatively straightforward to discriminate between these two different theoretical predictions, But surprisingly this is not the case.

The lack of a consistent description of the spin-alignment represents today's biggest uncertainty in the simulation of the LHC quarkonium production measurements and is the largest contribution to the systematic error affecting the measurement of quarkonium production cross-sections and kinematic distribution. In Figure 1.1 the J/ψ prompt cross-section from the ATLAS experiment is shown. This measurement was done using the early data of 2010. The yellow bands around the data points represent the spin-alignment uncertainty.

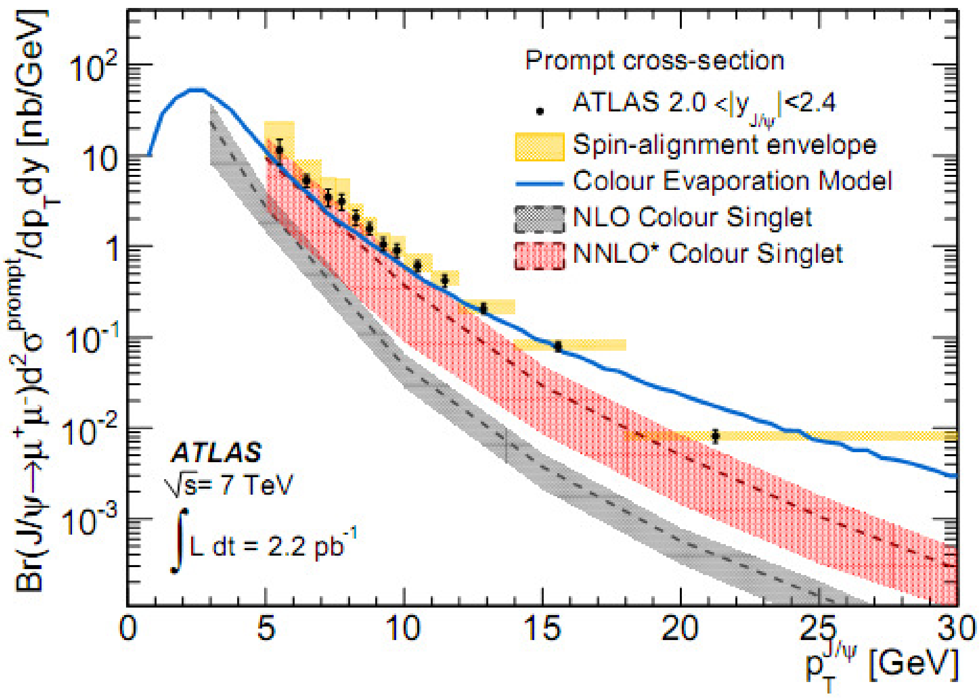

Figure 1.1.: Prompt J/ψ cross-section as a function of J/ψ transverse momentum. Overlaid is a band representing the variation of the result under various spin-alignment scenarios representing a theoretical uncertainty on the prompt component. Predictions from NLO and $NNLO^*$ calculations, and the Colour Evaporation Model are overlaid.

The work presented in this thesis summarizes a five-year effort concentrated around the measurement of the spin-alignment of prompt J/ψs in pp collisions in the ATLAS experiment at the Large Hadron Collider at CERN. This research was part of the studies preformed at a sub group of the ATLAS Physics group. For this measurement we examine the two dimensional angular distributions of the muon decay products coming from prompt and non-prompt J/ψ's. This measurement was very challenging and required a very good understanding of various detector effects. It is the first J/ψ spin-alignment measurement done with a center of mass (CM) energy of 8 TeV.

In chapter 2 we will give a summary of the different theoretical models for the production of the J/ψ that are relevant to hadron colliders, and will define the different reference frames for the measurement of the J/ψ spin-alignment.

The main analysis, which is described in details in chapter 6 and in the appendices, is based on dataset of an integrated luminosity of 14.1 fb^{-1}, corresponding to the 2012 data taking (from period C6) with pp collisions at 8 TeV center of mass energy. The full description of the dataset and the event selection is discussed in chapter 4. Chapter 3 describes the LHC machine and the ATLAS detector. In this chapter we give emphasis on the Inner detector, muon spectrometer and the muon trigger system which are most relevant for this thesis.

The analysis was preformed on the prompt J/ψ candidates. For this, analysis of the prompt/non-prompt J/ψ fraction was preformed (chapter 5). In order to distinguish and separate the prompt J/ψs from the entire sample, that include sources of non-prompt J/ψs and non-J/ψ events, a simultaneous fit on mass and life-time was preformed. The full details and procedure of how to identify the different sources are explained.

Different aspects of the main measurement are described in chapter 6. The bare outcome of this analysis is shown in Figures 7.8, 7.9, and 7.10, where the final values of the three spin-alignment parameters ($\lambda_{\theta^*}, \lambda_{\phi^*}, \lambda_{\theta^*\phi^*}$) are shown as a function of the $p_{\mathrm{T}}(J/\psi)$. The results are summarized and discussed in chapter 8.

The appendices shed more light on the analysis process providing detailed description of the muon reconstruction and trigger efficiencies that are used in the main analysis. In addition complementary plots and tabels for the different chapters are added as appendices.

During my PhD I was involved in the development of the new small Thin Gap Chamber (sTGC) planned for the 2018 LHC upgrade. This work was done as part of a collaboration of three institutes in Israel (Tel-Aviv University, Weizmann Institute and the Technion-Israel

Institute). Chapter 9 review this project and shows the results from various tests we conducted during the past five years.

My analysis code is largely available under my private svn repository [6], except for files that contain ATLAS data or full simulation results.

Chapter 2.

Theory

2.1. Introduction

A particle is produced in a certain superposition of elementary mechanisms [7]. It is said to be polarized if it is observed in a preferred state belonging to a definite subset of the possible eigenstates of the angular momentum component, J_Z, along a characteristic quantization axis. This is a direct consequence of angular momentum conservation and basic symmetries of the electromagnetic and strong interactions. Figure 2.1 shows various leading order diagrams of elementary production processes giving rise to different polarization scenarios.

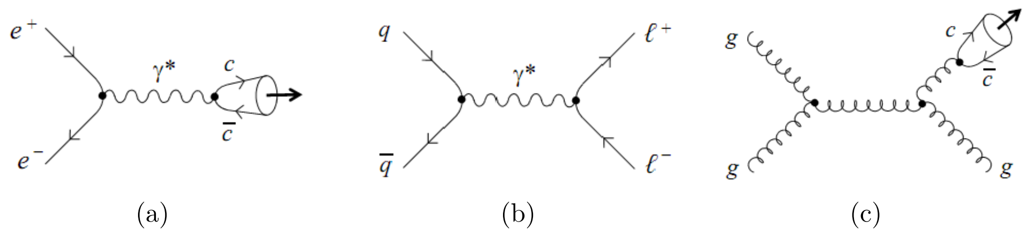

Figure 2.1.: Leading order diagrams for production mechanisms giving rise to observable polarizations [7]. (a) vector quarkonium production in electron-positron annihilation (b) Drell-Yan production in quark4-antiquark annihilation (c) quarkonium production by gloun fragmentation to color octet $c\bar{c}$.

In Figure 2.1(a) a vector quarkonium is produced via intermediate photon from annihilation of electron-positron. This quarkonium is polarized because of helicity conservation, a general property of QED in the relativistic limit. The dynamic of the coupling between the electron and the photon is of the form $\bar{u}\gamma^\mu u = \bar{u}_L\gamma^\mu u_L + \bar{u}_R\gamma^\mu u_R$, where γ^μ are the dirac matrices, u is the electron spinor and L,R represent left-handed or right handed chiral components. In the relativistic limit, the fermions are assumed to have zero mass, that is why their momenta direction cannot be reversed by any Lorenz transformation, hence left/right-handed chiral component are the eigenstates of the helicity operator $h = \vec{S} \cdot \vec{p}\,|\vec{p}|$. In this case, chirality conservation become helicity conservation. In our example (Figure 2.1(a)) this rule implies that the electron and positron must have opposite helicities, since the photon has zero helicity. Because in the laboratory frame their momenta is opposite, their spins must be parallel, and due to angular momentum conservation the produced quarkonium must have angular momentum along the direction of the colliding leptons ($J_Z = \pm 1$).

The same reasoning holds for the production of Drell-Yan lepton pairs in quark-antiquark annihilation (see Figure 2.1(b)): the quark and antiquark, in the limit of vanishing masses, must annihilate with opposite helicities, resulting in a dilepton state having $J_z = -1$ along the direction of their relative velocity.

The last process in Figure 2.1(c) is the main production process in hadron colliders at very high transverse momentum(p_{T}). In this case, transitions of the gluon to other allowed color and angular momentum configurations, containing the $c\bar{c}$ in either a color-singlet or a color-octet state, with spin $S = 0, 1$ and angular momentum $L = 0, 1, 2, ...$, as well as additional gluons, are more and more suppressed with increasing p_{T}. The fragmenting gluon is believed to be on shell (up to a small correction) and have, therefore, helicity ± 1. This property is inherited by the $c\bar{c}[^3S^{(8)}]_1]$ state and remains intact during the non-perturbative transition to the color-neutral physical state, via soft-gluon emission. In this model, the observed charmonium has angular momentum component $J_Z = -1$, but this time not along the direction of the beam (like in the previous case), but along its own flight direction. In the following sections we will describe the different theoretical models and the different spin-alignment frame of references.

2.2. Quantum Chromodynamics introduction

Quantum Chromodynamics (QCD) is the theory of strong interactions. It is formulated in terms of elementary fields, quarks and gluons, which their interactions obey the principles of relativistic Quantum Field Theory (QFT), with non-Abelian gauge invariance SU(3). Quarks and anti-quarks exist in three different color state, they transform respectively under the three dimensional 3 and $\bar{3}$ representations of the gauge group SU(3). The gauge bosons of the theory are the gluons. Gluons are color octets, transforming under the eight-dimensional representation of SU(3). The gluons are massless and they interact with the quarks and among themselves. The quarks come in six flavors and have a wide range of masses, varying from a few MeV for the up and down quarks to 175 GeV for the top quark. Up, down and strange are considered the light quarks while the charm, bottom and top quarks are considered the heavy quarks. Quarks appear as point-like at the scales of $\sim 10^{-18}$m, the current limit of experimental resolutions.

Quarks and gluons were never observed as free particles, this phenomena is due to color confinement hypothesis which states that naturally occurring states can only exist in colorless states. That is why for example $q\bar{q}$ (named mesons) and qqq (named baryons) are allowed combinations, because the individual quark colors may combine to form a color singlet state, but qq states are not allowed states.

The strong coupling constant, α_s, represents the strength of quark-gluon and gluon-gluon interactions, analogous to the α coupling constant for QED. It depends on the transverse momentum of the process, a property named the running coupling. When the interactions are in the energy regime lower than 1 GeV the coupling constant is so strong that the petrubative theory brakes. At high energies the coupling constant decreases, becoming small enough for petrubative theory to be applied. The decrease in α_s implies that in the limit of high energies quark will become free particles, what is known as "Asymptotic freedom".

The binding force in QCD systems is so strong such that even strong energy invested in a collision can not break the hadrons into free quarks, but instead they will bound to quarks from the color field and produce other hadrons. This process of production of $q\bar{q}$ pairs in strong interactions is the heart of the model of hadron production.

2.3. Quarkonium production

During the past few years there were several theoretical attempts to build models which will describe the production mechanism of the quarkonium states. None of them succeeded to perfectly describe the experimental measurements. This is obviously one of our main motivation to further explore the characteristics of the quarkonium states. In the following subsections we briefly describe the various models and the main differences between them with emphasis on the experimental aspects.

2.3.1. The Color Singlet Model

The Color Singlet Model In the Color Singlet Model (CSM) [8, 9], it is assumed that the $Q\bar{Q}$ pair evolves into the quarkonium is in a color-singlet state and that it has the same spin and angular-momentum quantum numbers as the quarkonium. In the CSM, the production rate for each quarkonium state is related to the absolute values of the color-singlet $Q\bar{Q}$ wave function and its derivatives, evaluated at zero $Q\bar{Q}$ separation. These quantities can be extracted by comparing theoretical expressions for quarkonium decay rate in the CSM with experimental measurements. The CSM was successful in predicting the quarkonium production rate at low energy regime. In the higher energy regime, a large corrections to the next-to-leading order (NLO) and next-to-next-to-leading order (NNLO) in α_s has to be made in order to fit the quarkonium cross-section. Results from ATLAS experiment [10] showed that the CSM prediction for NNLO significantly improve the p_T dependence and normalization of prompt J/ψ production compared to NLO, and a vast improvement over earlier LO predictions. Although it is clear that these predictions still not fully describe the production mechanism of prompt J/ψ, particularly at the highest transverse momenta.

2.3.2. The Color Evaporation Model

In the Color Evaporation Model (CEM) [11] it is assumed that every produced $Q\bar{Q}$ pair can evolve into a quarkonium if it has an invariant mass that is less than the threshold for producing a pair of open flavor heavy mesons. It is further assumed that the nonperturbative probability for the $Q\bar{Q}$ pair to evolve into a quarkonium state H is given by a constant F_H that is energy-momentum and process independent. Once F_H has been fixed by comparison with the measured total cross-section for the production of the quarkonium H, the CEM can predict, with no additional free parameters, the momentum distribution of quarkonium production rate.

2.3.3. The NRQCD factorization approach

Nonrelativistic QCD (NRQCD [4]) is an effective theory of QCD that reproduces all the QCD dynamics at momentum scales of the order of $m_Q v$ and smaller (m_Q is the mass of the heavy quark and v is the relative quark velocity in the bound state) , which treats quarkonium as an approximately nonrelativistic system. NRQCD makes systematic corrections to this approximation using an expansion series in v, the velocity of the heavy quark in the quarkonium rest frame. When applied to production, this implies that $Q\bar{Q}$ pairs produced with one set of quantum numbers can evolve into a quarkonium state with different quantum numbers, by emitting low energy gluons. The NRQCD factorization approach expresses the probability for a $Q\bar{Q}$ pair to evolve into a quarkonium in terms of matrix elements of the NRQCD operators. The inclusive cross-section for direct production of quarkonium state H is:

$$\sigma(H) = \sum_n \sigma_n(\Lambda)\langle O_n^H(\Lambda)\rangle \tag{2.3.1}$$

Λ represents the ultraviolet cutoff of the effective theory, σ_n are expansions in powers of v of the cross-sections to produce a $Q\bar{Q}$ pair in the color, spin and orbital angular momentum state n. The σ_n are convolutions of the parton distribution functions. The matrix elements $\langle O_n^H(\Lambda)\rangle$ are vacuum expectation values of fermions operators in NRQCD. Eq. 2.3.1 represents both processes in which the $Q\bar{Q}$ pair produced in the color singlet state and the color octet state. The NRQCD factorization formula for heavy quarkonium production depends on an infinite number of unknown matrix elements (unlike of the CSM and the CEM expressions). However the sum in Eq. 2.3.1 can be expressed in powers of v so that the equation becomes a double expansion in powers of v and α_s. Therefore the sum is being cutoff at fixed order in v and only a few matrix elements contribute to the sum. Although the application of NRQCD factorization to heavy quarkonium production processes has had many successes, there remain a number of discrepancies between its predictions and the experimental measurements. The main failure of NRQCD is in predicting the angular distribution for the quarkonium decay P_T dependence, which can be interpreted as a failure to predict the Quarkonium longitudinal polarization [12].

2.4. J/ψ spin-alignment

The polarization of a particle with spin is determined by its spin density matrix [13], which defines the amplitude when the particles has mixing spin states. The J/ψ is spin one vector, massive particle with three spin eigenvalues, ± 1,0 states. The spin density matrix for a massive vector boson is denoted as $\rho_{\lambda\lambda'}$, where $\lambda = \pm 1, 0$. $\rho_{\lambda\lambda'}$ is proportional to the polarized production cross-section $\sigma_{\lambda\lambda'}$:

$$\rho_{\lambda\lambda'} \propto \sigma_{\lambda\lambda'} = A[\psi(\lambda)]A^*[\psi(\lambda')] \tag{2.4.1}$$

where $A[\psi(\lambda)]$ is the production amplitude for a ψ produced with helicity λ. This means that the J/ψ polarization is determined by its production mechanism. Because the spin density matrix is Hermitian:

$$\rho_{-1,-1} + \rho_{+1,+1} + \rho_{0,0} = 1 \tag{2.4.2}$$

The following constrains can be obtained due to conservation of parity (in the dimuon decay channel):

$$\rho_{-1,-1} = \rho_{+1,+1} \tag{2.4.3}$$
$$\rho_{-1,+1} = \rho_{+1,-1} \tag{2.4.4}$$
$$\rho_{-1,0} = -\rho_{+1,0} \tag{2.4.5}$$
$$\rho_{0,-1} = -\rho_{0,+1} \tag{2.4.6}$$

so the number of independent matrix elements reduces to four: $\rho_{-1,-1}$, $\rho_{1,-1}$, $Re[\rho_{0,1}]$ and $Im[\rho_{0,1}]$.

In the channel $J/\psi \to \mu^+\mu^-$ the differential cross-section as function of the muons angular variables in the rest frame of the J/ψ can be expressed by:

$$\frac{d^2\sigma}{dcos\theta^* d\phi^*} = \frac{1}{1+\lambda_{\theta^*}/3}(1 + \lambda_{\theta^*} cos^2\theta^* + \lambda_{\phi^*} sin^2\theta^* cos2\phi^* + \lambda_{\theta^*\phi^*} sin2\theta^* cos\phi^*) \tag{2.4.7}$$

The $cos\theta^*$ and ϕ^* are the muons angular variables, where θ^* is the angle defined with respect to the z-axis and ϕ^* is the azimuthal angle and depend on the coordinate system. The λ_i where $i = \theta^*, \phi^*, \theta^*\phi^*$ are called the polarization parameters. There is a direct relation between the λ_i parameters and the spin density matrix:

$$\lambda_{\theta^*} = \frac{\rho_{+1,+1} - \rho_{0,0}}{\rho_{+1,+1} + \rho_{0,0}} \tag{2.4.8}$$
$$\lambda_{\phi^*} = \frac{2\rho_{+1,-1}}{\rho_{+1,+1} + \rho_{0,0}} \tag{2.4.9}$$
$$\lambda_{\theta^*\phi^*} = \frac{\sqrt{2}\rho_{+1,0}}{\rho_{+1,+1} + \rho_{0,0}} \tag{2.4.10}$$

Therefore, by measuring the angular distribution of the decaying muons, we can extract the spin-alignment state of the J/ψ and understand its production mechanism. For example a J/ψ that was produced in a pure helicity 0 state, which means $\rho_{0,0} = 1$, its polarization parameters will be $\lambda_i = (-1, 0, 0)$, which is called fully longitudinal polarization. If the helicity states were pure ± 1 the polarization parameters were $\lambda_i = (1, 0, 0)$, which is called fully transverse polarization. In the case the three parameters are equal to zero, the J/ψ is unpolarized, which means that the muons will decay isotropically in the rest frame of the the J/ψ and $cos\theta^* - \phi^*$ distribution will be uniform.

The measurement of the dimuon angular distribution require the choice of a coordinate system, with respect to which the momentum of one of the two decay products is expressed in spherical coordinates. In inclusive quarkonium measurements, the axes of the coordinate system are fixed with respect to the physical reference provided by the directions of the two colliding beams as seen from the quarkonium rest frame. Figure 2.2 illustrates the definitions of the polar angle θ^* and the azimuthal angle ϕ^*. The angle θ^* is determined by the direction of one of the two decay products (in our analysis with respect to the positive muon) with respect to the chosen polar axis, and the azimuthal angle ϕ^* is measured with respect to the plane containing the momentua of the colliding beams (”production plane”).

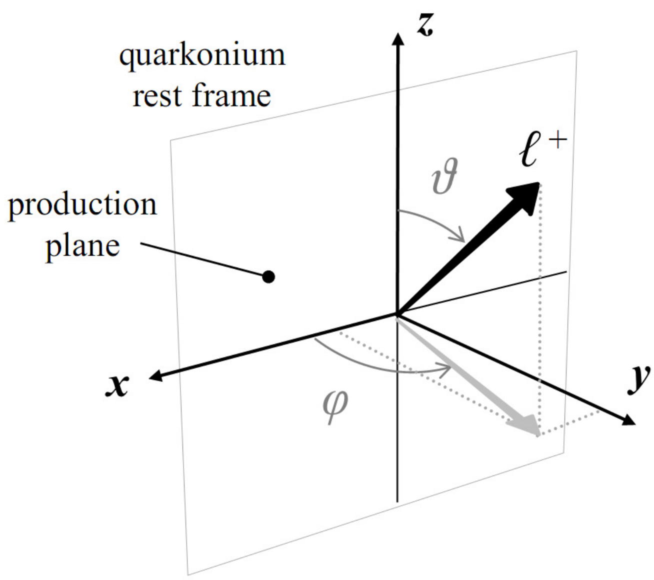

Figure 2.2.: The coordinate system for the measurement of dimuon decay angular distribution in the J/ψ rest frame. The y-axis is prepnedicular to the production plane.

Historically the measurements of the quarkonium decay were preformed in three different definitions of the polar axis. The Gottfried-Jackson frame (GJ) [14] defines the polar axis in the direction of the momentum of one of the two colliding beam. The helicity frame (HX) defines the polar axis as the opposite of the direction of motion from the interaction point, i.e. the flight direction of the quarkonium itself in the center of mass of the colliding beams, and the Collins-Soper frame [15] defines the axis as the bisector of the angle between one beam and the opposite of the other beam. These definitions can be seen in Figure 2.3.

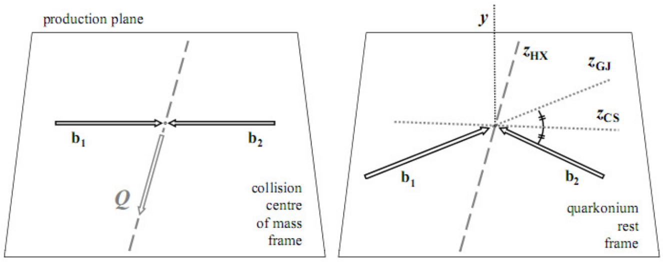

Figure 2.3.: Illustration of the three definitions of the polarization axis z with respect to the directions of motion of the colliding beams (b_1, b_2) and the quarkonium (Q), where CS stand for Collins-soper, GJ for Gottfried-Jackson and HX is for helicity.

From Figure 2.3 it can be seen that the different frames are related by a pure rotation around the y axis, which is common for the three frames. In the limit of zero transverse momentum all frames coincide and when the transverse momentum increases the CS axis is rotated by 90 degrees from the HX axis. We can transform from CS to the HX frame (or vise versa) using the following formulas:

$$\lambda'_{\theta^*} = \frac{\lambda_{\theta^*} - 3\Lambda}{1+\Lambda} \tag{2.4.11}$$

$$\lambda'_{\phi^*} = \frac{\lambda_{\phi^*} + \Lambda}{1+\Lambda} \tag{2.4.12}$$

$$\lambda'_{\theta^*\phi^*} = \frac{\lambda_{\theta^*\phi^*} cos2\delta - \frac{1}{2}(\lambda_{\theta^*} - \lambda_{\phi^*}) sin2\delta}{1+\Lambda} \tag{2.4.13}$$

where

$$\Lambda = \frac{1}{2}(\lambda_{\theta^*} - \lambda_{\phi^*}) sin^2\delta - \frac{1}{2}\lambda_{\theta^*\phi^*} sin2\delta \tag{2.4.14}$$

and δ is the angle between the z-axis of the two frames.

This expression for a general transformation between frames, implies the existence of an invariant quantity, definable in terms of the different polarization parameters in the following equivalent forms:

$$F_{c_i} = \frac{(3+\lambda_{\theta^*}) + c_1(1-\lambda_{\phi^*})}{c_2(3+\lambda_{\theta^*}) + c_3(1-\lambda_{\phi^*})} \tag{2.4.15}$$

where c_i are arbitrary constant numbers. The most common one is with the choice of $c_1 = -3, c_2 = 0, c_3 = 1$ that give us the invariant parameter:

$$\tilde{\lambda} \equiv F_{-3,0,1} = \frac{\lambda_{\theta^*} + 3\lambda_{\phi^*}}{1 - \lambda_{\theta^*}} \tag{2.4.16}$$

The determination of an invariant quantity is more immune to extrinsic kinematic dependencies induced by the observation perspective and is, therefore, less acceptance dependent than the standard anisotropy parameters $\lambda_{\theta^*}, \lambda_{\phi^*}$ and $\lambda_{\theta^*\phi^*}$.

Chapter 3.

Experimental setup

The Large Hadron Collider [16] (LHC) at CERN, resides in a circular tunnel of 27 km long. The tunnel is buried 50 to 175 m underground and it passes below the Swiss and French borders. It is the world's most powerful accelerator for Particle Physics research. The machine started running during 2009 and after a short commissioning period it started colliding proton-proton beams during December 2009. That year the LHC collected a total integrated luminosity of $20\mu b^{-1}$ and the maximum energy was $\sqrt{s}$=2.38 TeV. The LHC operated at 3.5 TeV per beam in 2010 and 2011 and each of the two big experiments collected integrated luminosities of 5 fb^{-1}. During 2012 the LHC operated at 4 TeV per beam and collected total of 23.3 fb^{-1} of data, for each experiment.

3.1. The LHC machine

The LHC is designed to collide protons at a center of mass energy of 14 TeV. Before particles are injected into the LHC they go through several acceleration stages. The first is the linear particle accelerator (LINAC 2) generating 50 MeV protons. The protons are injected into the Proton Synchrotron Booster (PSB) which accelerate the particles to 1.4 GeV. After that the particles are injected into the Proton Synchrotron (PS) where they are accelerated to 26 GeV, afterward they injected to the Super Proton Synchrotron (SPS) which increases their energy to 450 GeV. The particles injected to the LHC into two parallel rings and after ramping up to the desired energy the beams are squeezed and directed to collisions in the dedicated LHC experiments (see Figure 3.1).

The LHC has two high luminosity experiments, ATLAS [17] and CMS [18]. There are also two low luminosity experiments: LHCb [19] for B-physics, and TOTEM [20] for the detection of protons from elastic scattering at small angles. In addition to the proton beams, the LHC also operates with heavy ion beams and for that it uses one dedicated heavy ion experiment, ALICE [21].

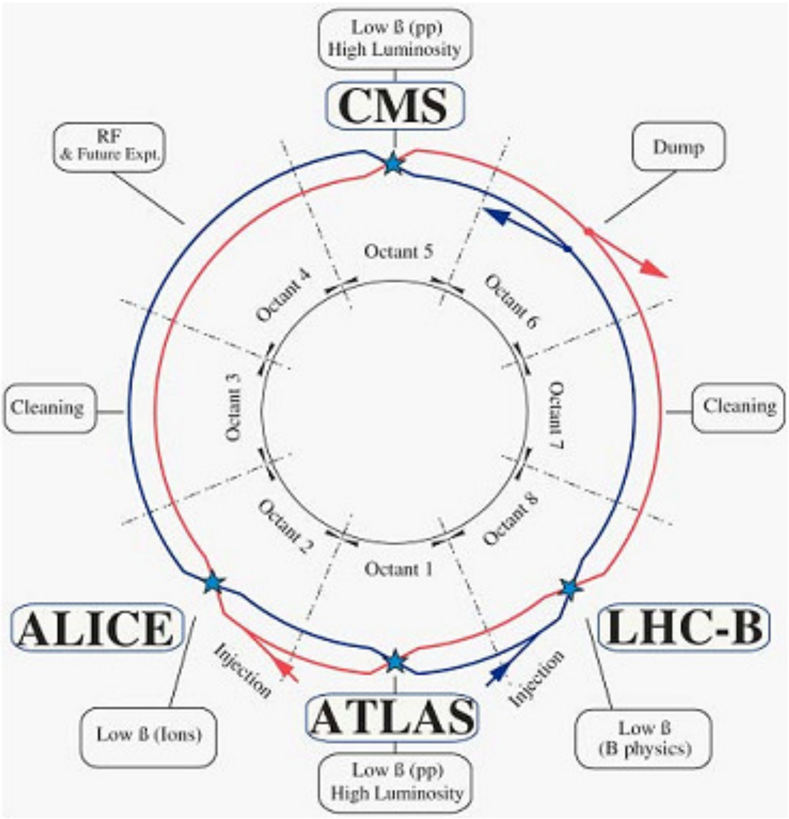

Figure 3.1.: Schematic layout of the LHC (Beam 1–clockwise, Beam 2–anti clockwise).

3.1.1. The LHC design

The LHC is designed to collide proton beams with a CM energy of 14 TeV and luminosity of 10^{34} cm^{-2}s^{-1}. The maximum total integrated luminosity per year is 80-120 fb^{-1}, assuming the machine can be operated for 200 days per year. The maximal number of bunches instantaneously circulating at the tunnel is 2808 per beam (there are 3564 bunch slots), where the minimum nominal bunch spacing is 25 ns. This corresponds to a maximum bunch crossing frequency of 40 MHz. The maximum bunch intensity is $\sim 10^{11}$ protons per bunch. The peak beam energy depends on the integrated dipole field around the storage ring, which implies a peak dipole field of 8.33 T for the 7 TeV in the LHC machine. The LHC ring accommodates 1232 such main superconducting dipoles magnets to keep the beam circulating in it.

3.1.2. The LHC operation in 2012

During the *pp* data taking periods in 2012, the LHC operated at the nominal energy of 4 TeV for each beam. The nominal bunch spacing in 2012 proton run was 50 ns until December and later it was 25 ns, in order to reduce the pileup.

At the high-luminosity experiments the number of interactions is maximized by the "β-squeeze" (beam focusing), where in 2011 the value of β^* was initially 1.5 m reduced later to 1.0 m in mid-September 2011, while in 2012 it was reduced to 0.8. This resulting increase in luminosity typically leads to several proton-proton interactions occurring in the same bunch crossing. Consequently, every interaction which was registered by the detector is accompanied by several minimum bias events from the same bunch crossing (in-time pile-up) and previous bunch crossing (out-of-time pile-up).

The in-time pileup results in additional reconstructed primary vertices. The increased average number of vertices can influence the efficiency of the event selection through the effect on lepton isolation criteria, measurement of the missing transverse energy, etc.

In 2012, the integrated luminosity of the *pp* collisions at $\sqrt{8}$ TeV, as recorded by ATLAS was 21.7 fb^{-1}. The total integrated luminosity as delivered by the LHC and as recorded by the ATLAS detector can be seen in figure 3.2. For a comparison, the previously running experiment TEVATRON, a $p\bar{p}$ collider with a center of mass energy of 1.96 TeV, collect almost 10 fb^{-1}of data over its whole operation period [22].

3.2. The ATLAS detector

ATLAS is a large multi purpose 4π detector. The coordinate system and nomenclature used to describe the ATLAS detector and the particles emerging from the *pp* collisions are briefly summarized here.

The nominal interaction point is defined as the origin of the coordinate system, while the beam direction defines the z-axis and the $x - y$ plane is transverse to the beam direction. The positive x-axis is defined as pointing from the interaction point to the centre of the LHC ring and the positive y-axis is defined as pointing upwards. The side-A of the detector is defined as that with positive z and side-C is that with negative z. The azimuthal angle ϕ is measured around the beam axis, and the polar angle θ is the angle from the beam axis. The pseudorapidity is defined as $\eta = -\ln\tan\theta/2$. The transverse momentum p_{T} is defined in

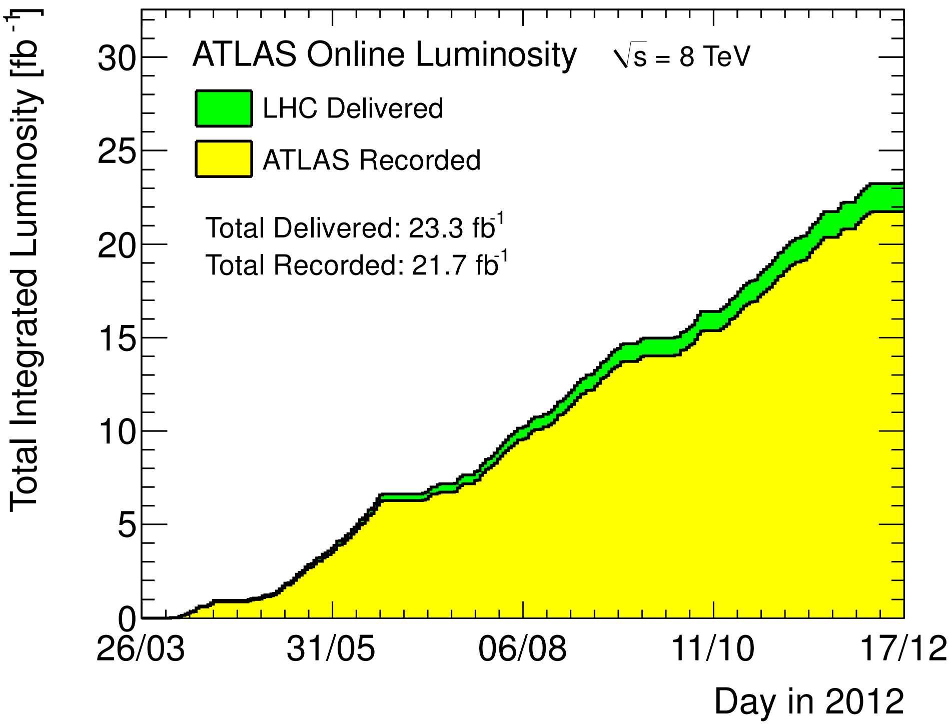

Figure 3.2.: Delivered and recorded luminosity for pp collisions at $\sqrt{s} = 8$ TeV , as seen by the LHC and ATLAS respectively in 2012.

the $x - y$ plane. The distance ΔR in the pseudorapidity-azimuthal angle space is defined as $\Delta R = \sqrt{\Delta\eta^2 + \Delta\phi^2}$.

The ATLAS detector [17] layout is shown in Fig. 3.3. The dimensions of the detector are 25 m in height and 44 m in length. It's overall weight is approximately 7000 tonnes. It covers almost the full solid angle around the collision point with layers of tracking detectors, calorimeters and muon chambers. It has an onion-like structure which can be divided into three major sub-systems:

- Inner Detector (ID)
- Calorimeters
- Muon spectrometer surrounding the calorimeters

The magnet configuration comprises a thin superconducting solenoid surrounding the ID cavity and supplying a two Tesla magnetic field for the measurement of the track momentum in the ID, and three large superconducting air core toroids, one long barrel and two end-caps,

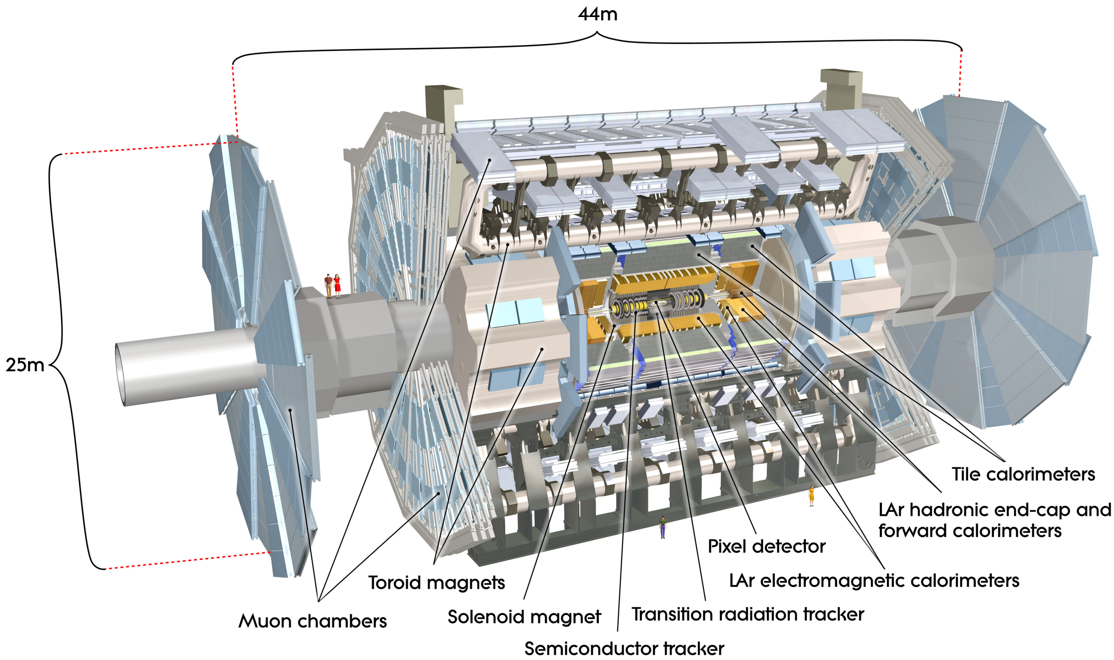

Figure 3.3.: Cut-away view of the ATLAS detector. The dimensions of the detector are 25 m in height and 44 m in length. The overall weight of the detector is approximately 7000 tones.

arranged with an eight-fold azimuthal symmetry around the calorimeters and generating a strong bending power in a large volume within a light and open structure.

For the analysis preformed in this document the trigger system, the Inner Detector (ID), the Calorimeter and the Muon Spectrometer (MS) are of particular importance.

3.2.1. Inner detector

The ATLAS ID has a fully coverage in ϕ and covers the pseudorapidity range $|\eta| < 2.5$. It consists of a silicon Pixel detector (Pixel), silicon strip detector (SCT) and Transition Radiation Tracker (TRT). This set of detectors covers the radial distance of 50.5 mm from the interaction point up to 1066 mm surrounded by an axial magnetic field of 2 Tesla.

A detailed conceptual layout of the ID can be seen in figure 3.4. The highest granularity is achieved around the vertex region using semiconductor pixel detectors followed by a silicon microstrip detector. Typically for each track the pixel detector contributes three and the strips four space points. At larger radii typically 36 tracking points are provided by the straw tube tracker. The relative precision of the measurement is well matched, so that no single measurement dominates the momentum resolution. The outer radius of the Inner Detector is 1.15 m, and the total length 7 m. In the barrel region the high-precision detectors are arranged in concentric cylinders around the beam axis, while the end-cap detectors are mounted on disks perpendicular to the beam axis. The barrel TRT straws are parallel to the beam direction. All end-cap tracking elements are located in planes perpendicular to the beam direction.

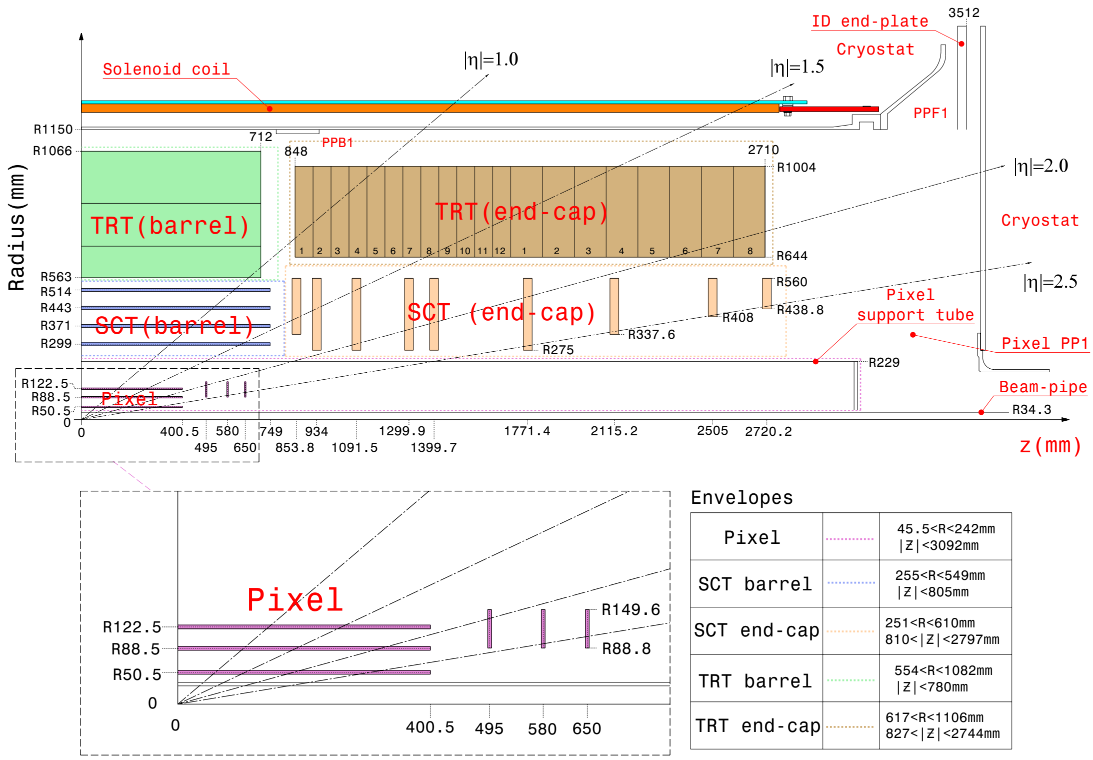

Figure 3.4.: Plan view of a quarter-section of the ATLAS inner detector showing each of the major detector elements with their active dimensions and envelopes.

3.2.2. Calorimeter

The ATLAS calorimeter in the central (barrel) region is composed of high granularity Liquid Argon (LAr) electromagnetic sampling calorimeters that cover the pseudorapidity range up to $|\eta| < 3.2$. The hadronic calorimeter in the barrel is made of scintillating tiles and covers the range $|\eta| < 1.7$. In the range $1.5 < |\eta| < 3.2$, namely the end-caps, the hadronic calorimeter uses LAr technology. At higher $|\eta|$, up to $|\eta| < 4.9$, LAr is used for both electromagnetic (EM) and hadronic (HAD) energy measurements.

3.2.3. Muon spectrometer

The layout of the muon spectrometer is shown in figure 3.5. The ATLAS Muon Spectrometer (MS) is designed for triggering and measuring tracks of minimum ionizing particles in a large range of pseudorapidity up to $|\eta| < 2.7$. It is made of a large toroidal magnet, with an average field of 0.5 Tesla. The MS consist of four types of detectors and has one barrel region (BR) and two End-cap Regions (ER). For precision measurement it has Monitored Drift Tubes chambers (MDT) that are located both in the BR and ER sections and Cathode Strip Chambers (CSC) in the inner most part of the ER. It uses for trigger Resistive Plate Chambers (RPC) and Thin Gap Chambers (TGC) in the BR and in the ER respectively. The chambers are arranged in three layers so particles traverse at least 3 stations with a lever arm of several meters. The detector is design to measure a very large spectrum of transverse momentum with high resolution. The stand-alone transverse momentum resolution of approximately 10% for a 1 TeV muon, which translates into a sagitta along the z (beam) axis of about 500 μm, to be measured with a resolution of $\leq$ 50 μm. Muon momenta down to a few GeV may be measured by the spectrometer alone. Even at the high end of the accessible range ($\sim$3 TeV), the stand-alone measurements still provide adequate momentum resolution and excellent charge identification.

(a) (b)

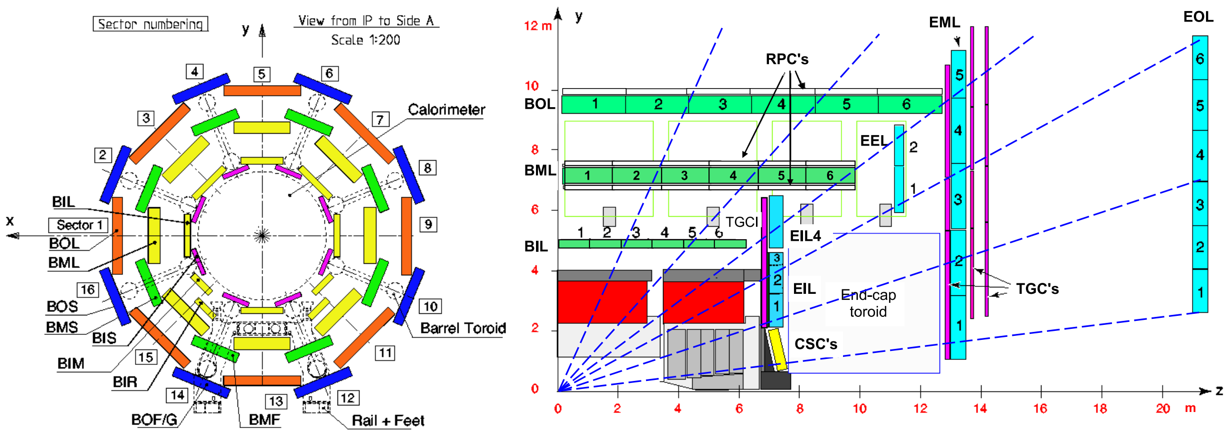

Figure 3.5.: In (a), The cross-section of the barrel muon system perpendicular to the beam axis (non-bending plane), showing three concentric cylindrical layers of eight large and eight small chambers. The outer diameter is about 20 m. In (b), the cross-section of the muon system in a plane containing the beam axis (bending plane). Infinite-momentum muons would propagate along straight trajectories which are illustrated by the dashed lines and typically traverse three muon stations.

In the trigger system, resistive-plate chambers (RPC) are used in the barrel ($|\eta| < 1.05$) and thin-gap chambers[1] (TGCs) in the end-cap regions ($1.05 < \eta < 2.4$). The trigger chambers for the muon spectrometer serve a threefold purpose:

- Provide bunch-crossing identification due to their excellent timing resolution
- Provide well-defined p_{T} thresholds for the trigger system
- Measure the muon coordinate in the direction orthogonal to that determined by the precision-tracking chambers

3.3. Triggering and data acquisition

The proton-proton interaction rate at the design luminosity of $10^{34} cm^{-2} s^{-1}$ is about 1 GHz, while the event data recording limit is about 200 Hz. This requires a sophisticate trigger system that will be able to recored the important events. ATLAS has three-level trigger system, Level 1 (L1), Level 2 (L2) and the Event Filter (EF), where the L2 and the EF together form the High-Level Trigger (HLT). The L1 trigger uses reduced granularity information from a subset of detectors: for high-P_T muons it uses the RPC's and the TGC's, for electromagnetic clusters, jets, τ leptons, E_T^{miss} and large total transverse energy it uses the calorimeter sub-system. The maximum L1 acceptance rate which the detector readout system can handle is 75 kHz, and the L1 decision must reach the front end electronics within 2.5 μs after the bunch-crossing which it is associated. Regions of Interest (RoI's) are identified as possible trigger objects within the event from L1 and passed to the L2. The L2 trigger uses RoI information on coordinates, energy and type of signatures to reduce the event rate below 3.5 kHz, with average processing time of $\sim$40 ms. The EF uses offline analysis on fully built events to reduce the rate to approximately 200 Hz, with an average processing time of $\sim$4 s.

3.3.1. The muon trigger

The schematic layout of the trigger system is shown in figure 3.6. The trigger detectors must provide acceptance in the range $|\eta| \leq 2.4$ and over the full ϕ-range. The resolution requirements in barrel and end-cap are different. The main reasons for that is:

- The muon momenta for a given p_{T} is strongly increasing with η

[1]The TGCs were mainly constructed and tested in Israel

- The three trigger layers in the end-cap are outside the magnetic field - seeing no curvature
- The distance between the three trigger layers in the end-cap are smaller than the ones in the barrel (see figure 3.6)
- Radiation level in the end-cap region reach a factor of 10 higher than in the barrel

If one wants to match the p_T-resolution of the barrel one needs to increase the η-dependent granularity leading to a finer granularity in the end-cap trigger readout.

The trigger in the barrel and the end-cap regions is based on three trigger stations each. The algorithm require a coincidence of hits in three trigger stations within a road, and tracks the path of the muon from the interaction point through the different detector layers. The road width is related to the p_T threshold that is applied for the different triggers.

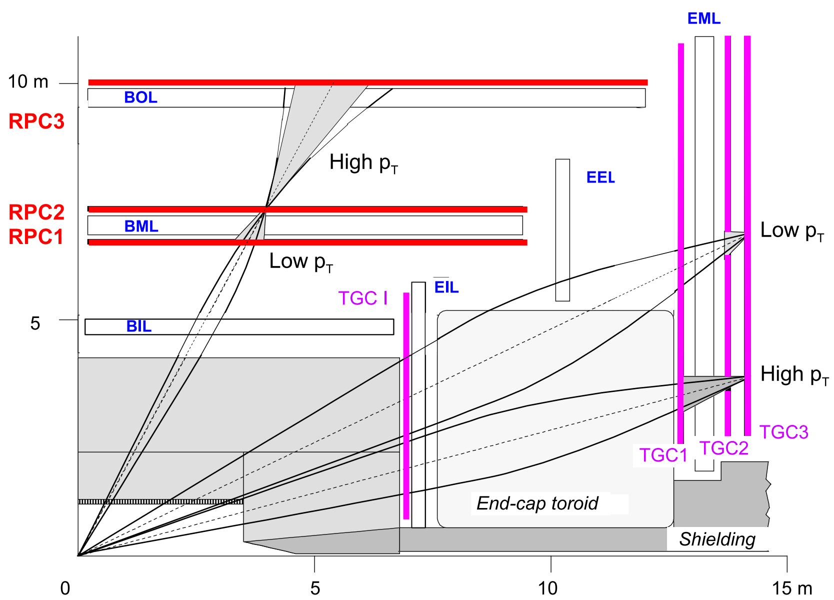

Figure 3.6.: Schematics of the muon trigger system. RPC2 and TGC3 are the reference (pivot) planes for barrel and end-cap, respectively.

In the end-cap, the three layers are in front (TGC1) and behind (TGC2 and TGC3) the second MDT wheel, while the fourth layer is located in front of the innermost tracking layer (see figure 3.6). The trigger information is generated by a system of fast coincidences between the three last layers along the trajectory of the muon.

Each coincidence pattern corresponds to a certain deviation from a straight line, i.e. curvature of the track, which is used as a criterion for the track to have passed a predefined momentum threshold. The deviation from a straight line is the deviation of the slope of the track segment between two trigger chambers from the slope of a straight line between the interaction point and the hit in a reference layer called the pivot plane, which is the second layer in the barrel (RPC2) and the last layer in the end-cap (TGC3), as illustrated in figure 3.6. For the present analysis, low p_{T} triggers are used, so for example in the end-cap, the slope between TGC3 and TGC2 is compared to the slope between the interaction point and TGC3 and in the barrel the slope between RPC2 and RPC1 is compared to the slope between the interaction point and RPC2.

A system of programmable coincidence logic allows concurrent operation with a total of six thresholds, three associated with the low-p_{T} trigger (threshold range approximately 6–9 GeV) and three associated with the high-p_{T} trigger (threshold range approximately 9–35 GeV). The trigger signals from the barrel and the muon end-cap trigger are combined into one set of six threshold multiplicities for each bunch-crossing in the muon to CTP interface, before being passed on to the CTP itself. Thus, the L1 muon trigger searches for patterns of hits consistent with low and high-p_{T} muons originating from the interaction region in the six independently-programmable p_{T} thresholds. The information (for each bunch-crossing) used in the L1 trigger decision is the multiplicity of muons for each of the p_{T} thresholds where muons are not double-counted across the different thresholds.

3.4. ATLAS software

The ATLAS software version that was used for this analysis is labeled release 17.2.10.

3.4.1. The ATHENA framework

The ATLAS experiment records approximately 1 PB of data per year. The analysis of this enormous amount of data is a great challenge for the collaboration. To address this challenge a standard framework for simulation, reconstruction and physics analyses in ATLAS has been developed named Athena [23, 24]. Athena is based on the Gaudi framework [25], an architecture originally developed for LHCb experiment. It is an implementation of the component-based architecture responsible for handling the configuration and execution of several C++ packages through python scripts. It takes care of the execution order, data flow and persisting issues.

There are four event data formats that can be analysed by Athena framework in ATLAS:

- RAW data: contains the output of the ATLAS detector, produced by real or simulated events after the HLT. It comes in the "bytestream" format as they are delivered from the detector, rather than object-oriented format. The average size of each event is approximately 1.5 MB.
- Event summary data (ESD): holds the output of the reconstruction process. Both detector information and combined reconstruction objects like muons, electrons and jets are stored at this stage. An object-oriented format based on ROOT [26] objects is adopted, and the typical event size is 1 MB.
- Analysis object data (AOD): a subset of the ESD, with the physical objects used in analysis and few detector objects to allow track-refitting, isolation studies and others. The AOD is also stored in ROOT format and the nominal event size is of the order of 100 KB.
- Skimmed dimuon AOD (DAOD): contains a small subset derived from the AOD / ESD, specific for an analysis or performance group. More than one derivation is possible, in which the data is reduced by removing unnecessary physics blocks (e.g. jets, photons etc.), selecting only some objects and dropping irrelevant information from those objects. User-data can be added in the process, and in the final stage of derivation a flat ROOT n-tuple can be produced.

For this analysis AODs and DAODs were used for making slimmed n-tuples. These DAODs were specialized for the use of B-physics analyses and were available only from 2012.

3.4.2. Flagging data for physics analysis

Since not all of the recorded collision data are "good" for physics analysis, it is essential to identify which collisions are good and which are not. To define a good collision, Data Quality (DQ) information is needed, as assessed by the DQ group. The use of this DQ information in a physics analysis is done via the use of dedicated lists of runs and luminosity blocks, known as "good run lists" (GRLs). A luminosity block (LB) is the unit of time for data-taking, and lasts about two minutes. A good run list is formed by applying DQ criteria, and possibly other criteria, to the list of all valid physics runs and LBs. The DQ flags are simple indicators of data quality, and act much like a traffic light. To form a GRL, a query of DQ flags is required to be green, i.e. indicating good data. In a physics analysis, the requirement of good runs and luminosity blocks needs to be included in the event selection, to skip events from bad runs and luminosity blocks.

Chapter 4.

Event selection

The thesis covers two measurements, the J/ψ direct and indirect production cross section measurement and measurement of the J/ψ spin-alignment. This section starts with the event selection which is common to both analyses. The following chapters will detail the two measurements.

4.1. Data samples

Collision data with a center of mass energy of 8 TeV, are included in this analysis. Segments of data known as *luminosity blocks* within those runs are included if they are taken in periods declared by the LHC operators to have stable beams. Additionally, data is only included if it is deemed to be suitable for physics analysis, on the basis of the status of the muon spectrometer, inner detector, calorimeter and magnet systems. Events within those luminosity blocks are required to have passed the L1 muon or EF trigger as described in Section 3.2. Taking into account the luminosity block selection, the total integrated luminosity for the sample is calculated to be 14.1 fb^{-1}.

The data used in this analyses were taken from period C6 through period L of the 2012 data-taking. The analyses presented here deploys the two triggers described in section 3.3 - the EF trigger which is fed from the MBTS trigger, and the L1 muon trigger without p_{T} thresholds.

The candidate preselection proceeds as follows: In order to select well reconstructed muons, the 2012 Muon Combined Preformance (MCP) guidelines are followed. It require that each muon used in the analysis satisfy the following set of cuts:

- At least one hit in the Pixel detector. A dead Pixel sensor crossed by the track is also considered as a hit
- At least five hits in the SCT. A dead SCT sensor crossed is also considered as a hit
- If $0.1 < |\eta| < 1.9$:

  At least six TRT hits, including TRT outliers [1], with outlier fraction below 0.9
- At most two Pixel or SCT holes along the track

In addition to these selections $J/\psi \to \mu\mu$ candidates were selected by requiring two combined muons [2] with $p_{\mathrm{T}} > 4$ GeV, $|\eta| < 2.3$ and $p > 3\ GeV$. The common vertex probability is required to be higher than 0.01. Only candidate with invariant mass of $2.6 < m_{J/\psi} < 3.5\ GeV$ are taken and with pseudo-proper time in the range $-1.5 < \tau < 13\ ps$ are selected in order to reduce background events. Trigger matching is imposed by requiring a $\Delta R < 0.05$ between each muon and its matched trigger object.

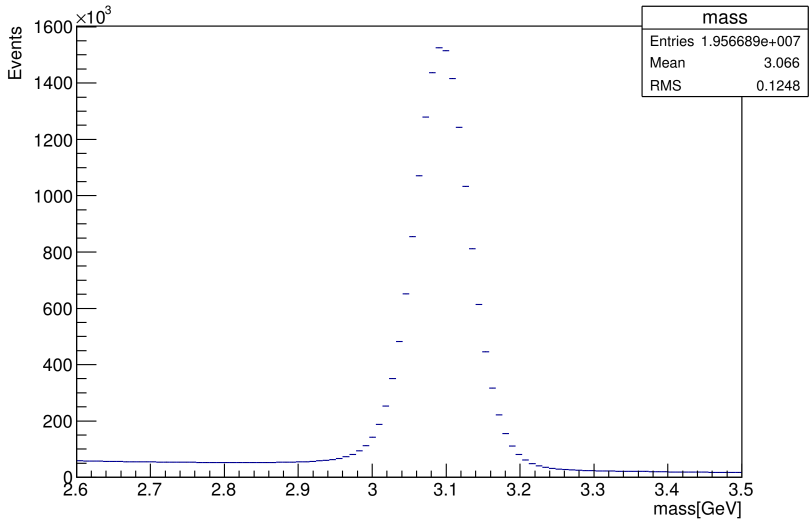

Figure 4.1.: J/ψ mass distribution in the entire p_{T} region, after applying all selection cuts.

The data sample is divided into 19 p_{T} slices in the range between 8 to 70 GeV and rapidity $0.2 < |y| < 0.8$.

The trigger selected for this analysis is named EF_2mu4T_Jpsimumu_L2StarB. It is a dimuon trigger with minimum muon's p_{T} of 4 GeV. This trigger is a dedicated trigger for analysis in the BPhysics group at ATLAS and therefore it is not heavily prescale throughout the

[1]TRT outlier is either a straw tube with a signal but not crossed by the nearby track, or a set of TRT measurements around the track extrapolation which, however, fail to form a smooth trajectory together with the pixel and SCT measurements.

[2]combined muons are reconstructed from tracks in both ID and MS

whole period. The early runs of 2012 suffered from low efficiency for events with large lifetimes, hence the trigger was modified to compensate for that loss. As a result the polarization measurement can be preformed on 70% of the event sample.

The spin-alignment analysis is preformed in two modes, one in the low J/ψ p_{T} region (below 20 GeV), using a MC sample with muon p_{T} threshold of 4 GeV. The second region, above 20 GeV is using a MC sample with muon p_{T} threshold of 6.5 GeV (for reason the will be explain in detail later). For this reason two data samples are also prepared using the same kinematic cuts.

In Figure 4.1 all J/ψ candidate are shown, for the entire J/ψ p_{T} region and the selected rapidity slice, after all the selected cut describe above. In Table 4.1 the total number of events after all the selection cuts for the different slices described above are listed.

4.2. Rapidity slice

Figure 4.2 depicts the η-ϕ distribution of the higher p_{T} muons. It shows the low efficiency in the region of η close to zero due to holes in the ATLAS coverage used for for supports and services.

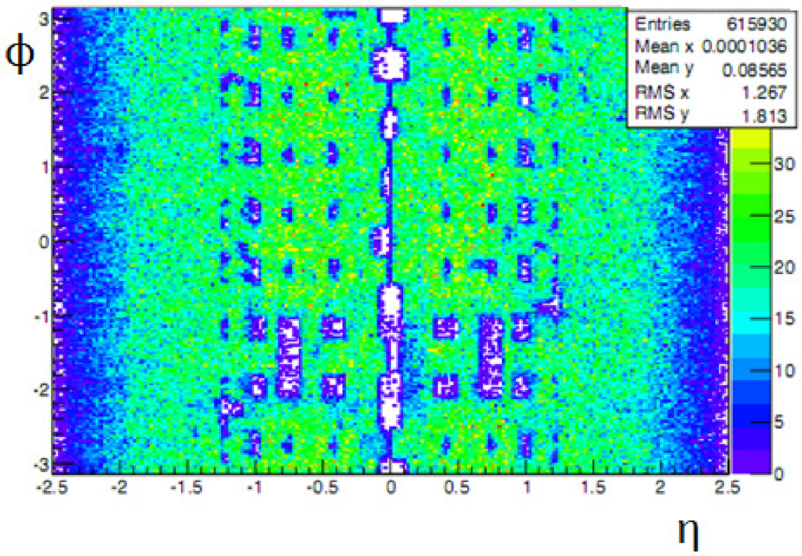

Figure 4.2.: η-ϕ distribution of the high p_{T} muon.

The selection of the rapidity slices was designed with the aim to minimize the potential biases on the J/ψ spin-alignment measurement. For example, for a J/ψ in the direction around

Table 4.1.: Total J/ψ candidates after all selection cuts for each individual kinematic slice.

$p_T[GeV]$ slice	$J/\psi \to \mu(4)\mu(4)$ candidates	$J/\psi \to \mu(6.5)\mu(6.5)$ candidates
8.0 - 8.5	509657	0
8.5 - 9.0	809563	0
9.0 - 9.5	986713	0
9.5 - 10.0	1063487	0
10.0 - 10.5	1069729	0
10.5 - 11.0	1031045	0
11.0 - 11.5	965079	0
11.5 - 12.0	891084	0
12.0 - 13.0	1546302	8145
13.0 - 14.0	1253877	158029
14.0 - 15.0	1000718	270238
15.0 - 16.0	794392	298381
16.0 - 18.0	1135631	545504
18.0 - 20.0	729997	425229
20.0 - 25.0	909829	615126
25.0 - 30.0	353423	269230
30.0 - 40.0	224227	183421
40.0 - 50.0	54768	47189
50.0 - 70.0	21955	19324
8.0 - 70.0	15351476	2839816

η equal zero ("crack region"), where the detector acceptance is low, for certain ϕ^*, the two muons will bend to the detector direction and will be detected. But for a J/ψ with the same kinematics (p_{T} and rapidity), with different ϕ^* angle, one or two of the muons can fall into the low acceptance region, hence the J/ψ will not be detected. Figure 4.3 illustrates this phenomena.

A toy MC and full MC study was preformed in order to find the lowest J/ψ rapidity that is minimally effected from that uncovered region. For this purpose, the sample is divided into small rapidity slices and examine in each slice the rate of events with at least one real muon in the uncovered region failing reconstruction. Examining slice by slice the rate of events having one truth muon in the crack region that failed the reconstruction, it was found that from

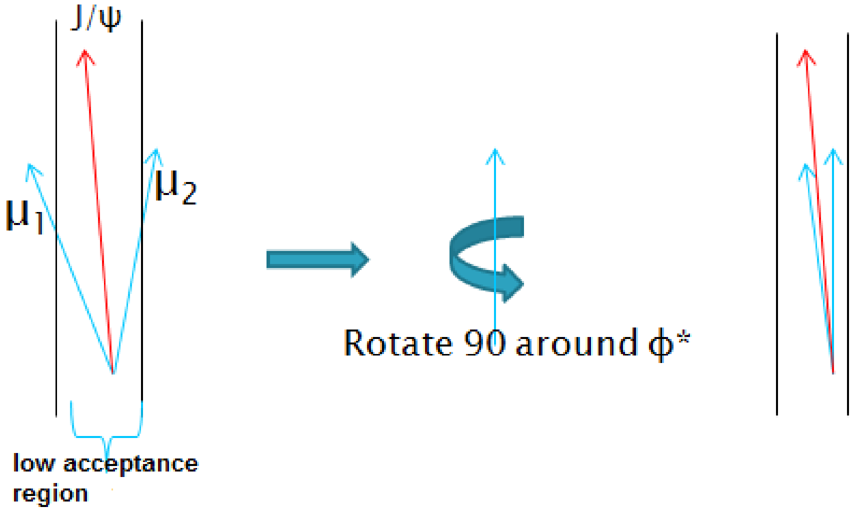

Figure 4.3.: Illustration of low acceptance possible bias

rapidity above 0.2 less than 9% of events at p_{T} below 10 GeV escape detection, and as the p_{T} increases the inefficiency vanishes.

4.3. ϕ^* low efficiency region

When looking at the angular distribution of the decaying muons (see Figure 5.10), one can notice low efficiency regions in two places:

- ϕ^* around $+\pi/2$ mostly at negative $cos(\theta^*)$
- ϕ^* around $-\pi/2$ mostly at positive $cos(\theta^*)$

Figure 4.4 shows the ϕ^* projection for different p_{T} slices in the data.

It can be seen that there are two low efficiency regions as mentioned around $\phi^* = \pm\pi/2$. In addition it can be seen that these inefficiencies are p_{T} dependent, i.e. as the J/ψ p_{T} increases, the inefficiencies increases. This inefficiencies also seen in the MC sample (see Figure 6.6).

An intuitive explanation for this phenomena is using the so called ”cowboy” and ”sailor” schemes: When considering two J/ψ with identical kinematics, but with opposite charge assignment, the muon pair will bend in different structure due to the magnetic field. In one combination, the muons getting closer together in the MS (”cowboy”), significantly reduce the dimuon trigger rate, due to multiple hits in the same segments. In the second case both muons

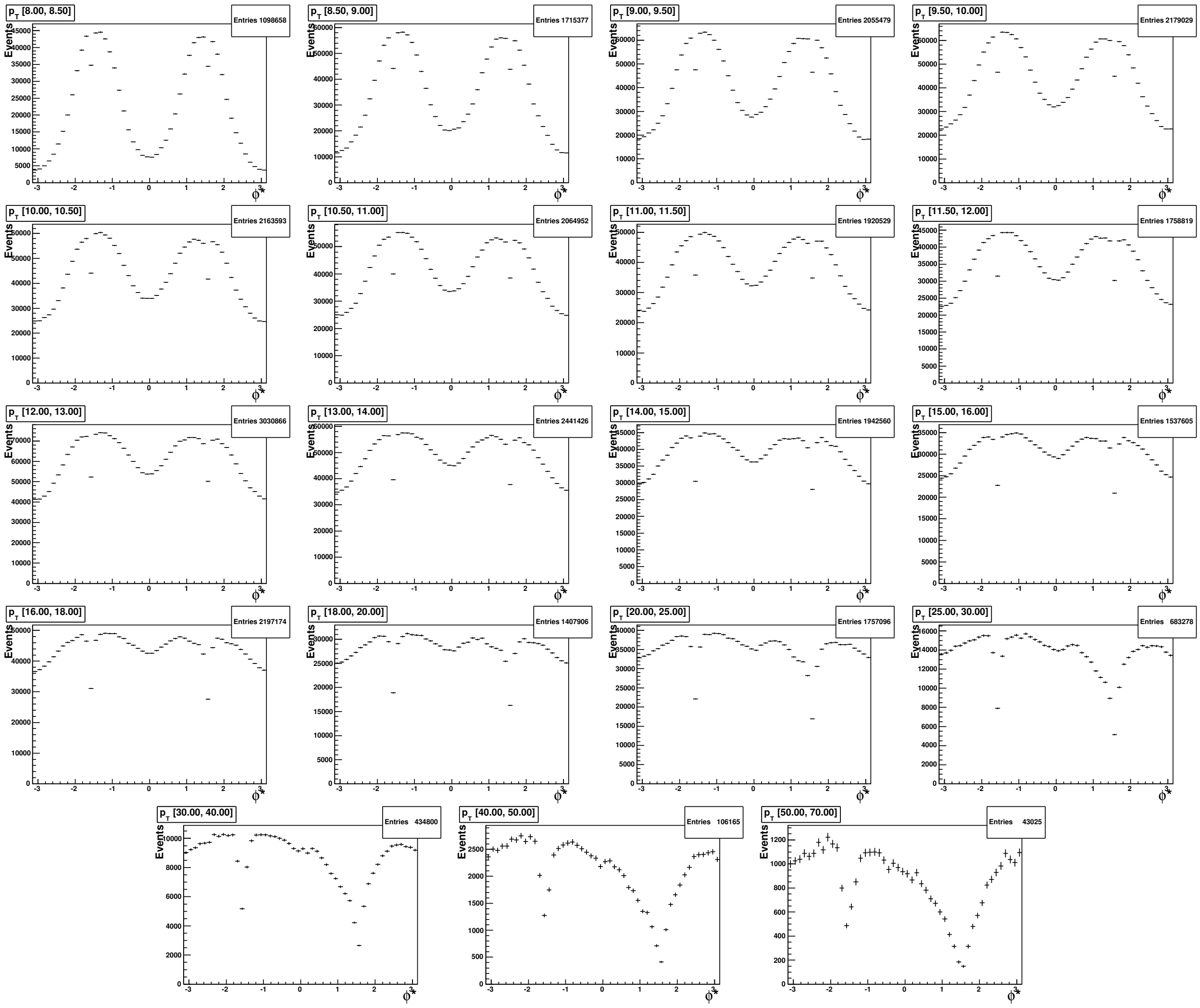

Figure 4.4.: ϕ^* projection for different p_T slices. The plots are ordered from the lowest p_T to the highest.

will go apart from each other (”sailor”), and will reach different segments of the detector. This is illustrated in Figure 4.5.

The solenoid magnetic field in the barrel region of the ATLAS detector is shown in Figure 4.6 as a function of the distance from the center of the detector along z-axis. The dominant component of the magnetic field is towards the positive z-axis (almost in all the barrel region). This means that muons will mainly bend on the transverse plane (changing the value of ϕ while the η is unchanged).

Due to bending the muon pair tracks in the ϕ direction, the two muons can hit the same detector segments if their η values are close.

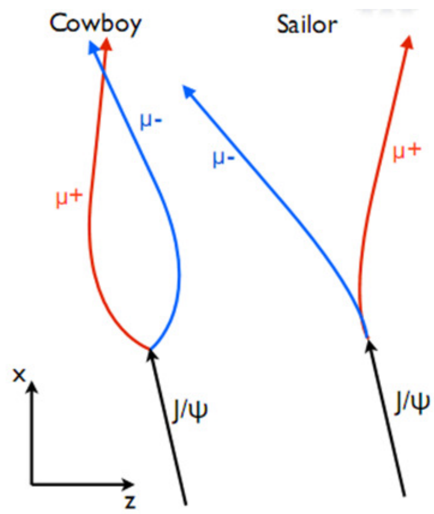

Figure 4.5.: Illustration of "cowboy" and "sailor" muon pairs. Due to the magnetic field, muons can bend towards each other (cowboy) or moving apart (sailor).

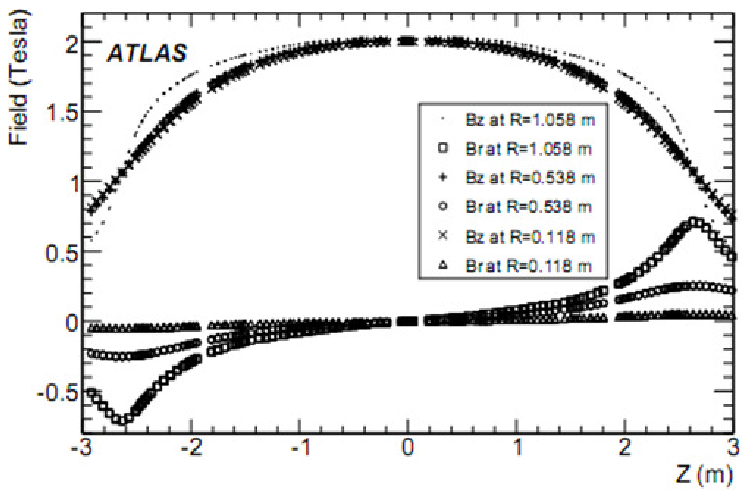

Figure 4.6.: The solenoid magnetic field in the barrel region along z-axis .

$\phi^* = \pm\pi/2$ characterized by two muons close in rapidity. If the muons are in this regions, and are of the cowboy type events, it is probable that they will escape the dimuon trigger detection. The p_T dependence is due to the fact that as the p_T increases the muon tracks tend to stay closer, producing many hits in the same detector segments, which can be identified as single (very noisy) track.

In Chapter 7, estimation of the systematics uncertainty rising from these low efficiency regions is preformed.

Chapter 5.

Prompt-Non-Prompt fraction

This chapter presents a measurement of the production ratio of prompt to non-prompt J/ψ. Prompt production is defined by direct production, where the J/ψ is produced via the hard interaction, or via the the direct production of an excited state, which then decays to the J/ψ in *feed-down process* . The non-prompt J/ψ is expected to come from the decays $b \to J/\psi + X$ and the continuum of $b\bar{b}$ events. The measurement is performed in the dimuon decay mode of pp collisions at the center of mass energy of 8 TeV, with an integrated luminosity of 14.1 fb^{-1}, and are presented as a function of the J/ψ transverse momentum and rapidity. This analysis is a direct continuation of the measurement preformed on the 7 TeV data that was published based on the data taken in 2010 [27].

The data sample and the selection cuts are as described in chapter 4.

5.1. Proper decay time

Experimentally, it is possible to distinguish between J/ψ from prompt production and decays of heavier charmonium states (prompt production) and the J/ψ produced in B hadron decays (non-prompt production).

The former decay at their production point, which is the primary vertex of the event, while the J/ψ mesons produced in B hadron decays will have a displaced decay point due to the long lifetime of their B parent hadron. From the measured distances between the primary vertices and corresponding J/ψ decay vertices one can infer the fraction of J/ψ that originate from non-prompt sources. An unbinned maximum likelihood fit is used to extract this fraction from the data. The signed projection of the flight distance of the J/ψ , $\vec{L}$, onto its transverse momentum $\vec{p_{\mathrm{T}}}(J/\psi)$ is calculated,

$$L_{xy} \equiv \frac{\vec{L} \cdot \vec{p_{\mathrm{T}}}(J/\psi)}{|\vec{p_{\mathrm{T}}}(J/\psi)|} \tag{5.1.1}$$

as a measure for the displacement of the J/ψ vertex. Here, $\vec{L}$ is the vector from the primary vertex to the J/ψ decay vertex and $\vec{p_{\mathrm{T}}}(J/\psi)$ is the transverse momentum vector of the J/ψ. The probability for the decay of a B hadron to J/ψ as a function of proper decay time follows an exponential distribution

$$p(t) = \frac{1}{t_B} exp(-t/t_B) \tag{5.1.2}$$

where t_B is the lifetime of the B hadron and t is the proper decay time. For each decay the proper decay time can be calculated as

$$t = \frac{L}{\beta\gamma c} \tag{5.1.3}$$

where L is the distance between the B hadron production and decay point, $\beta\gamma$ is the Lorentz factor and c is the speed of light. For relativistic particles $\beta\gamma$ is equal to a particle's momentum divided by its mass. Therefore, for B hadrons if one takes the projections of the decay length and momentum on the transverse plane, one obtains

$$t = \frac{L_{xy} m_B}{p_{\mathrm{T}}(B)} \tag{5.1.4}$$

L_{xy} is measured between the position of the secondary vertex found in the offline analysis, and the primary vertex in the event. The primary vertex is refitted with the two muon tracks excluded, to avoid a bias. The uncertainty on L_{xy} is calculated from the covariance matrices of the primary and the secondary vertices. Since the B hadron is not completely reconstructed, the J/ψ momentum is used in a variable called "pseudoproper decay time":

$$\tau = \frac{L_{xy} m(J/\psi)}{p_{\mathrm{T}}(J/\psi)} \tag{5.1.5}$$

Here, the world average value of m(J/ψ) is used to reduce the correlation between the fits that will be performed on the mass and the lifetime; however, studies have shown that the results are insensitive to this choice. At large J/ψ p_{T}, where most of the B transverse momentum is carried by the J/ψ, the distribution of τ will have an almost exponential distribution with the B hadron lifetime as a parameter. At small p_{T} the range of opening angles between the J/ψ

and B hadron momentum leads to a smearing of the underlying exponential distribution. By making a cut on τ one can efficiently distinguish between prompt to indirect J/ψ samples as shown in Fig. 5.1. The different shapes of the decay time between these two populations used

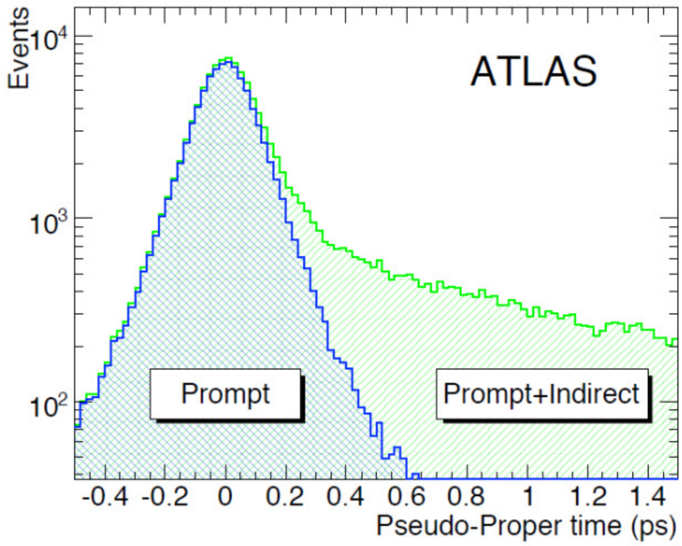

Figure 5.1.: *Simulated pseudo-proper decay time distribution for reconstructed prompt J/ψ (blue) and the sum of prompt and indirect J/ψ contributions(green).*

in the fit PDF is describe next.

5.2. Fitting procedure

For each slice of p_{T} and $|y|$ a 2-dimensional unbinned maximum likelihood fit (henceforth referred to as the "fit"), is performed in the dimensions of dimuon invariant mass and pseudo-proper lifetime. Dimuon candidates must be within the ranges: $2.6 < m(\mu^+\mu^-) < 3.5$ GeV, and $-1.5 < \tau(\mu\mu) < 13$ ps^{-1}. From the fitted parameters, the quantities of interest, such as yields, and non-prompt fractions are calculated. The fit is performed using the ROOT framework (version `5.34/09`) and RooFit (version `3.56`).

The events are fitted using the Probability Density Function (PDF):

$$\mathrm{PDF}(m,\tau) = \sum_{i=1}^{5} \oplus\, f_i(m) \;\cdot\; h_i(\tau) \otimes g(\tau) \qquad , \tag{5.2.1}$$

where $\otimes$ implies a convolution, and the individual components are given in table 5.1.

Table 5.1.: Fit model PDF. The definition of each term is described in the text. The symbols $\oplus$ and $\otimes$ are used to define a normalised weighted average and convolution, respectively. The subscripts on each term refer to different PDF terms, which may share common parameters with other terms.

i	Sig./Bkgd	Source	$f_i(m)$	$h_i(\tau)$
1	J/ψ	Prompt	$CB_1(m) \oplus G_1(m)$	$\delta(\tau)$
2	J/ψ	Non-prompt	$CB_1(m) \oplus G_1(m)$	$E_1(\tau)$
3	Bkgd	Prompt	$L_1(m)$	$\delta(\tau)$
4	Bkgd	Non-prompt	$E_3(m)$	$E_4(\tau)$
5	Bkgd	Non-prompt	$E_5(m)$	$E_6(\|\tau\|)$

The component PDF terms are defined below:

- CB – Crystal Ball (Implemented as a RooCBShape);
- G – Gauss (RooGaussian);
- L – Linear;
- E – Exponential.
- Resolution function $g(\tau)$ is a double Gaussian.
- δ – delta function.

In order to stabilize the fit model and reduce the number of free parameters, a number of component terms share common parameters, or use a scaling (free) parameter. The details of the fit model are described below.

The signal mass shapes are described by the sum of a Crystal Ball shape (CB) and Gaussian. The CB and Gaussian share a common mean. The relative fraction of CB and Gaussian is a free parameter.

The signal lifetime shapes are described by an exponential (for positive τ only) convoluted with a Gaussian (describing the lifetime resolution), for the non-prompt component, the same Gaussian is used to describe the prompt contributions. The resolution double-Gaussian has a fixed mean at $\tau = 0$ and free width. The lifetime of the J/ψ is the free parameter of the fit.

The non-J/ψ contributions are described by prompt, non-prompt, and a double-sided exponential (convoluted with double-Gaussian) standing for candidates of miss-reconstructed or non-coherent dimuon pairs. The same resolution double-Gaussian is used to describe the background, as well as the signal. For the non-resonant mass parametrisations, the non-prompt contribution is modeled by an exponential. The prompt mass contribution follows a flat distribution, and the double-sided background uses an exponential.

The important quantities extracted from the fit are: fraction of signal; fraction of signal that is prompt; σ of the CB and of the Gaussian. From these parameters (and their covariance matrix) all measured values are extracted. In total there are 19 free parameters in the fit.

5.3. Fitting results

The summary of the fits results are presented as a function of p_{T} for the selected slice of rapidity in Figure 5.2.

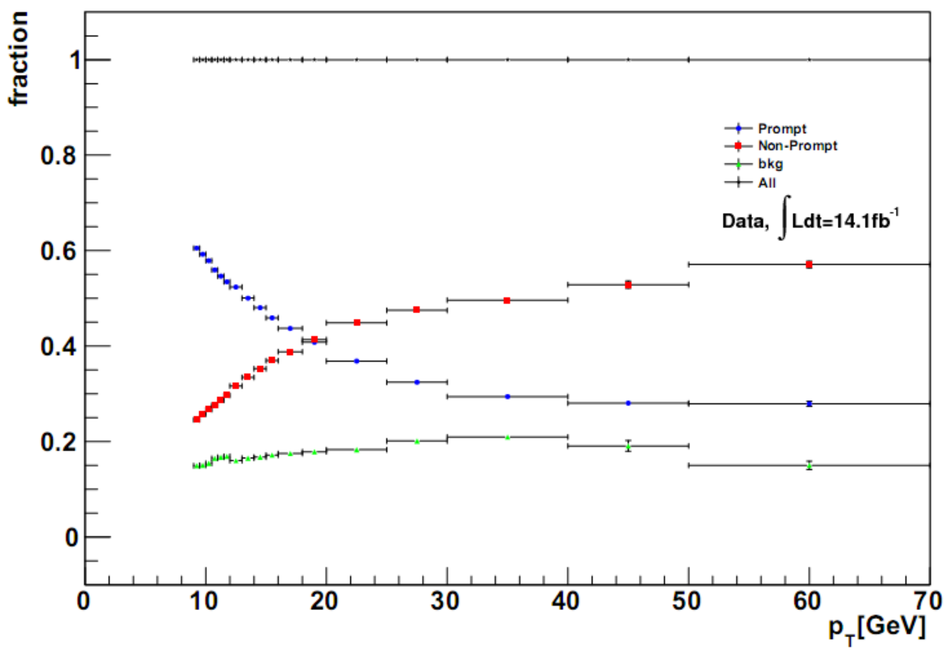

Figure 5.2.: Total fractions over the entire sample as a function of $p_{\mathrm{T}}(\mu^+\mu^-)$ for the selected slices of rapidity. Blue: prompt J/ψ fraction, red: non-prompt J/ψ fraction, green: non J/ψ fraction, black: sum of all fractions.

Each point in Figure 5.2 is extracted form the mass-decay simultaneous fit that is described at section 5.2. Typical mass and decay fit can be seen in Figure 5.3, and the fits results for the different slices are summarized in appendix D.

From Figure 5.2 it can be seen that as the p_{T} of the J/ψ increases the prompt fraction decrease dramatically from around 70% to 30%, and the non-prompt increases from 20% to

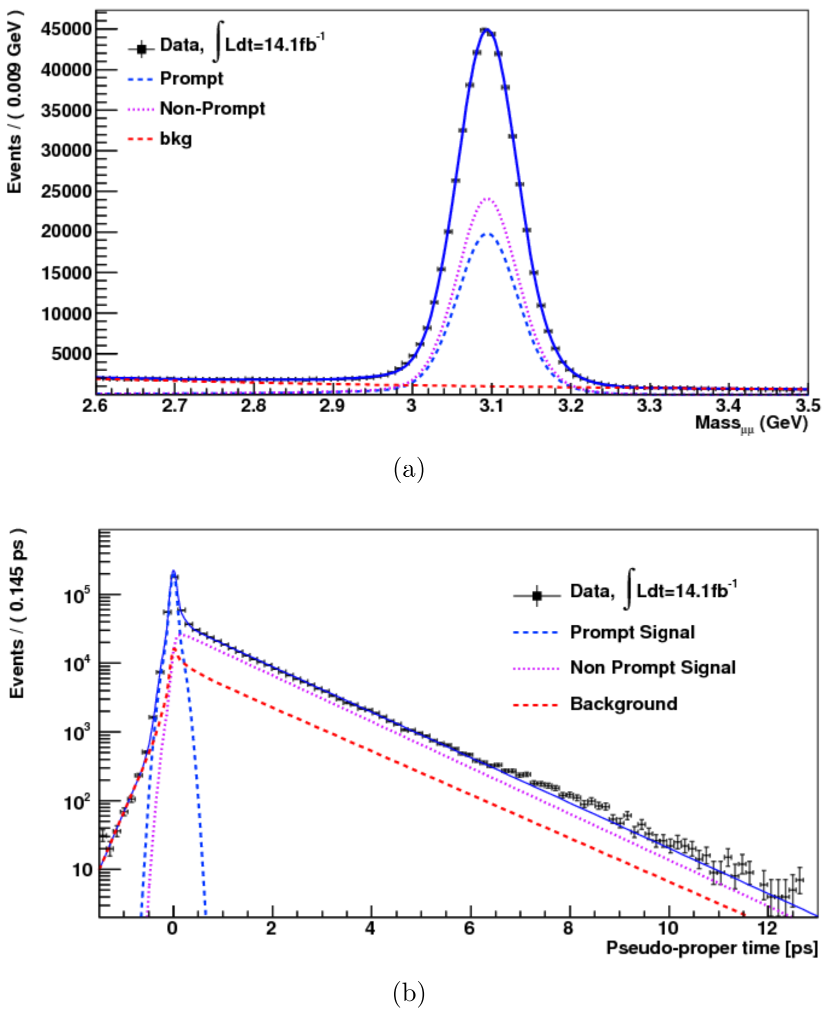

Figure 5.3.: A typical simultaneous mass-decay fit results. (a) is the mass fit result and (b) the pseudo-proper time fit results. Blue line is the total fit result, the blue dash line is the prompt J/ψ PDF, purple dash line is the non-prompt J/ψ and the red dashed line is the background.

55%, while the background is almost constant (slight increase). In addition it can be seen that the different muons p_{T} cut above J/ψ p_{T} of 20 GeV is not affecting the measurement and the fractions distributions are continuous.

5.4. Extract pure prompt sample

In order to extract a prompt-like J/ψ sample, three regions are defined:

- Background - none J/ψ events

- Signal - defined both in the mass and τ space
- Non-prompt J/ψ + background - defined in the signal mass range with high values in the τ space

The different regions are represented by different cuts on the dimuons invariant mass and the τ calculated separately for each slice.

The background sample is defined as the two side bands of the dimuon mass as $[\mu - 8\sigma, \mu - 3.5\sigma]$ and $[\mu + 3.5\sigma, \mu + 8\sigma]$ where μ is the mean of the J/ψ mass and σ is:

$$\sqrt{f_{Gauss}\sigma^2_{gauss} + (1 - f_{Gauss})\sigma^2_{CB}} \tag{5.4.1}$$

where f_{Gauss} is the relative weight of the Gauss function. These regions are shown in Figure 5.4 and represented as the area between the red lines.

The signal region is define in both spaces:

- In the mass space - the region $[\mu - 3\sigma, \mu + 3\sigma]$
- In τ space - the region covers 0.99 of the signal prompt PDF

The signal region is depicted in Figures 5.4 and 5.5

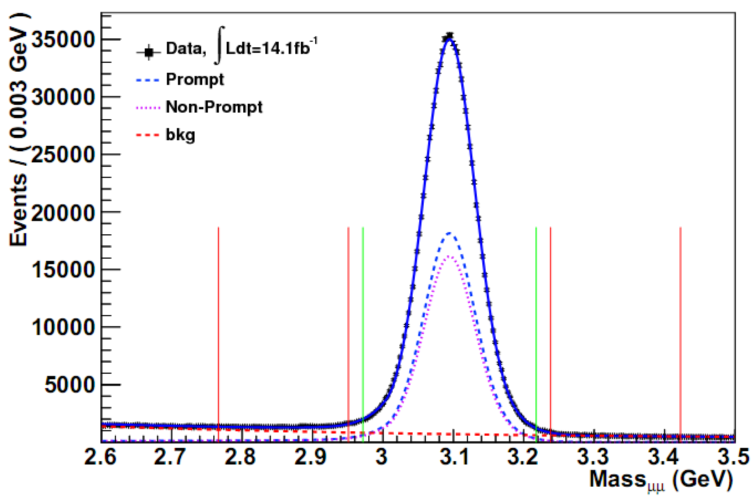

Figure 5.4.: Mass plot example for slice of p_T between 16-18 GeV. The area between the red lines represents the mass sidebands and the area between the green lines represents the mass signal region.

The last region, non-prompt + background, is define as the mass signal region as before with a τ cut at the end of the prompt signal region, i.e. no prompt J/ψ in it (marked by

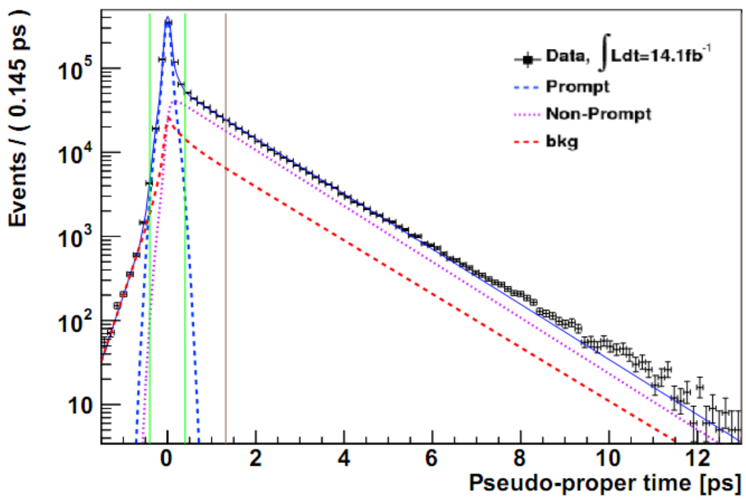

Figure 5.5.: Example of pseudo proper time plot for slice of p_{T} between 16-18 GeV. The area between the green lines represents the signal region, and all the data above the gray line represents the non-prompt + background region.

the the gray line in Figure 5.5). The reason the mass signal cut is include in this region is to reduce the background contamination.

The relative fractions of prompt/non-prompt/background in each region are shown in Figure 5.6.

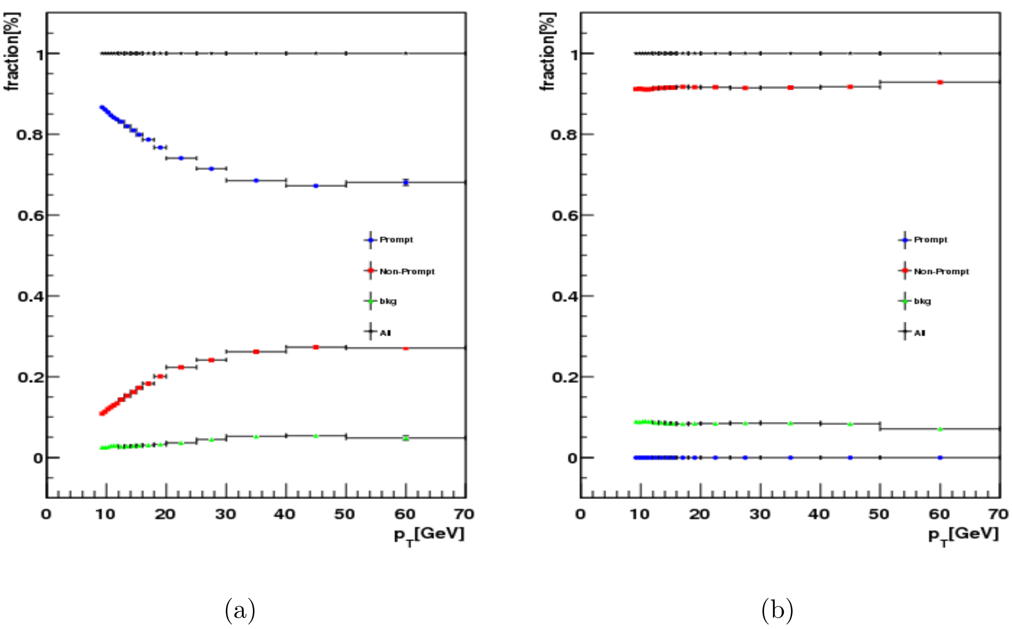

Figure 5.6.: Fraction of prompt J/ψ (blue), non-prompt J/ψ (red) and background (green) for: (a) signal region only and (b) non-prompt+background (without mass sidebands).

One concludes that in the signal region the prompt fraction slowly decreases from 90% to 70%. In the non-prompt + background sample we have above 90% non-prompt J/ψ in all the slices. Theses values are correlated with the selection cut. For tighter cuts on the signal region, the prompt fraction will be higher but it will cause statistic drop. In Chapter 7, the systematic impact of this phenomena on the measured J/ψ spin-alignment calculation is derived.

These measured ratios are used to obtain a relatively clean sample of prompt J/ψ for the spin-alignment measurement. For that purpose, the histogram of background only (H_bkg) in the angular distribution space are obtained, an example can be seen in Figure 5.7(a). For getting a histogram with non-prompt J/ψ only events (H_np), the histogram filled with events from region non-prompt + background is subtracted with the correct fraction of background from H_bkg. An example of non-prompt only histogram can be seen in Figure 5.7(b).

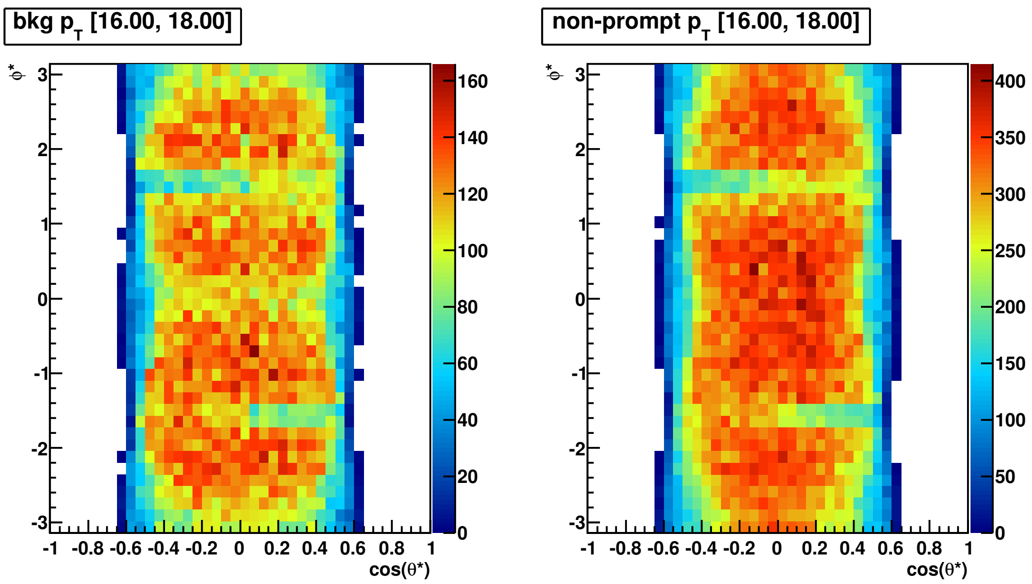

(a) (b)

Figure 5.7.: The angular distribution of the decay muons : (a) for the background only region and (b) for the non-prompt only candidates.

After the two high purity histograms, H_bkg and H_np are obtain, one can subtract from the signal region the fraction of non-prompt J/ψ and background events and get the required prompt J/ψ histogram. This procedure was preformed to each of the individual slices. On Figure 5.8(a) all candidates in the signal region are shown, and on Figure 5.8(b) only prompt candidates in the same region.

Figure 5.9 presents an example of the different ϕ^* projection for the signal region, prompt signal region, non-prompt region and background. It can be seen from this figure the different

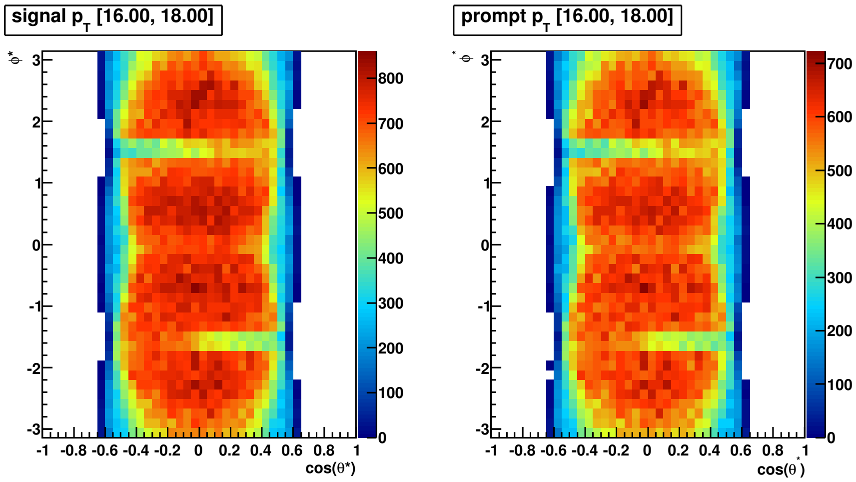

(a) (b)

Figure 5.8.: The angular distribution of the decay muons for the signal region: (right) all signal region, include contribution of prompt, non-prompt and background and (left) prompt event only, after subtracting the contributions of the non-prompt and background candidates.

angular behaviour and emphasise the important of getting clean prompt like sample. For example the acceptance of the *prompt* J/ψ at the edges of the ϕ^* distribution is lower than of the non-prompt sample. If we won't clean the sample properly, we will measure an average spin-alignment of different processes.

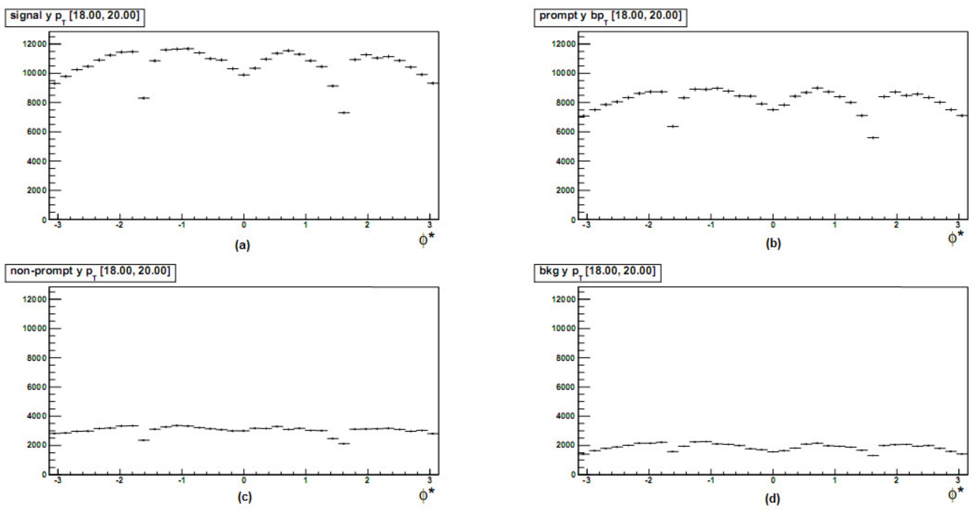

Figure 5.9.: Example of ϕ^* projection for the signal region and its components for p_{T} slice between 16-18 GeV. (a) the signal region (b) prompt J/ψ component (c) non-prompt J/ψ component (d) non-J/ψ component.

The rest of the slices (prompt only) that will be fitted later are shown in Figure 5.10.

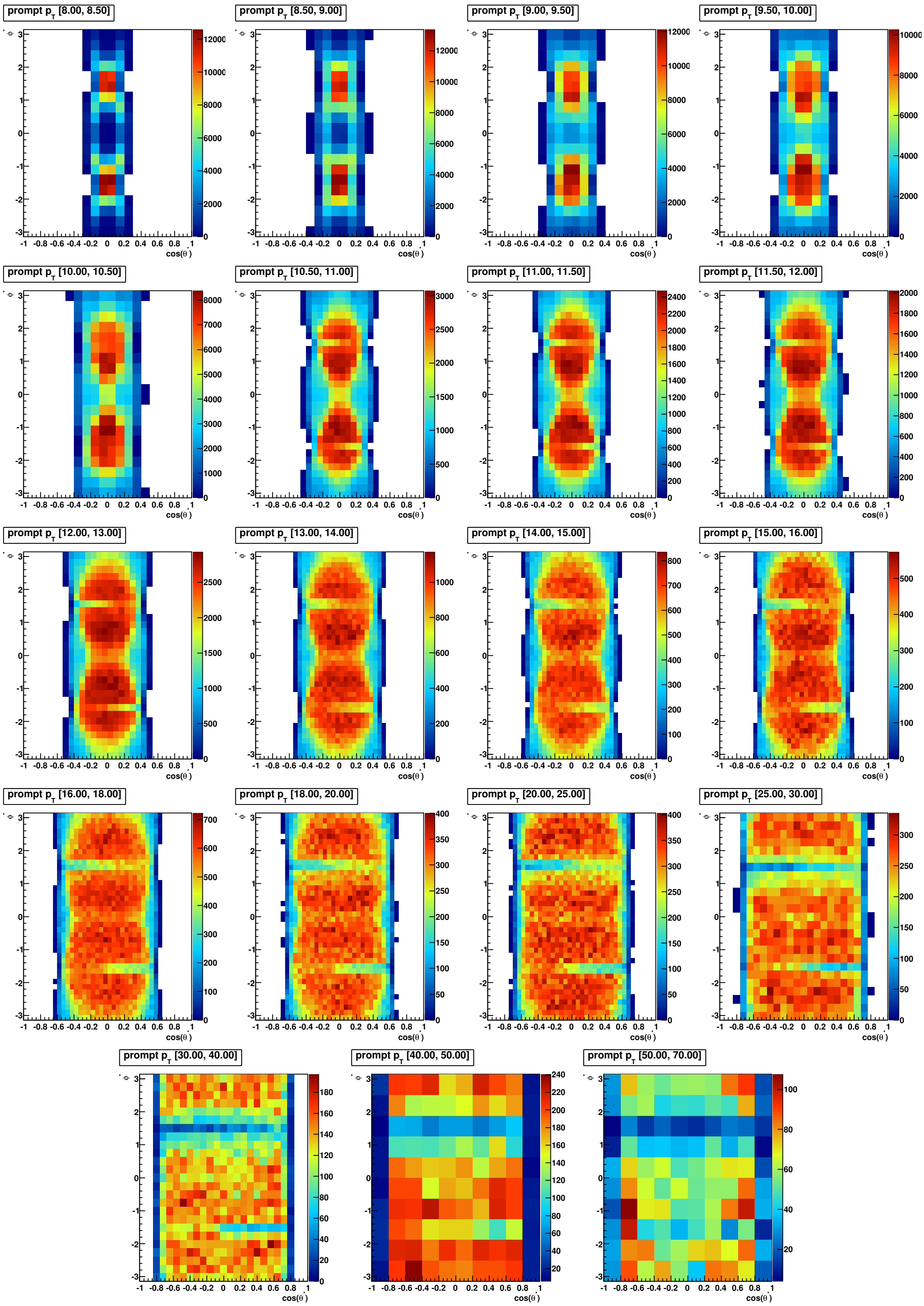

Figure 5.10.: J/ψ $cos\theta^*$ and ϕ^* distribution from 2012 data for all p_T slices, after removing non-prompt and background components. The plots are presented from the lowest p_T to the highest.

Chapter 6.

Spin-alignment analysis

Taking advantage of the large increase in integrated luminosity delivered by the LHC in 2012, this chapter describes the measurement of J/ψ spin-alignment in one intervals of absolute J/ψ rapidity and the full range of J/ψ transverse momentum.

For this part of the analysis, the same data samples that were described in chapter 4 are used, with additional cuts that will be describe below.

6.1. Reconstruction and trigger efficiencies

The efficiency of the offline reconstruction cuts for events with muons within the fiducial region is given by:

$$\epsilon_{reco} = \epsilon_{trk}(p^{\mu}_{T1}, \eta^{\mu}_{1}) \times \epsilon_{trk}(p^{\mu}_{T2}, \eta^{\mu}_{2}) \times \epsilon_{\mu}(p^{\mu}_{T1}, q_1 \cdot \eta^{\mu}_{1}) \times \epsilon_{\mu}(p^{\mu}_{T2}, q_2 \cdot \eta^{\mu}_{2}). \tag{6.1.1}$$

In this equation, the characteristics of the two muons are labelled with indices $1, 2$. The efficiency of the track selection cuts, ϵ_{trk} , for tracks originating from real muons is determined to be greater than 99% over the whole kinematic range with an associated systematic of $\pm 0.5\%$.

The efficiency to reconstruct a muon, ϵ_{μ}, is derived using a tag-and-probe method on $J/\psi \to \mu^+\mu^-$ data. Candidate events are required to pass one of a variety of single muon triggers with various p_T thresholds, thus allowing reconstruction of J/ψ candidates formed by a reconstructed muon and a good quality ID track. This technique provides a sample of muon candidates unbiased with respect to both trigger and offline reconstruction, and with favourable signal to background. Each event must contain at least three good quality tracks reconstructed in the Inner Detector. The *tag* muon corresponds to a muon candidate with p_{T}>4 GeV and $|\eta|$<2.4, that must have fired the single muon trigger in the event, as required by the trigger matching algorithms. The *probe* track is only required to pass the Inner Detector track quality, p_{T}, and η cuts and be consistent with having the same vertex as the identified tag muon.

The muon reconstruction efficiency is then derived in two-dimensional $p_T - q\eta$ bins (thirty muon p_{T} intervals and twenty-seven muon pseudorapidity (η) intervals). The ratio of the fitted $J/\psi \to \mu^+\mu^-$ signal yield for those probe tracks identified as muons to the fitted signal yield for all probe tracks in these double-differential intervals, is identified as the single muon reconstruction efficiency.

The final reconstruction efficiency map can be seen in Figure 6.1. More details about the generation of the map can be found in appendix B. For the purpose of calculating reconstruction scale factors to correct the MC samples, the same map was generated using MC events. Validation of the procedure was made and presented in appendix C.

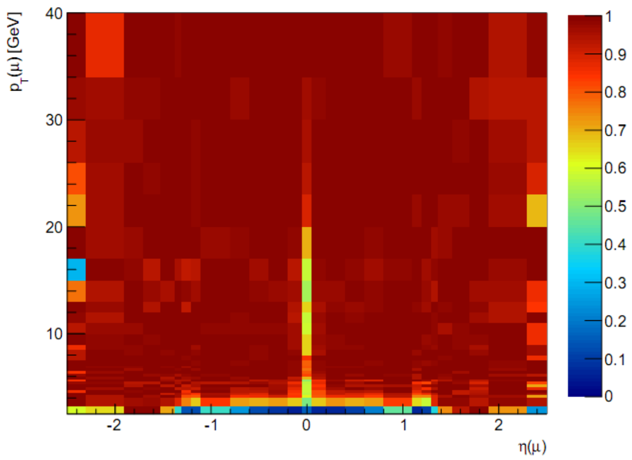

Figure 6.1.: The muon reconstruction efficiency map determined from 2012 data as a function of muon pseudorapidity and muon p_{T}.

The efficiency of the dimuon trigger to select events that have passed the offline selection criteria, ϵ_{trig} , is also calculated from data. It can be factorised into three terms:

$$\epsilon_{trig} = \epsilon_{RoI}(p^{\mu}_{T1}, q_1 \cdot \eta^{\mu}_1) \times \epsilon_{RoI}(p^{\mu}_{T2}, q_2 \cdot \eta^{\mu}_2) \times c_{\mu\mu}(\Delta R, |y^{\mu\mu}|) \tag{6.1.2}$$

where ϵ_{RoI} is the efficiency of the trigger system to find a Region of Interest (RoI) for a single muon with transverse momentum, p_{T} , and charge-signed pseudorapidity, $q\eta$, and $c_{\mu\mu}$ is a correction for effects related to the dimuon elements of the trigger. This correction accounts for the dimuon vertex and opposite charge cuts, and for loss of efficiency in the dimuon trigger if the two muons are close enough together to register only a single RoI.

The dimuon correction, $c_{\mu\mu}$, itself consists of two components

$$c_{\mu\mu}(\Delta R, y^{\mu\mu}) = c_a(y^{\mu\mu}) \times c_{\Delta R}(\Delta R, y^{\mu\mu}) \tag{6.1.3}$$

each evaluated in three separate regions of dimuon rapidity: barrel ($|y^{\mu\mu}| < 1.0$), transition ($1.0 < |y^{\mu\mu}| < 1.2$), and endcap ($1.2 < |y^{\mu\mu}| < 2.3$). The correction c_a is due to the effect of vertex and opposite charge requirement to the trigger, and is defined by the maximum efficiency for large dimuon angular separation. The asymptotic values are found using the fraction of candidate $J/\psi \to \mu^+\mu^-$ decays selected by the standard dimuon trigger to those selected by a similar dimuon trigger without any charge or vertex requirements. Figure 6.2 presents the c_a correction for the three rapidity sections. The last region, in the endcap, was fitted to polynomial function due to the decrease in efficiency.

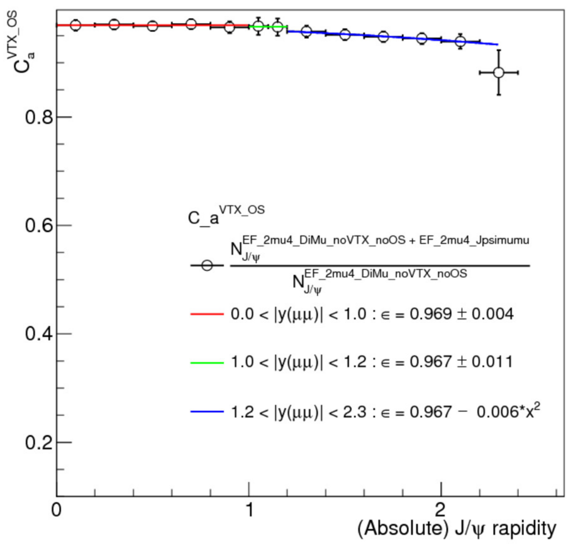

Figure 6.2.: c_a correction with respect to J/ψ absolute rapidity for the three rapidity regions, barrel ($|y^{\mu\mu}| < 1.0$), transition ($1.0 < |y^{\mu\mu}| < 1.2$), and endcap ($1.2 < |y^{\mu\mu}| < 2.3$)

The correction for efficiency loss due to the spatial separation of the muons, $c_{\Delta R}$, differs from unity only for those muon pairs with $\Delta R \lesssim 0.3$. This dependence on ΔR is extracted in the same three regions of dimuon rapidity as used for c_a from a sample of offline reconstructed dimuon events with $p_{\mathrm{T}}(\mu_2)$>8 GeV and 2< $M_{\mu\mu}$ <8 GeV (excluding the region around the J/ψ resonance, 2.9–3.3 GeV), selected using a single muon trigger with a threshold of 18 GeV. The 8 GeV requirement on the lower p_{T} muon is made to ensure that the efficiency to identify a 4 GeV ROI in the trigger system has reached its plateau value. The ΔR dependence of

$c_{\Delta R}$ is then extracted from a fit to the fraction of events in this control sample that also pass the dimuon trigger used in this analysis. Figure 6.3 present this correction for the 3 rapidity regions.

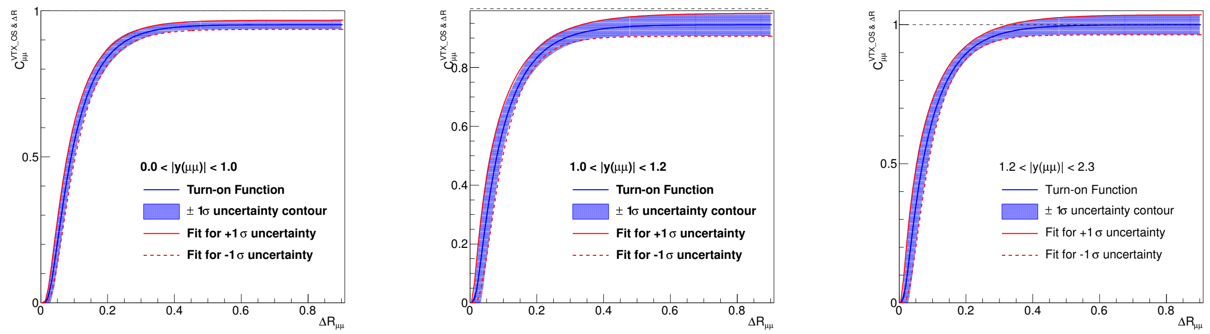

(a) (b) (c)

Figure 6.3.: $c_{\Delta R}$ correction, due to the spatial separation of the muons, for the full rapidity region. (a) barrel region (b) transition region (c) endcap region. This correction was made for the data trigger efficiency map. The blue envelopes represent the region of $\pm\sigma$ from the central value.

The final component of the dimuon trigger efficiency, ϵ_{RoI}, represents the single muon trigger efficiency with a threshold of p_{T}>4 GeV. It is measured using well reconstructed $J/\psi \to \mu\mu$ candidates in data that pass a single muon trigger (with a threshold of 18 GeV, 20 GeV, 24 GeV or 36 GeV). The ratio of the yield of J/ψ candidates (determined by fitting the invariant mass distributions) that pass both this single muon trigger and the 4 GeV p_T threshold dimuon trigger, used in this analysis, to the yield of J/ψ candidates that pass the single muon trigger (irrespective of whether the dimuon trigger also fires) is identified as the single muon trigger efficiency. In each case, the reconstructed muon(s) are matched to the muon(s) that triggered the event for each of the single or dimuon triggers. The number of candidates passing the dimuon trigger is then further corrected by c_a and $c_{\Delta R}$ for dimuon correlation effects[1]). The ratio of the dimuon trigger yield to the single muon one is identified as ϵ_{RoI} in the $p_{\mathrm{T}}(\mu)$ and $q\eta(\mu)$ interval considered.

The final trigger efficiency maps is presented in Figure 6.4.

In appendix A the full details and corrections are presented, and a comparison between data and MC correction is made. This method, described above, for deriving the trigger

[1]These corrections introduce a negligible anti-correlation between the measured values of ϵ_{RoI} and those of c_a and $c_{\Delta R}$.

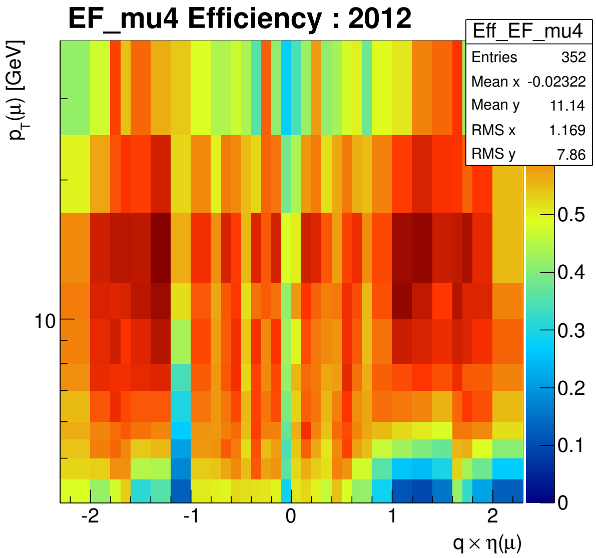

Figure 6.4.: The single muon trigger RoI efficiency, ϵ_{RoI}, for data of 2012 as a function of muon charge-signed pseudorapidity and muon p_{T}, to be queried for both muons and combined with the $c_{\mu\mu}(\Delta R, y^{\mu\mu})$ correction factor to arrive at the dimuon efficiency.

efficiency map and its corrections, was fully tested and confirmed using MC samples. Those tests are described in details in appendix C.

6.2. Monte-Carlo samples

To perform the measurement, the data shapes are compared to templates shapes produced from two different Monte-Carlo (MC) sample. One sample of $pp \to J/\psi \to \mu^+\mu^-$ were the minimum p_{T} for both muons is 4 GeV, generated with 10M events and approximate cross-section of 202.4 nb. The second sample is $pp \to J/\psi \to \mu^+\mu^-$ were the minimum p_{T} for both of the muons is 6.5 GeV, generated with 70M events and approximate cross-section of 29.65 nb.

The first sample, mostly populate the low p_{T} slices, and the second one represents a significantly higher luminosity and populate more the higher p_{T} slices. The first sample is used for measuring the J/ψ spin-alignment from the lowest p_{T} up to p_{T} of 20GeV. For higher p_{T} the second MC sample is used. Both samples are correctly re-weighted to the data luminosity (will be describe at 6.2.2). The selections criteria are the same as done for the data (described in chapter 4).

Table 6.1.: Total simulated J/ψ candidate after all selection criteria for each individual kinematic slice for the event filter trigger EF_2mu4T_Jpsimumu_L2StarB, for the two MC samples.

$p_T[GeV]$ slice	$J/\psi \to \mu(4)\mu(4)$ candidates	$J/\psi \to \mu(6.5)\mu(6.5)$ candidates	Total
8.0 - 8.5	28216	0	28216
8.5 - 9.0	47216	0	47216
9.0 - 9.5	58751	0	58751
9.5 - 10.0	63853	0	63853
10.0 - 10.5	64109	0	64109
10.5 - 11.0	61562	0	61562
11.0 - 11.5	57284	0	57284
11.5 - 12.0	52295	0	52295
12.0 - 13.0	88770	15795	104565
13.0 - 14.0	69700	450956	520656
14.0 - 15.0	54152	828408	882560
15.0 - 16.0	41161	913214	954375
16.0 - 18.0	55519	1613595	1669114
18.0 - 20.0	32888	1170073	1202961
20.0 - 25.0	35870	1508846	1544716
25.0 - 30.0	11574	555034	566608
30.0 - 40.0	5941	310705	316646
40.0 - 50.0	1180	63208	64388
50.0 - 70.0	397	21498	21895
8.0 - 70.0	830438	7451332	8281770

In Tabel 6.1 the total number of events after passing all the selection criteria for the dimuon trigger are presented, for both samples (before re-weighting). It can be seen from the table that from p_{T} slice of 13-14 GeV, the statistics of the second sample is much higher. The reason for not using this sample from this p_{T}, but only from p_{T} of 20 GeV, is due to lower statistics in the data (from the higher muon p_{T} cut), and more important is because of the lower $cos\theta^*$ acceptance in this region when applying the required muon p_{T} cut, which reduces the sensitivity of the measurement. In Figure 6.5 the $\cos\theta^*$ for the same J/ψ p_{T} slice is presented, one for each muons p_{T} cuts.

In the lower p_{T} slices, the $cos\theta^*$ suffers from low acceptance. For this reason it was decided at this stage to merge the low p_{T} slices to wider bins, and by that to gain acceptance and

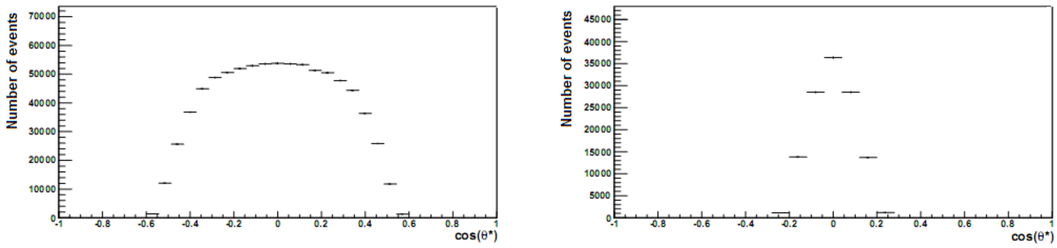

(a) (b)

Figure 6.5.: $cos\theta^{*}$ projection with different muons p_{T} cuts for J/ψ p_{T} slice of 14-15 GeV using 2012 data. (a) muons threshold of 4 GeV (b) muons threshold of 6.5 GeV.

higher sensitivity in measuring the polar parameter. In the medium p_{T} slices neighboring slices are merged to gain more statistics (in the higher region of the smaller MC sample). By merging the slices at this stage, one takes advantage of the accurate measurements of the fractions, using the finer slices, therefore getting more accurate and pure sample of prompt like candidates when merging the slices.

The new J/ψ p_{T} slices are: 9.0, 12.0, 14.0, 16.0, 18.0, 20.0, 25.0, 30.0, 40.0, 50.0, 70.0 GeV (total of 10 slices).

6.2.1. Templates

The template are produce in 2D-space of J/ψ $cos\theta^*$ and ϕ^* as defined in section 2.4 for the ten different J/ψ p_T slices. Since the MC samples are already produced using only direct J/ψ decays, one does not need to repeat the process of cleaning the sample from background and non-prompt J/ψ, like it was done for the data sample, but one needs to apply the same kinematic and reconstruction cuts as done in the data. In addition one needs to apply the same mass and pseudo proper-time cuts that were applied to the data for selecting the signal region.

The different templates for each of the slices, after applying all discussed cuts, can be seen in Figure 6.6.

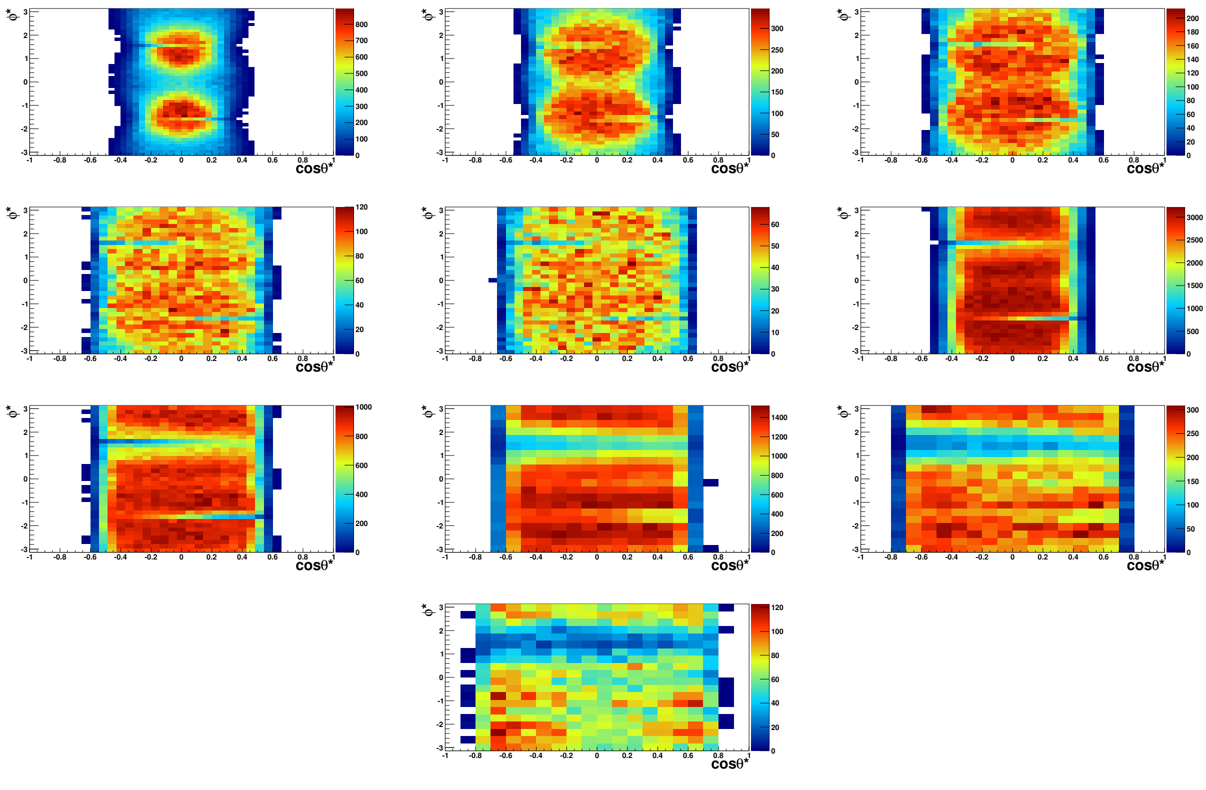

Figure 6.6.: J/ψ $cos\theta^*$ and ϕ^* templates for all p_T slices. The plots are ordered from the lowest p_T to the highest.

6.2.2. MC re-weighting

As the MC does not fully agree with the data, several corrections are required. These corrections are not preformed in the J/ψ angular space, in order not to bias the results (one expects differences in that space), but it is made using the more natural objects that construct the J/ψ, i.e. on the muons parameters.

The corrections that are applied to the MC samples:

- Cross-section correction - corrected to the data luminosity
- Pile-up correction
- Reconstruction efficiency scale factor
- Trigger efficiency scale factor

The two MC samples represent different luminosities. The smaller sample stands for luminosity of $47.86pb^{-1}$ and the bigger sample for luminosity of $2.36fb^{-1}$. These two samples used for the processes of prompt J/ψ so one should divide these values by the correct BR (of 5.8%) and get $0.825fb^{-1}(\mathcal{L}_4)$ and $40.6fb^{-1}$ $(\mathcal{L}_{6.5})$ respectively. The way the sample is corrected is as follow:

$$\omega_{\mathcal{L}} = \frac{\mathcal{L}_{data}}{\mathcal{L}_i} \tag{6.2.1}$$

where i equal 4 or 6.5.

In Figure 6.7 the $J/\psi(p_{\mathrm{T}})$ distribution before and after applying the correction are presented. It can be seen that after the correction, at p_{T} of 20 GeV, there is a small step in the distribution. This is expected and it is due to the higher muons p_{T} cut.

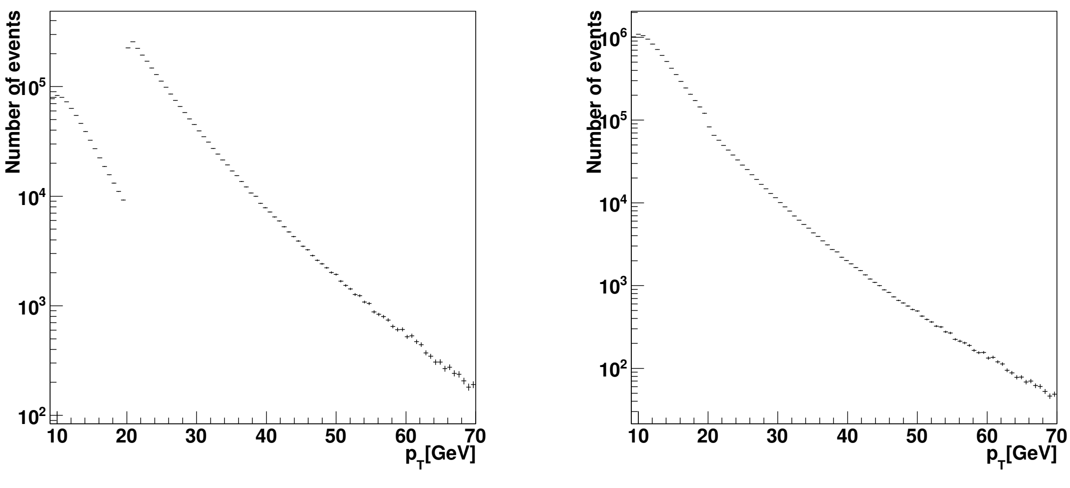

Figure 6.7.: J/ψ p_{T} distribution of MC. (a) when no correction are applied (b) after re-weighting to data luminosity.

Due to the increase of luminosity, there was also increase in pileup. Higher bunch densities caused more interactions to occur during the same bunch crossing, resulting in the products of many distinct interactions overlapping inside the detector. Figure 6.8 illustrates the increase in μ, the average number of interactions per bunch crossing, between 2011 and 2012.

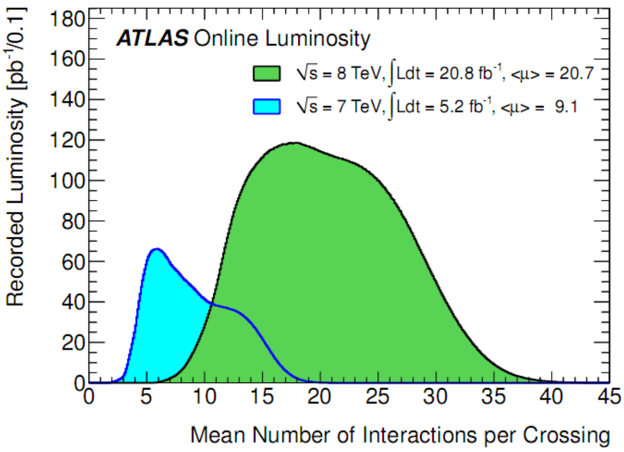

Figure 6.8.: Comparison of 2011($\sqrt{s} = 7TeV$) and 2012 ($\sqrt{s} = 8TeV$) pileup conditions. The yearly average number of interactions per bunch crossing, $< \mu >$, is given in the legend for both runs.

This effect makes the reconstruction and identification of physics objects more challenging. In addition, since MC samples are produced with a fixed set of pileup conditions, they do not necessarily mimic the pileup conditions eventually observed in the data. Instead of re-simulating every MC sample to mirror the observed pileup, each is re-weighted to match the pileup conditions observed in data. Figure 6.9 show the MC μ before and after re-weighting and the same parameter in our data sample.

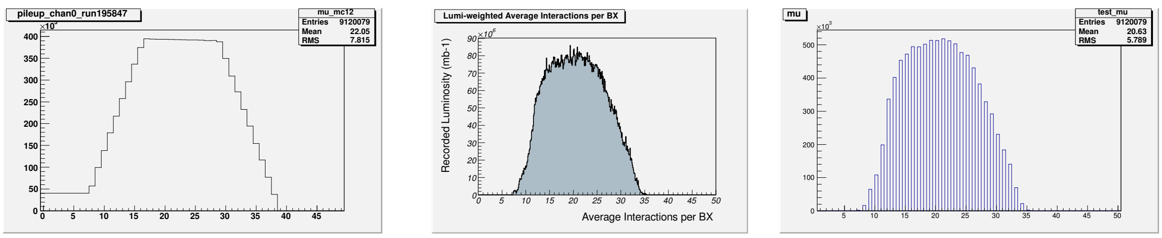

(a) (b) (c)

Figure 6.9.: average number of interactions per bunch crossing, $< \mu >$ (a) for the simulated MC (b) for 2012 data sample used in this analysis (c).re-weighted MC to mimic the data pileup condition.

The final two corrections correspond to the differences between the event reconstruction and trigger efficiency of data and MC. For that purpose, reconstruction and trigger efficiency maps for MC were generated, using the same procedure that was used for the data (see section 6.1). Later for each MC event we calculate two Scale Factors (SF), which are the ratio between the efficiency of data to the MC efficiency, one for reconstruction efficiency and one for trigger efficiency.

The Total correction coefficient applied to the MC on event by event base is:

$$\omega_{total} = \omega_{\mathcal{L}} \times \omega_{pileup} \times SF^{reco} \times SF^{trig} \tag{6.2.2}$$

The individual and overall weight corrections, calculated using the methods described above, are shown as function of $p_{\mathrm{T}}^{\mu\mu}$ and $|y^{\mu\mu}|$ in Figure 6.10.

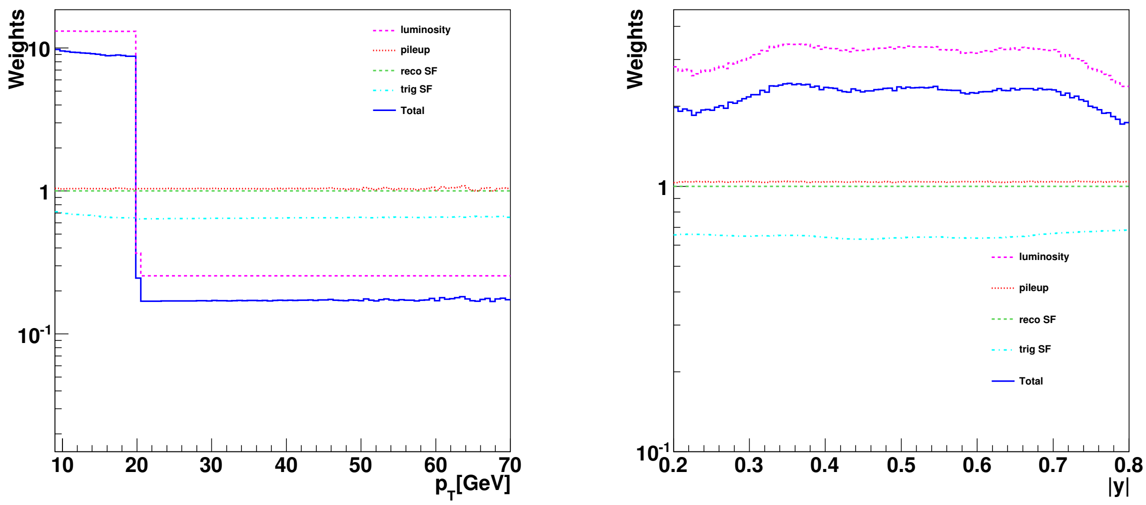

(a) (b)

Figure 6.10.: Individual and overall corrections for MC sample as a function of:(a) J/ψ p_{T} (b) J/ψ absolute rapidity. Dash purple line-luminosity weights, dash red line-pileup weights, dash green line-reconstruction SF weights, light blue line-trigger SF weights and blue line-total weights.

The largest contribution comes from the luminosity weight, but this correction is less significant because it will not affect the fit result (will be explained later).

Using these corrections, a comparison between data and MC is preformed. The comparison is done for the J/ψ parameter, p_{T} and rapidity.

From Figure 6.11 it can be seen that there is a very good agreement between the data and the smaller MC sample (up to 20 GeV), but for higher p_{T} there are more significant

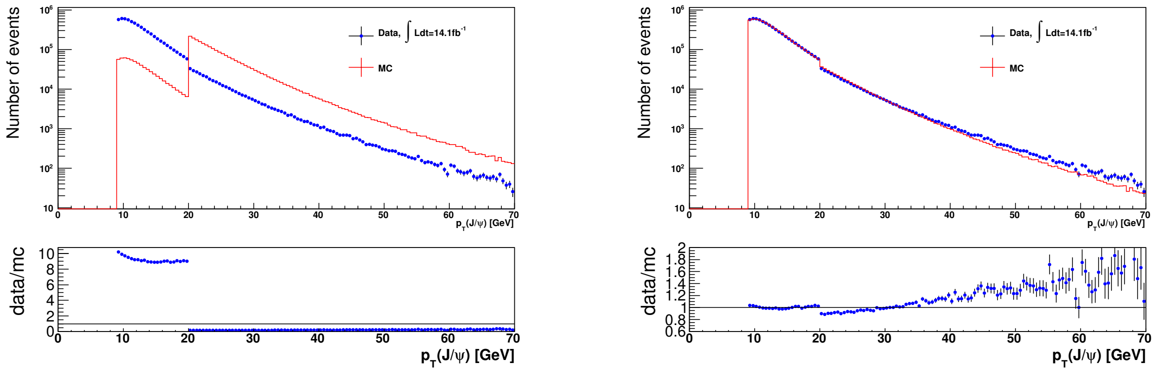

(a) (b)

Figure 6.11.: Comparison between data and MC of J/ψ p_{T} (a) before applying MC corrections (b) after all corrections made. At the bottom of each plot, a ratio of data to MC is plotted (black line represent the value 1.0).

discrepancies. These discrepancies rise from the estimation of the trigger efficiency at the higher p_{T} values, and is also observed at the closure tests (see appendix C).

When applying a correction to the trigger efficiency scale factor, by a linear function of the J/ψ p_{T} , the data fully agrees with MC in all the p_{T} range. Figure 6.12 shows the J/ψ p_{T} distribution after applying this additional correction. This discrepancy will be taken into account in the systematic study at chapter 7.

In addition, Figure 6.11(a) shows the difference in the statistics between the two MC sample (red curve). The low statistics in the region below 20 GeV will make the error coming from the model more dominant with respect to the statistical error of the data.

In the space of the J/ψ rapidity (Figure 6.13), after re-weighting the MC, one observes a good agreement between data and MC. No discrepancies are seen as in the p_{T} due to the averaging over p_{T} and most of the statistics are in the low p_{T} region where there are no discrepancies.

After applying all the corrections mentioned above, the final templates are ready for the fit. These templates can be seen in Figure 6.14.

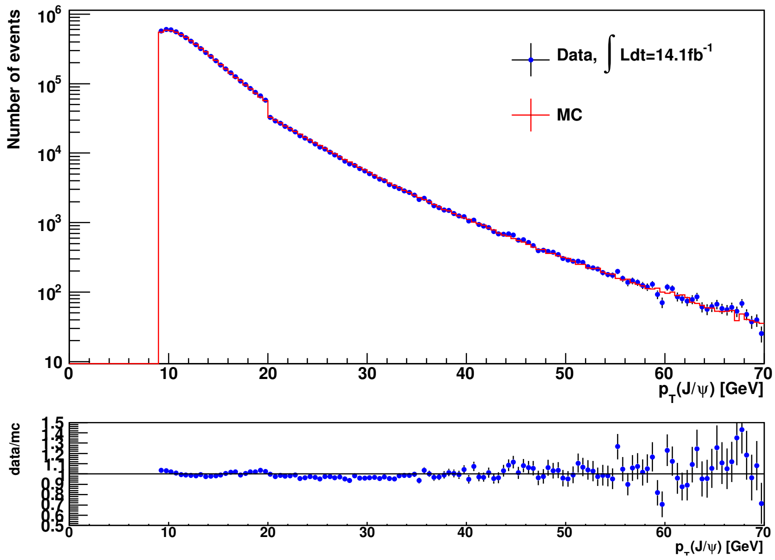

Figure 6.12.: Comparison between data and MC of J/ψ p_{T} after all corrections made with additional linear correction to the trigger scale factor. At the bottom of each plot, a ratio of data to MC is plotted (black line represent the value 1.0).

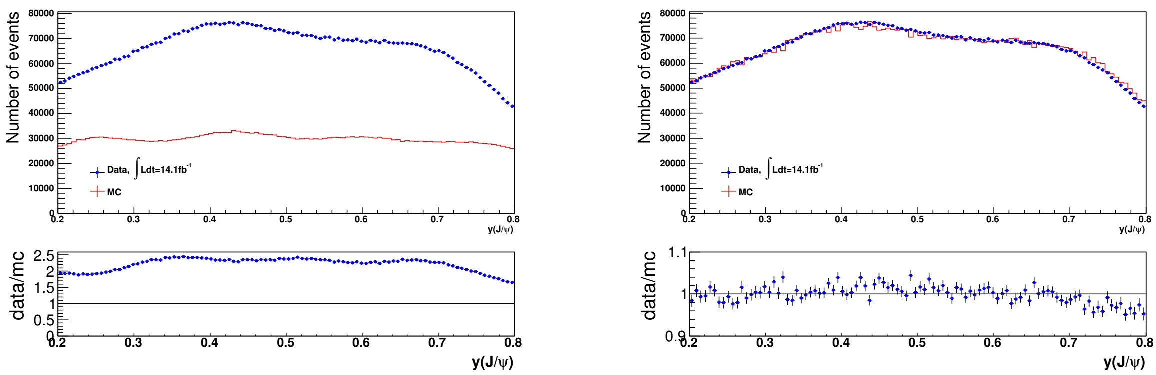

Figure 6.13.: Comparison between data and MC of J/ψ rapidity (a) before applying MC corrections (b) after all corrections made. At the bottom of each plot, a ratio of data to MC is plotted (black line represent the value 1.0).

6.3. Fit procedure

The aim is to measure the angular distribution of the decaying muons for prompt-J/ψ's as a function of its p_{T}. The theoretical formula is define in Eq. 2.4.7. The method the measurement is preformed is a χ^2 template fit. The data is divided into slices of p_{T} as described in section 4.1, and from that slices one extracts sub samples of prompt-like slices as explained in section 5.4.

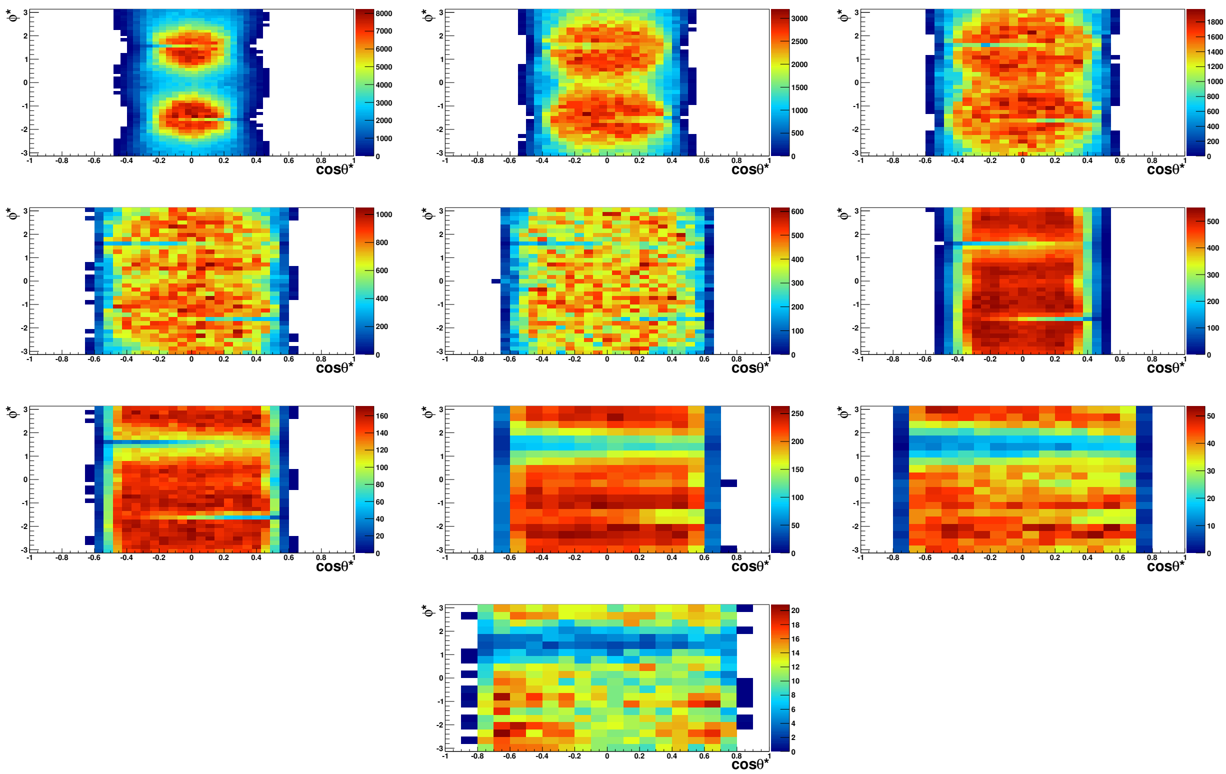

Figure 6.14.: J/ψ $cos\theta^*$ and ϕ^* template for all p_{T} slices after re-weighting for all the corrections mentioned in this section. The plots are ordered from the lowest p_{T} to the highest.

The same cut selections of mass window and pseudo proper time preformed to the data is preformed to the MC sample. The MC template are re-weighted for all the corrections described in section 6.2.2.

The χ^2 fit is define as:

$$\chi^2 = \sum_{i=1}^{n} \frac{[data_i - N_{sig} \cdot model(i, \lambda_{\theta^*}, \lambda_{\phi^*}, \lambda_{\theta^*\phi^*})]^2}{\sigma^2_{data_i} + \sigma^2_{model(i,\lambda_{\theta^*},\lambda_{\phi^*},\lambda_{\theta^*\phi^*})}} \tag{6.3.1}$$

The sum is over all the distribution bins (total n) for each p_{T} slice. N_{sig} is the total normalization of the MC and is one of the parameters of the fit. $\lambda_{\theta^*}, \lambda_{\phi^*}$ and $\lambda_{\theta^*\phi^*}$ are the parameters of the spin-alignment we aim to measure.

The $model(i\lambda_{\theta^*}, \lambda_{\phi^*}, \lambda_{\theta^*\phi^*})$ is composed of two components:

$$model(i, \lambda_{\theta^*}, \lambda_{\phi^*}, \lambda_{\theta^*\phi^*}) = \omega(\lambda_{\theta^*}, \lambda_{\phi^*}, \lambda_{\theta^*\phi^*}) \cdot template_i \tag{6.3.2}$$

where $template_i$ represent the i^{th} bin of the template and ω is the spin-alignment weight:

$$\omega(\lambda_i) = \frac{1}{1+\frac{\lambda_{\theta^*}}{3}} \cdot (1 + \lambda_{\theta^*} \cos^2\theta^* + \lambda_{\phi^*} \sin^2\theta^* \cos 2\phi^* + \lambda_{\theta^*\phi^*} \sin 2\theta^* \cos\phi^*) \tag{6.3.3}$$

$cos\theta^*$ and ϕ^* values are taken from the i^{th} bin of the MC template. $\sigma^2_{data_i}$ is the statistical error of the i^{th} bin and $\sigma^2_{model(i,\lambda_{\theta^*},\lambda_{\phi^*},\lambda_{\theta^*\phi^*})}$ is the error coming from both statistic of the MC and the error propagated from Eq. 6.3.3. Each step of the fit the λ's values are changed and the total χ^2 is re-calculated until it reach minimum.

In this method one has only four parameters which makes the fit procedure fast and efficient. The fit is performed using the ROOT framework (version `5.34/09`) using TMinuit Class for the minimization tool.

6.4. Results

This section describes the outcome results of the spin-alignment measurement. Figure 6.15 shows the $\cos\theta^*$ and ϕ^* projections of the fitted result, for lower p_{T} slice of p_{T} between 12-14 GeV. The red lines represent the fit projection and the gray bands represent the error from the model. It can be seen that the error from the model is more significant compared to the statistical error from the data (black points).

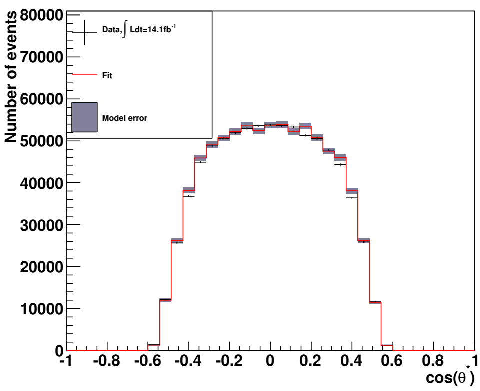

(a)

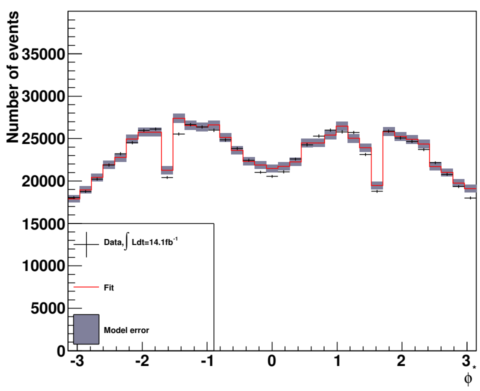

(b)

Figure 6.15.: Fit example for lower p_{T} slice (a) $cos\theta^*$ projection (b) ϕ^* projection. Black points represent the data and its statistical errors, red lines the fit result, and the gray bands represent the error propagation from the model.

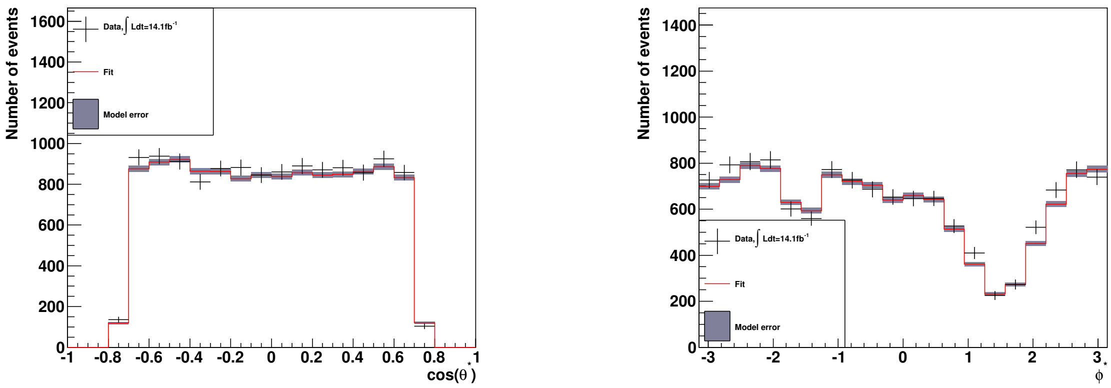

Figure 6.16.: Fit example for high p_{T} slice (a) $cos\theta^{*}$ projection (b) ϕ^{*} projection. Black points represent the data, red lines the fit result, and the gray bands represent the error propagation from the model.

Figure 6.16 depicts the fit result for the high p_{T} slice, with p_{T} in the range of 40-50 GeV. In this case the statistical error of the data is more significant. The rest of the fit projection plots can be found in appendix E.

The results for the three polarization parameters $\lambda_{\theta^{*}}$, $\lambda_{\phi^{*}}$ and $\lambda_{\theta^{*}\phi^{*}}$ with respect to the J/ψ p_{T} are presented in Figures 6.17 - 6.19. Table 6.2 summarize the fit results.

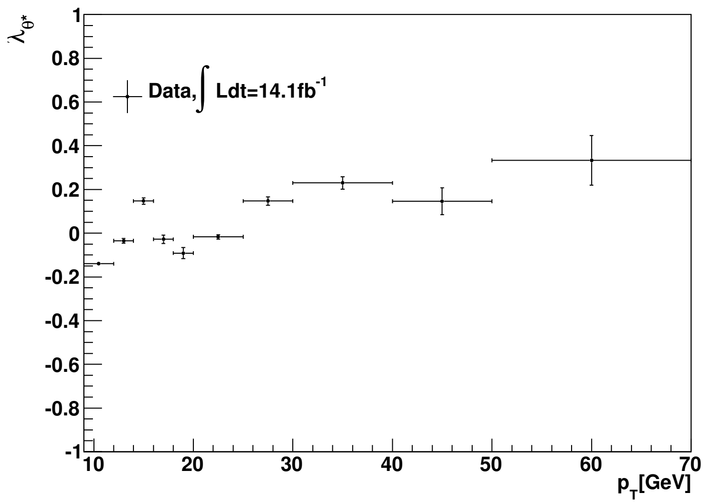

Figure 6.17.: Fit result for for $\lambda_{\theta^{*}}$ parameter with respect to the J/ψ p_{T}, for 2012 data using integrated luminosity of 14.1 fb^{-1}.

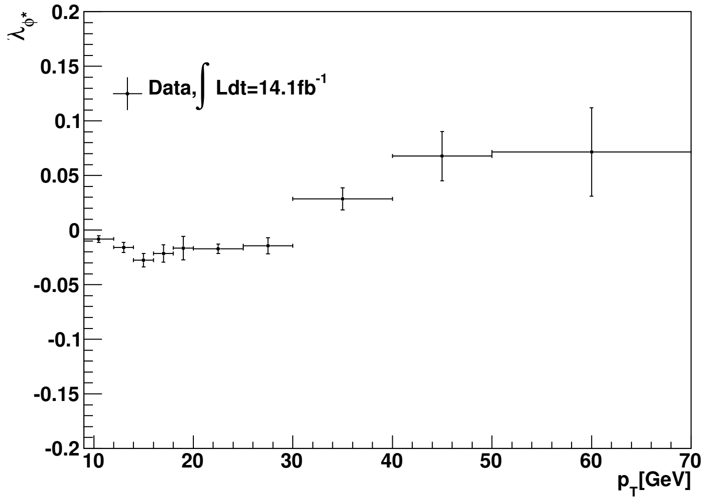

Figure 6.18.: Fit result for for λ_{ϕ^*} parameter with respect to the J/ψ p_{T}, for 2012 data using integrated luminosity of 14.1 fb^{-1}.

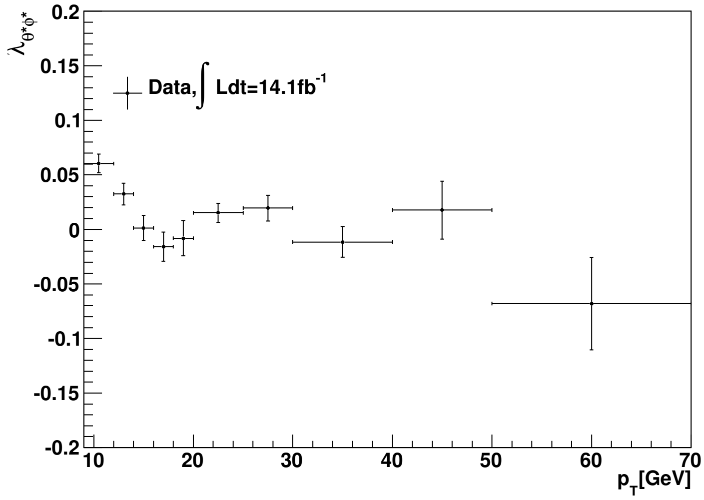

Figure 6.19.: Fit result for for $\lambda_{\theta^*\phi^*}$ parameter with respect to the J/ψ p_{T}, for 2012 data using integrated luminosity of 14.1 fb^{-1}.

The λ_{ϕ^*} and $\lambda_{\theta^*\phi^*}$ are very small throughout the whole p_{T} spectrum, were $\lambda_{\theta^*\phi^*}$ is consistent with zero in most of the bins. λ_{ϕ^*} is negative in the lower to mid p_{T} and with the increase of the p_{T} tends slightly to positive values. The polarization parameter, λ_{θ^*}, tends to negative values in the low p_{T} regions, and increase with p_{T} to higher positive values. All the results here include only statistical uncertainties.

The statistical uncertainty slightly grows with p_{T}, this is expected due to the lower statistics in data at higher p_{T} slices. The average statistical uncertainties for λ_{θ^*}, λ_{ϕ^*}, and $\lambda_{\theta^*\phi^*}$ are 0.031, 0.012 and 0.016 respectively.

The correlation coefficients found to be small between all three parameters, were the average values are 0.096, 0.012, and 0.015 for the correlations between $\lambda_{\theta^*-\phi^*}$, $\lambda_{\theta^*-\theta^*\phi^*}$ and $\lambda_{\phi^*-\theta^*\phi^*}$ respectively (the detailed list can be found in Table E.1).

Table 6.2.: Summarize of fit results for three polarization parameters for each p_{T} slices.

$p_T[GeV]$ slice	parameter	mean value	stat. uncertainty
	λ_{θ^*}	-0.1395	0.0064
$9 < p_T < 12$	λ_{ϕ^*}	-0.0081	0.0030
	$\lambda_{\theta^*\phi^*}$	0.0605	0.0086
	λ_{θ^*}	-0.035	0.010
$12 < p_T < 14$	λ_{ϕ^*}	-0.0158	0.0046
	$\lambda_{\theta^*\phi^*}$	0.033	0.010
	λ_{θ^*}	0.147	0.015
$14 < p_T < 16$	λ_{ϕ^*}	-0.0276	0.0061
	$\lambda_{\theta^*\phi^*}$	0.001	0.012
	λ_{θ^*}	-0.028	0.019
$16 < p_T < 18$	λ_{ϕ^*}	-0.0214	0.0080
	$\lambda_{\theta^*\phi^*}$	-0.016	0.013
	λ_{θ^*}	-0.091	0.026
$18 < p_T < 20$	λ_{ϕ^*}	-0.016	0.011
	$\lambda_{\theta^*\phi^*}$	-0.008	0.016
	λ_{θ^*}	-0.017	0.010
$20 < p_T < 25$	λ_{ϕ^*}	-0.0170	0.0043
	$\lambda_{\theta^*\phi^*}$	0.0153	0.0086
	λ_{θ^*}	0.147	0.019
$25 < p_T < 30$	λ_{ϕ^*}	-0.0144	0.0075
	$\lambda_{\theta^*\phi^*}$	0.020	0.012
	λ_{θ^*}	0.230	0.028
$30 < p_T < 40$	λ_{ϕ^*}	0.029	0.010
	$\lambda_{\theta^*\phi^*}$	-0.011	0.014
	λ_{θ^*}	0.146	0.061
$40 < p_T < 50$	λ_{ϕ^*}	0.068	0.023
	$\lambda_{\theta^*\phi^*}$	0.018	0.027
	λ_{θ^*}	0.33	0.11
$50 < p_T < 70$	λ_{ϕ^*}	0.072	0.041
	$\lambda_{\theta^*\phi^*}$	-0.068	0.042

In the next section one estimates the systematic uncertainties, and there one expects the opposite behavior, i.e. higher systematic uncertainties in the low p_{T} region, due to the lower statistics in the template samples in that region.

Chapter 7.

Systematics studies

In the following chapter the different systematic uncertainties for the spin-alignment analysis are discussed in details. For this part one investigates several cuts made in the analysis and the different weights applied to the MC, in order to search for possible biases.

The main systematic uncertainties are listed at the end of the chapter in Tables 7.5 - 7.7, and the final measurement results, including both statistical and systematics uncertainties are presented at Figures 7.8 - 7.10. A detailed description of the uncertainties are listed below.

7.1. Fit procedure

In order to test the fit procedure that is described in section 6.3, a dedicate toy MC tests were preformed. These tests were performed in the following way:

1. Generating toy samples using full MC sample that is weighted to the measured polarization in the data.
2. Each toy sample is generated with the same statistics as in the data sample
3. For each slice 1000 toy experiments were tested.

In these tests one wants to check two elements: possible biases in the measurement that are occurring due to the fit procedure, and to validate the statistical errors of the individual fits.

For each p_{T} slice one looks at the distribution of the fitted parameters (total of 1000 per slice) and fitted it to a Gaussian. The residual of the mean of the Gaussian to the mean value of the measurement (listed in Table 6.2) is taken as the systematic uncertainty of the fit procedure. The width of this distribution (The σ of the Gaussian) is compared to the statistical uncertainty of the measured values. The way it is compared is by fitting the pull distributions by a Gaussian, where the expected value of its width is 1.

In the case:

- $\sigma_{pull} > 1$, the fit error is underestimated
- $\sigma_{pull} < 1$, the fit error is overestimated

Figure 7.1 demonstrate the fitted parameter distributions from all the toy MC tests for two slices, and Figure 7.2 presents their corresponding pull distributions (the rest of the distributions can be found in appendix E).

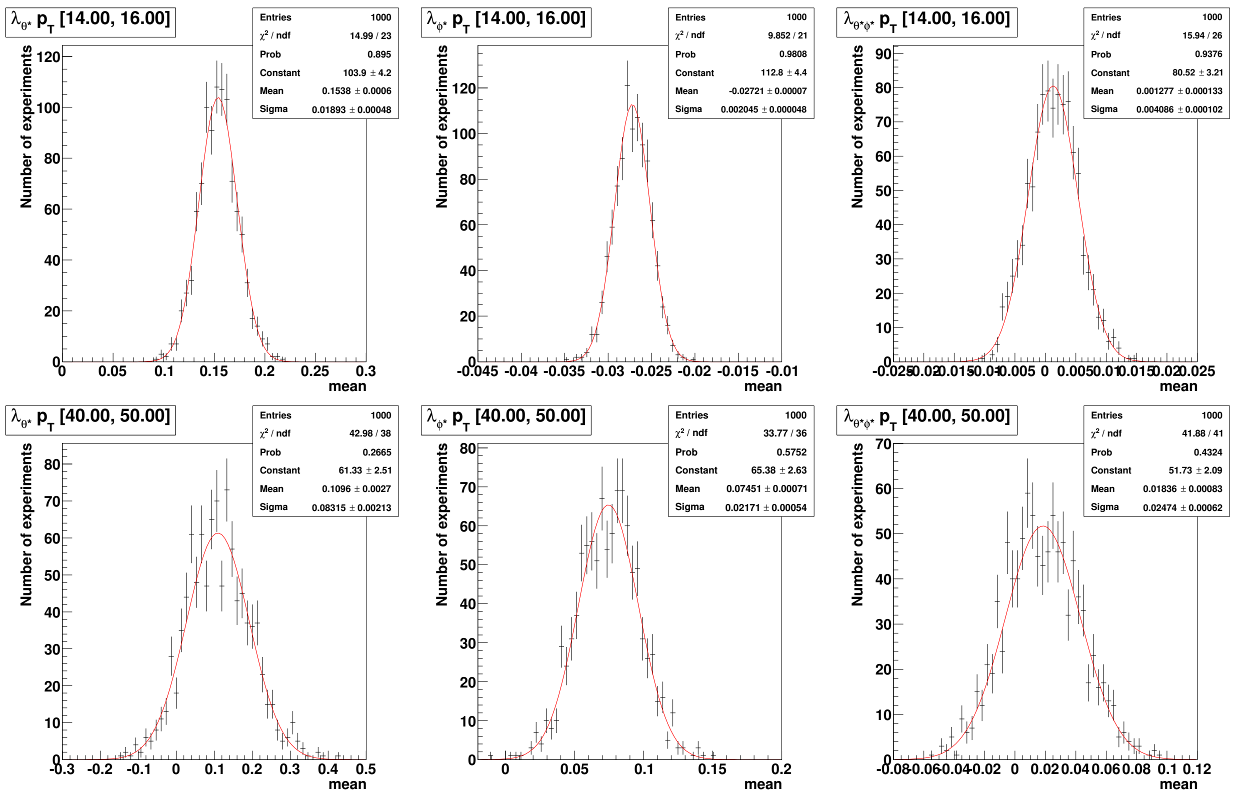

Figure 7.1.: An example of the spin-alignment parameters distributions for the toy MC tests. Each row represent different p_{T} slice, and each column represent the different parameter λ_{θ^*}, λ_{ϕ^*}, $\lambda_{\theta^*\phi^*}$ (in this order).

Table 7.1 summarize the systematic uncertainties due to the fit procedure. In addition the pull distribution width and the data statistical uncertainties are listed for comparison.

One can see from the table that for λ_{ϕ^*} and $\lambda_{\theta^*\phi^*}$, the error estimation is correct for the higher p_{T} slices, but for the lower p_{T} slices, one has overestimated the error by a factor of three. In all the p_{T} region, even if one takes into account the overestimation, and corrects the

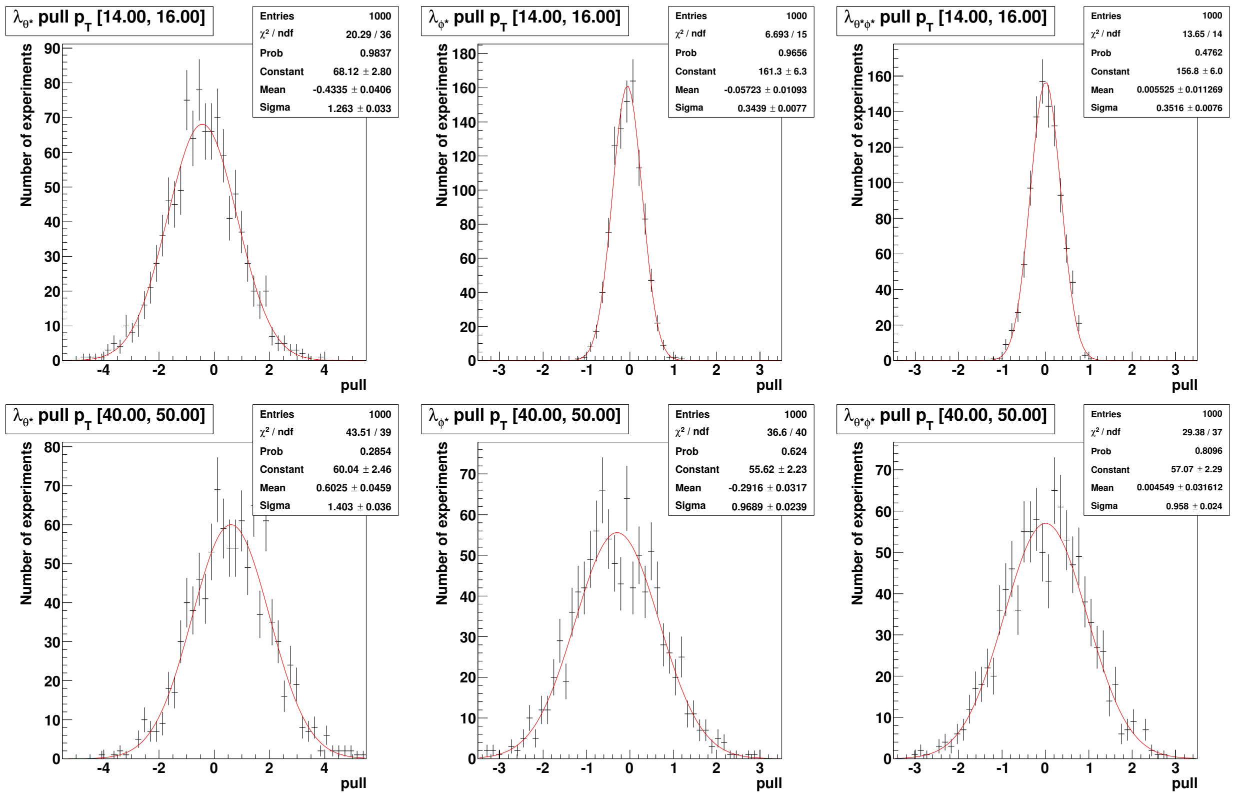

Figure 7.2.: An example of the polarization parameters pull distributions of the toy MC tests. Each row represent different p_{T} slice, and each column represent the different parameter λ_{θ^*}, λ_{ϕ^*}, $\lambda_{\theta^*\phi^*}$ (in this order).

errors, the systematic uncertainties are not as significant as the statistical errors. For the λ_{θ^*} parameter, the systematics uncertainties are low, and in some slices one has underestimate the statistical error. In the slices were the error estimate is derived appropriately the systematic uncertainty is negligible.

Figure 7.3 show the results of all toy MC experiment and their uncertainties.

7.2. Prompt selection

Here one estimates the systematic uncertainties arising from the procedure of selecting the prompt-like sample. There are two possible contributions, one from the fraction analysis, that define the fractions of each population, and the second from the selection cuts that define the signal region (see section 5.4).

Table 7.1.: Summary of the systematic uncertainties from the fit procedure for three polarization parameters for each p_{T} slices.

$p_T[GeV]$	parameter	sys. uncertainty	stat. uncertainty	σ_{pull}
	λ_{θ^*}	0.015	0.0064	2.7
$9 < p_T < 12$	λ_{ϕ^*}	0.000097	0.0030	0.32
	$\lambda_{\theta^*\phi^*}$	-0.00011	0.0086	0.32
	λ_{θ^*}	0.0086	0.010	1.6
$12 < p_T < 14$	λ_{ϕ^*}	0.00022	0.0046	0.35
	$\lambda_{\theta^*\phi^*}$	-0.00027	0.010	0.33
	λ_{θ^*}	0.0067	0.015	1.26
$14 < p_T < 16$	λ_{ϕ^*}	0.00035	0.0061	0.34
	$\lambda_{\theta^*\phi^*}$	-0.00010	0.012	0.35
	λ_{θ^*}	0.0098	0.019	1.02
$16 < p_T < 18$	λ_{ϕ^*}	0.00024	0.0080	0.35
	$\lambda_{\theta^*\phi^*}$	0.00037	0.013	0.34
	λ_{θ^*}	0.011	0.026	0.86
$18 < p_T < 20$	λ_{ϕ^*}	0.00015	0.011	0.36
	$\lambda_{\theta^*\phi^*}$	-0.00025	0.016	0.35
	λ_{θ^*}	-0.041	0.010	4.7
$20 < p_T < 25$	λ_{ϕ^*}	0.00015	0.0043	0.92
	$\lambda_{\theta^*\phi^*}$	0.00019	0.0086	0.97
	λ_{θ^*}	-0.042	0.019	2.7
$25 < p_T < 30$	λ_{ϕ^*}	0.0015	0.0075	0.98
	$\lambda_{\theta^*\phi^*}$	0.00050	0.012	0.94
	λ_{θ^*}	-0.021	0.028	1.92
$30 < p_T < 40$	λ_{ϕ^*}	0.00055	0.010	0.96
	$\lambda_{\theta^*\phi^*}$	-0.00030	0.014	0.94
	λ_{θ^*}	-0.036	0.061	1.4
$40 < p_T < 50$	λ_{ϕ^*}	0.0067	0.023	0.97
	$\lambda_{\theta^*\phi^*}$	0.00052	0.027	0.96
	λ_{θ^*}	0.047	0.11	1.18
$50 < p_T < 70$	λ_{ϕ^*}	0.017	0.041	0.99
	$\lambda_{\theta^*\phi^*}$	-0.0071	0.042	0.99

The first one found to be negligible, the reason is due to the low statistical uncertainty in the fraction parameters (see Table D.1). The average error of the prompt fraction(f_{prompt}) is less than 0.2%.

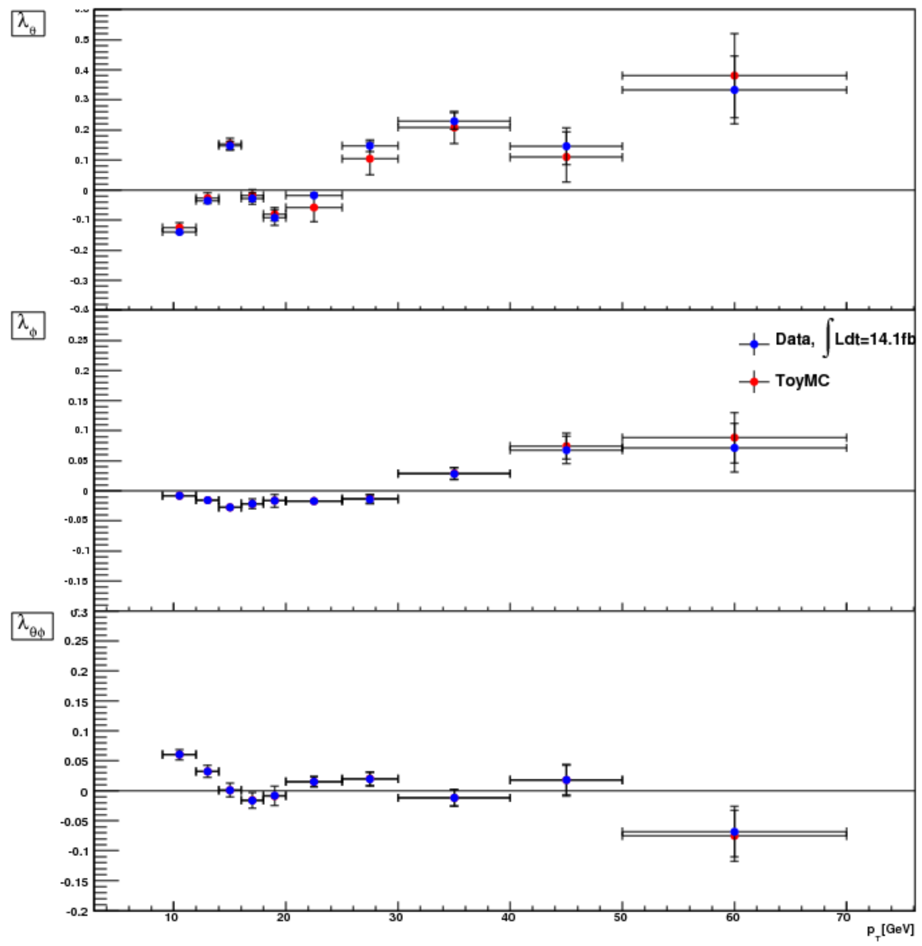

Figure 7.3.: Results of the toy MC for all three parameters. In red are the mean values of the toy experiments, and their statistical uncertainties, and in blue are the data results.

The signal region was defined by a mass cut of 3σ around the J/ψ peak and in the pseudo proper time, 3σ of the area of the signal prompt PDF. The way one tests this systematic is by shifting these cuts by $\pm\sigma$, each time in one space (mass or τ). These cuts define the purity of the sample for prompt-like candidates.

Figure 7.4 depicts the impact of shifting the mass cut by $\pm\sigma$ on the fractions of the different populations in the signal region. It can be seen that the stronger this cut is the purer the sample is, i.e. the fraction of prompt J/ψ increases. The downfall is that the overall statistics decreases.

The effect of the cut on the pseudo proper time on the fraction is more dramatic, as seen in Figure 7.5. Again, the tighter this cut is, the fraction of prompt J/ψ is higher.

The results of this study is summarized in Table 7.2

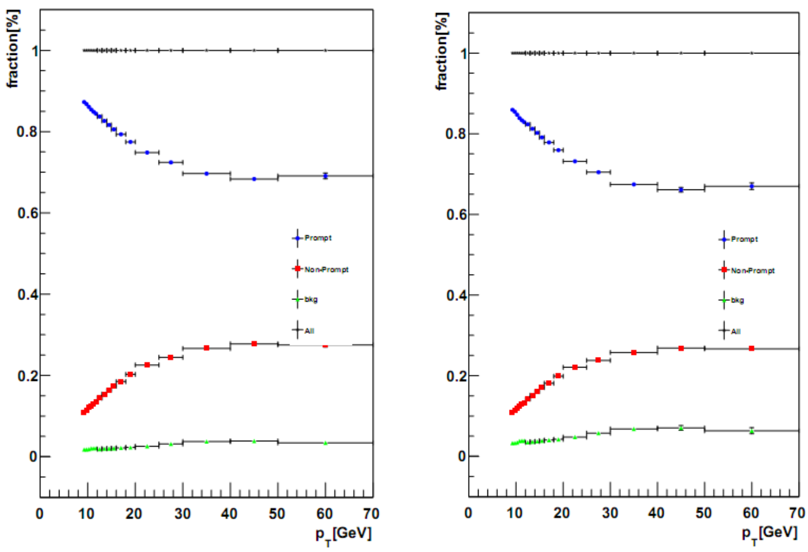

(a) (b)

Figure 7.4.: Changes in fractions with respect to the size of mass window (a) mass cut of 2σ around the J/ψ mass peak (b) mass cut of 4σ around the J/ψ mass peak. Blue is the prompt fraction, red is the non-prompt fraction and green is the non J/ψ background.

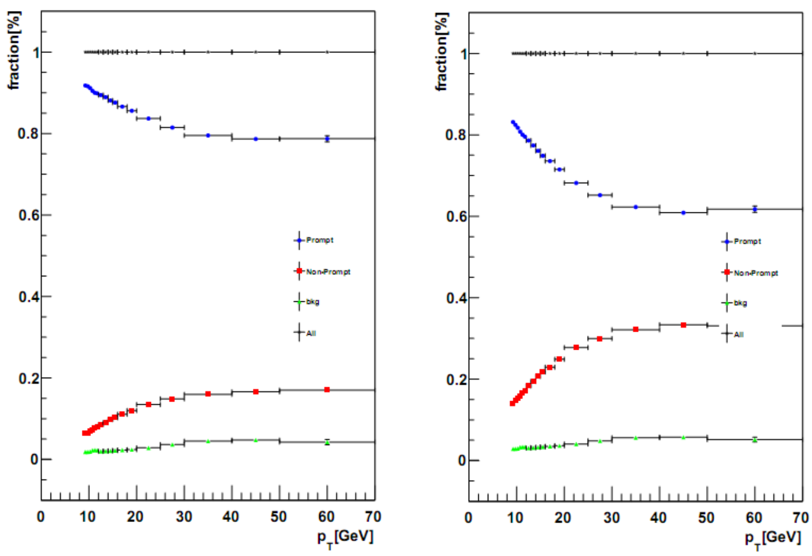

(a) (b)

Figure 7.5.: Changes in fractions with respect to the size of pseudo proper time window (a) τ cut of 2σ (b) τ cut of 4σ. Blue is the prompt fraction, red is the non-prompt fraction and green is the non J/ψ background.

The average systematic uncertainty for λ_{θ^*},λ_{ϕ^*}, and $\lambda_{\theta^*\phi^*}$ due to the mass window cuts are (+0.012,-0.013),(+0.0020,-0.00080), and (+0.0011,-0.0018) respectively, and due to the τ window are (+0.016,-0.0097),(+0.037,-0.014), and (+0.054,-0.0023). By comparing to the

Table 7.2.: Summary of the systematic uncertainties from the cut selection of the signal region for each p_{T} slices.

$p_T[GeV]$	parameter	sys. mass window	sys. τ window	total
$9 < p_T < 12$	λ_{θ^*}	$^{+0.000}_{-0.020}$	$^{+0.031}_{-0.0070}$	$^{+0.031}_{-0.021}$
	λ_{ϕ^*}	$^{+0.00018}_{-0.0023}$	$^{+0.0022}_{-0.012}$	$^{+0.0022}_{-0.012}$
	$\lambda_{\theta^*\phi^*}$	$^{+0.0011}_{-0.0000}$	$^{+0.0035}_{-0.00015}$	$^{+0.0037}_{-0.00015}$
$12 < p_T < 14$	λ_{θ^*}	$^{+0.0075}_{-0.0037}$	$^{+0.000}_{-0.017}$	$^{+0.0075}_{-0.017}$
	λ_{ϕ^*}	$^{+0.000030}_{-0.00048}$	$^{+0.0029}_{-0.012}$	$^{+0.0029}_{-0.012}$
	$\lambda_{\theta^*\phi^*}$	$^{+0.0000}_{-0.0012}$	$^{+0.00000}_{-0.00054}$	$^{+0.0000}_{-0.0013}$
$14 < p_T < 16$	λ_{θ^*}	$^{+0.0089}_{-0.0081}$	$^{+0.0000}_{-0.0089}$	$^{+0.0089}_{-0.012}$
	λ_{ϕ^*}	$^{+0.0000}_{-0.0012}$	$^{+0.0030}_{-0.013}$	$^{+0.0030}_{-0.013}$
	$\lambda_{\theta^*\phi^*}$	$^{+0.00011}_{-0.00050}$	$^{+0.00096}_{-0.0030}$	$^{+0.00097}_{-0.0030}$
$16 < p_T < 18$	λ_{θ^*}	$^{+0.0057}_{-0.014}$	$^{+0.011}_{-0.000}$	$^{+0.012}_{-0.014}$
	λ_{ϕ^*}	$^{+0.00000}_{-0.00061}$	$^{+0.00035}_{-0.016}$	$^{+0.00035}_{-0.016}$
	$\lambda_{\theta^*\phi^*}$	$^{+0.00039}_{-0.0018}$	$^{+0.0000}_{-0.0054}$	$^{+0.00039}_{-0.0057}$
$18 < p_T < 20$	λ_{θ^*}	$^{+0.014}_{-0.000}$	$^{+0.026}_{-0.024}$	$^{+0.030}_{-0.024}$
	λ_{ϕ^*}	$^{+0.00000}_{-0.00098}$	$^{+0.0027}_{-0.0032}$	$^{+0.0027}_{-0.0033}$
	$\lambda_{\theta^*\phi^*}$	$^{+0.00024}_{-0.00027}$	$^{+0.0092}_{-0.0000}$	$^{+0.0092}_{-0.00027}$
$20 < p_T < 25$	λ_{θ^*}	$^{+0.011}_{-0.012}$	$^{+0.0022}_{-0.0054}$	$^{+0.011}_{-0.013}$
	λ_{ϕ^*}	$^{+0.0020}_{-0.0013}$	$^{+0.0047}_{-0.017}$	$^{+0.0051}_{-0.017}$
	$\lambda_{\theta^*\phi^*}$	$^{+0.0030}_{-0.0000}$	$^{+0.0020}_{-0.0065}$	$^{+0.0036}_{-0.0065}$
$25 < p_T < 30$	λ_{θ^*}	$^{+0.0072}_{-0.019}$	$^{+0.0084}_{-0.0091}$	$^{+0.011}_{-0.021}$
	λ_{ϕ^*}	$^{+0.0010}_{-0.0000}$	$^{+0.000}_{-0.017}$	$^{+0.0010}_{-0.017}$
	$\lambda_{\theta^*\phi^*}$	$^{+0.00083}_{-0.0037}$	$^{+0.0011}_{-0.0034}$	$^{+0.0014}_{-0.0050}$
$30 < p_T < 40$	λ_{θ^*}	$^{+0.0038}_{-0.029}$	$^{+0.047}_{-0.011}$	$^{+0.047}_{-0.031}$
	λ_{ϕ^*}	$^{+0.0024}_{-0.00021}$	$^{+0.0012}_{-0.022}$	$^{+0.0027}_{-0.022}$
	$\lambda_{\theta^*\phi^*}$	$^{+0.0000}_{-0.0048}$	$^{+0.012}_{-0.0038}$	$^{+0.012}_{-0.0061}$
$40 < p_T < 50$	λ_{θ^*}	$^{+0.0079}_{-0.0075}$	$^{+0.024}_{-0.000}$	$^{+0.025}_{-0.0075}$
	λ_{ϕ^*}	$^{+0.00076}_{-0.00082}$	$^{+0.016}_{-0.019}$	$^{+0.016}_{-0.019}$
	$\lambda_{\theta^*\phi^*}$	$^{+0.0000}_{-0.0055}$	$^{+0.014}_{-0.000}$	$^{+0.014}_{-0.0055}$
$50 < p_T < 70$	λ_{θ^*}	$^{+0.055}_{-0.020}$	$^{+0.0097}_{-0.015}$	$^{+0.056}_{-0.025}$
	λ_{ϕ^*}	$^{+0.014}_{-0.000}$	$^{+0.0038}_{-0.0097}$	$^{+0.015}_{-0.0097}$
	$\lambda_{\theta^*\phi^*}$	$^{+0.0052}_{-0.0000}$	$^{+0.011}_{-0.000}$	$^{+0.012}_{-0.000}$

statistical error one can conclude that for the λ_{θ^*}, on average, these systematic uncertainties are within the statistical error, but for λ_{ϕ^*}, and $\lambda_{\theta^*\phi^*}$ the systematic uncertainty is more significant.

7.3. Detector resolution

Due to the detectors resolution, the measurement of the muons p_{T} can shift from its real value. In this rapidity region, the detector resolution is found to be:

$$\frac{\sigma_{p_{\mathrm{T}}}}{p_{\mathrm{T}}} = 0.0005 \tag{7.3.1}$$

In order to test a bias from this effect, for each MC event, one has re-calculated the two muons momenta, by picking a random number from a Gaussian distribution with the corresponding $\sigma_{p_{\mathrm{T}}}$ around the measured value.

From these two new muons one reconstructs the shifted J/ψ and its properties. The systematic results for this effect are found to be very small. For the λ_{θ^*} an order of magnitude smaller than the statistical error, and for the λ_{ϕ^*} and $\lambda_{\theta^*\phi^*}$ smaller by two to three orders of magnitude.

7.4. Pileup

One of the MC weights applied in the analysis, is to correct for the event pileup effect, due to the increase in luminosity (see section 6.2.2). The way to check for biases caused by this correction is by conservatively running the analysis with or without applying this correction. This systematic effect is found to be negligible for λ_{ϕ^*}, and $\lambda_{\theta^*\phi^*}$. For the λ_{θ^*} it was found to be negligible for the higher p_{T} slices (using the larger MC sample) , but not for lower p_{T} slices. The results for λ_{θ^*} are summarized in Table 7.3.

7.5. Trigger scale factor

For testing for a potential biases due to the trigger scale factor one needs to distinguish between the trigger weights for the three contributions:

- Efficiency of the first muon
- Efficiency of the second muon
- $c_{\mu\mu}$ correction, which takes into account the correlation between the two muons

Table 7.3.: Summary of the systematic uncertainties from pileup MC re-weighting.

$p_T[GeV]$	parameter	sys. uncertainty	stat. uncertainty
$9 < p_T < 12$	λ_{θ^*}	-0.0096	0.0064
$12 < p_T < 14$	λ_{θ^*}	-0.051	0.010
$14 < p_T < 16$	λ_{θ^*}	-0.040	0.015
$16 < p_T < 18$	λ_{θ^*}	-0.046	0.019
$18 < p_T < 20$	λ_{θ^*}	-0.015	0.026
$20 < p_T < 25$	λ_{θ^*}	0.00048	0.010
$25 < p_T < 30$	λ_{θ^*}	-0.0032	0.019
$30 < p_T < 40$	λ_{θ^*}	-0.0041	0.028
$40 < p_T < 50$	λ_{θ^*}	-0.0063	0.061
$50 < p_T < 70$	λ_{θ^*}	-0.0022	0.11

For the first two cases, the way the systematic was tested is by shifting the efficiency maps by $\pm\sigma$, correct the scale factors, and comparing the polarization yields to the central values. It was preformed separately for each case.

The same procedure was done for the $c_{\mu\mu}$ correction, where for each event the $c_{\mu\mu}$ was shifted by $\pm\sigma$. The $c_{\mu\mu}$ and its σ can be seen in Figure 6.3. The total systematic arising from the trigger will be the quadratic sum of all three components.

An example of the effect of shifting the efficiency of the first muon by $\pm\sigma$ to the J/ψ p_{T} distribution is presented in Figure 7.6. The change in the rapidity distribution is presented in Figure 7.7

The plots show the shifts of the MC distributions on the two sides of the data distributions. From the ratio plots, it can be seen that these shifts are not uniform over the p_{T} or rapidity, nor by magnitude or by direction. Table 7.4 summarized the results.

From the result one can learn that the $c_{\mu\mu}$ correction systematic uncertainty is negligible compared to the total scale factor systematics. In addition the systematic uncertainty for λ_{ϕ^*} and $\lambda_{\theta^*\phi^*}$ are very small throughout the full p_{T} range. For the λ_{θ^*}, this systematic is the most significant. In the p_{T} region up 30 GeV, this uncertainty dominates the statistical error by at least one order of magnitude. At higher p_{T} slices the systematic is within the statistical error, and even negligible.

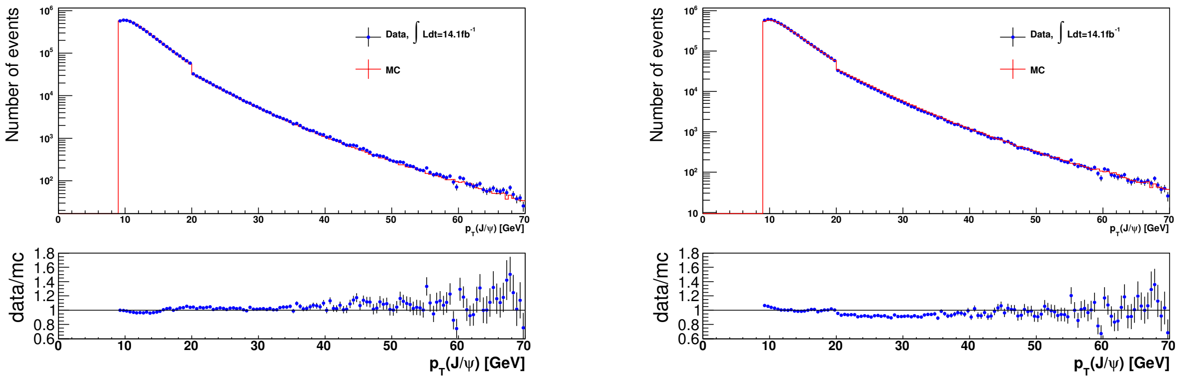

(a) (b)

Figure 7.6.: J/ψ p_{T} comparison between data and MC after shifting the trigger efficiency of the first muon by (a) $+\sigma$ (b) $-\sigma$. The bottom plots are the ratio between data to MC.

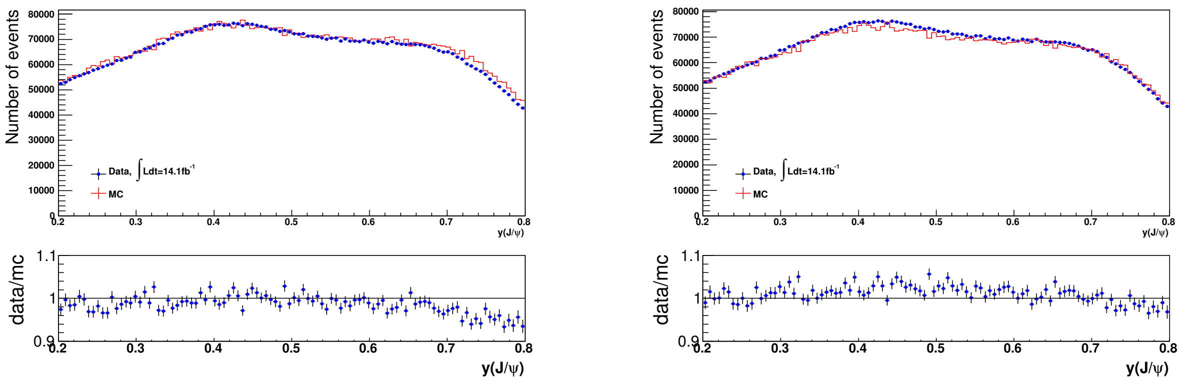

(a) (b)

Figure 7.7.: J/ψ rapidity comparison between data and MC after shifting the trigger efficiency of the first muon by (a) $+\sigma$ (b) $-\sigma$. The bottom plots are the ratio between data to MC.

Another potential systematic source that was tested corresponds to the luminosity weight given to the MC. It is found that it is not affecting the measurement and since it is just a normalization factor, that is different to each of the MC samples (since one does not mix the two samples in common slices). When changing this weight, the only changing parameter is the total normalization N_{sig} (see Eq. 6.3.1).

Finally the systematic uncertainty arising from the area of low efficiency is tested in the $\phi^* = \pm\pi/2$, that is discussed in section 4.3. The way it was tested is by excluding the low efficiency regions from the fit. It was determine by excluding the region of ± 0.1 around $\phi^* = \pm\pi/2$. It showed no significant biases in all the p_{T} region, and for all 3 parameters.

Table 7.4.: Summary of the systematic uncertainties arising from the trigger efficiecny scale factor for each p_{T} slices.

$p_T[GeV]$	parameter	sys. SF(μ_1)	sys. SF(μ_2)	sys. SF($c_{\mu\mu}$)	total sys.
$9 < p_T < 12$	λ_{θ^*}	$^{+0.072}_{-0.067}$	$^{+0.26}_{-0.21}$	$^{+0.00088}_{-0.00059}$	$^{+0.27}_{-0.22}$
	λ_{ϕ^*}	$^{+0.0022}_{-0.0032}$	$^{+0.0058}_{-0.0073}$	$^{+0.000002}_{-0.000001}$	$^{+0.0062}_{-0.0080}$
	$\lambda_{\theta^*\phi^*}$	$^{+0.00058}_{-0.00035}$	$^{+0.0020}_{-0.0016}$	$^{+0.000006}_{-0.000004}$	$^{+0.0021}_{-0.0017}$
$12 < p_T < 14$	λ_{θ^*}	$^{+0.041}_{-0.066}$	$^{+0.17}_{-0.15}$	$^{+0.0014}_{-0.0016}$	$^{+0.1700}_{-0.16}$
	λ_{ϕ^*}	$^{+0.0020}_{-0.0028}$	$^{+0.0025}_{-0.0030}$	$^{+0.000004}_{-0.000005}$	$^{+0.0033}_{-0.0041}$
	$\lambda_{\theta^*\phi^*}$	$^{+0.000046}_{-0.000072}$	$^{+0.00056}_{-0.00050}$	$^{+0.000007}_{-0.000008}$	$^{+0.00056}_{-0.00052}$
$14 < p_T < 16$	λ_{θ^*}	$^{+0.18}_{-0.21}$	$^{+0.13}_{-0.11}$	$^{+0.0033}_{-0.0032}$	$^{+0.22}_{-0.23}$
	λ_{ϕ^*}	$^{+0.0027}_{-0.0033}$	$^{+0.00041}_{-0.00047}$	$^{+0.000005}_{-0.000004}$	$^{+0.0027}_{-0.0033}$
	$\lambda_{\theta^*\phi^*}$	$^{+0.00017}_{-0.00016}$	$^{+0.000039}_{-0.000036}$	$^{+0.000001}_{-0.000001}$	$^{+0.00017}_{-0.00016}$
$16 < p_T < 18$	λ_{θ^*}	$^{+0.27}_{-0.28}$	$^{+0.0057}_{-0.0067}$	$^{+0.0052}_{-0.0044}$	$^{+0.27}_{-0.28}$
	λ_{ϕ^*}	$^{+0.0019}_{-0.0022}$	$^{+0.00033}_{-0.00040}$	$^{+0.000018}_{-0.000015}$	$^{+0.0020}_{-0.0022}$
	$\lambda_{\theta^*\phi^*}$	$^{+0.00089}_{-0.00059}$	$^{+0.000058}_{-0.000056}$	$^{+0.000026}_{-0.000030}$	$^{+0.00089}_{-0.00059}$
$18 < p_T < 20$	λ_{θ^*}	$^{+0.25}_{-0.26}$	$^{+0.084}_{-0.095}$	$^{+0.0068}_{-0.0054}$	$^{+0.26}_{-0.28}$
	λ_{ϕ^*}	$^{+0.0010}_{-0.0010}$	$^{+0.000016}_{-0.000064}$	$^{+0.000017}_{-0.000012}$	$^{+0.0010}_{-0.0011}$
	$\lambda_{\theta^*\phi^*}$	$^{+0.0019}_{-0.0021}$	$^{+0.00024}_{-0.00022}$	$^{+0.000005}_{-0.000006}$	$^{+0.0019}_{-0.0021}$
$20 < p_T < 25$	λ_{θ^*}	$^{+0.24}_{-0.26}$	$^{+0.11}_{-0.12}$	$^{+0.0047}_{-0.0033}$	$^{+0.26}_{-0.28}$
	λ_{ϕ^*}	$^{+0.00021}_{-0.00015}$	$^{+0.00032}_{-0.00026}$	$^{+0.000004}_{-0.000005}$	$^{+0.00038}_{-0.00030}$
	$\lambda_{\theta^*\phi^*}$	$^{+0.00044}_{-0.00050}$	$^{+0.00032}_{-0.00036}$	$^{+0.000000}_{-0.000001}$	$^{+0.00054}_{-0.00061}$
$25 < p_T < 30$	λ_{θ^*}	$^{+0.12}_{-0.14}$	$^{+0.00042}_{-0.00051}$	$^{+0.0089}_{-0.0060}$	$^{+0.13}_{-0.14}$
	λ_{ϕ^*}	$^{+0.00047}_{-0.00037}$	$^{+0.00023}_{-0.00026}$	$^{+0.000004}_{-0.000006}$	$^{+0.00052}_{-0.00045}$
	$\lambda_{\theta^*\phi^*}$	$^{+0.000050}_{-0.000078}$	$^{+0.000042}_{-0.000048}$	$^{+0.000001}_{-0.000001}$	$^{+0.000065}_{-0.000092}$
$30 < p_T < 40$	λ_{θ^*}	$^{+0.030}_{-0.034}$	$^{+0.00016}_{-0.00015}$	$^{+0.0076}_{-0.0054}$	$^{+0.031}_{-0.035}$
	λ_{ϕ^*}	$^{+0.00015}_{-0.00012}$	$^{+0.00012}_{-0.00014}$	$^{+0.000034}_{-0.000024}$	$^{+0.00020}_{-0.00019}$
	$\lambda_{\theta^*\phi^*}$	$^{+0.00038}_{-0.00035}$	$^{+0.000038}_{-0.000043}$	$^{+0.000028}_{-0.000040}$	$^{+0.00039}_{-0.00035}$
$40 < p_T < 50$	λ_{θ^*}	$^{+0.00099}_{-0.0015}$	$^{+0.00019}_{-0.00017}$	$^{+0.0019}_{-0.0029}$	$^{+0.0022}_{-0.0033}$
	λ_{ϕ^*}	$^{+0.000095}_{-0.00011}$	$^{+0.000032}_{-0.000037}$	$^{+0.000019}_{-0.000022}$	$^{+0.00010}_{-0.00012}$
	$\lambda_{\theta^*\phi^*}$	$^{+0.00030}_{-0.00026}$	$^{+0.000054}_{-0.000060}$	$^{+0.000011}_{-0.000014}$	$^{+0.00030}_{-0.00026}$
$50 < p_T < 70$	λ_{θ^*}	$^{+0.012}_{-0.011}$	$^{+0.00026}_{-0.00029}$	$^{+0.0023}_{-0.010}$	$^{+0.013}_{-0.015}$
	λ_{ϕ^*}	$^{+0.00037}_{-0.00033}$	$^{+0.000069}_{-0.000061}$	$^{+0.000016}_{-0.000099}$	$^{+0.00038}_{-0.00035}$
	$\lambda_{\theta^*\phi^*}$	$^{+0.00054}_{-0.00064}$	$^{+0.0000060}_{-0.0000042}$	$^{+0.00035}_{-0.000070}$	$^{+0.00064}_{-0.00065}$

7.6. Final results

The total uncertainties contributions are summarized in Tables 7.5 - 7.7, for each of the spin-alignment parameters. For each source, the average, minimum and maximum values are listed (averaged over all p_{T} slices).

Table 7.5.: List of the main contributions to the uncertainties of λ_{θ^*} parameter. The absolute uncertainty is reported.

systematic source	average	min.	max.	comment
Statistical error	0.031	0.0064	0.11	increases with p_{T}, due to lower stat.
Fit procedure	0.022	0.0067	0.047	within statistical error, in some slices the statistical error found to be underestimated
Prompt selection	0.021	0.0075	0.055	within statistical error, τ selection is more significant, f_{prompt} contribution is negligible
Detector resolution	-	-	-	negligible
Pileup	0.018	0.00048	0.051	within statistical error, more significant in low p_{T} slices
Trigger efficiency	0.16	0.0022	0.28	The most significant contribution, more significant at lower p_{T} slices

Figures 7.8 - 7.10 summarize the final results of the measurement of λ_{θ^*}, λ_{ϕ^*} and $\lambda_{\theta^*\phi^*}$ respectively. In black are the fit results and their statistical uncertainties, and the green bands represent both statistical and systematic uncertainties, added in quadrature.

Table 7.6.: List of the main contributions to the uncertainties of λ_{ϕ^*} parameter. The absolute uncertainty is reported.

systematic source	average	min.	max.	comment
Statistical error	0.012	0.0030	0.041	increases with p_{T}, separately for each MC sample
Fit procedure	0.0027	0.000097	0.017	within statistical error, for low p_{T} slices the statistical error is overestimated
Prompt selection	0.0096	0.00035	0.022	within statistical error, τ selections is more significant, f_{prompt} contribution is negligible
Detector resolution	-	-	-	negligible, by 2-3 orders of magnitude lower than the statistical error
Pileup	0.0019	0.00031	0.0064	within statistical error, not significant
Trigger efficiency	0.0018	0.00010	0.0080	very low, more significant at lower p_{T} slices

Table 7.7.: List of the main contributions to the uncertainties of $\lambda_{\theta^*\phi^*}$ parameter. The absolute uncertainty is reported.

systematic source	average	min.	max.	comment
Statistical error	0.016	0.0086	0.042	increases with p_{T}, separately for each MC sample
Fit procedure	0.00088	0.0001	0.0071	negligible with compare to the statistical error, for low p_{T} slices the statistical error is overestimated
Prompt selection	0.0051	0.0015	0.014	within statistical error, τ selections is more significant, f_{prompt} contribution is negligible
Detector resolution	-	-	-	negligible, by 2-3 orders of magnitude lower than the statistical error
Pileup	0.0033	0.00056	0.0080	within statistical error, not significant
Trigger efficiency	0.00073	0.000065	0.0021	negligible

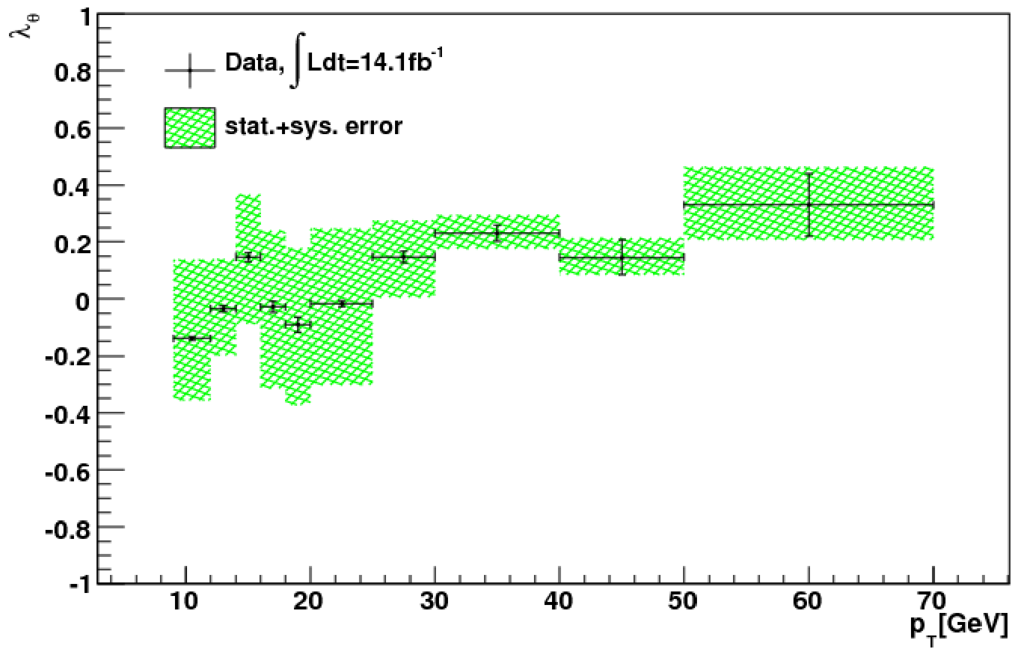

Figure 7.8.: Final fit results for λ_{θ^*} with respect to the J/ψ p_{T}. Black points represent fit result and their statistical uncertainties, and green bands represent the total uncertainties.

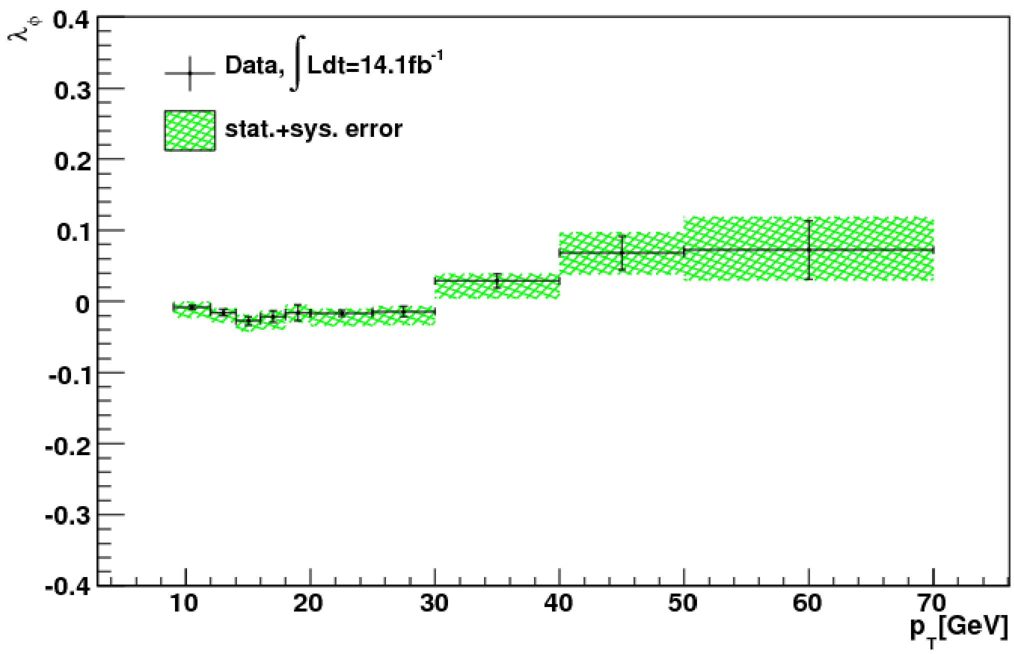

Figure 7.9.: Final fit results for λ_{ϕ^*} with respect to the J/ψ p_{T}. Black points represent fit result and their statistical uncertainties, and green bands represent the total uncertainties.

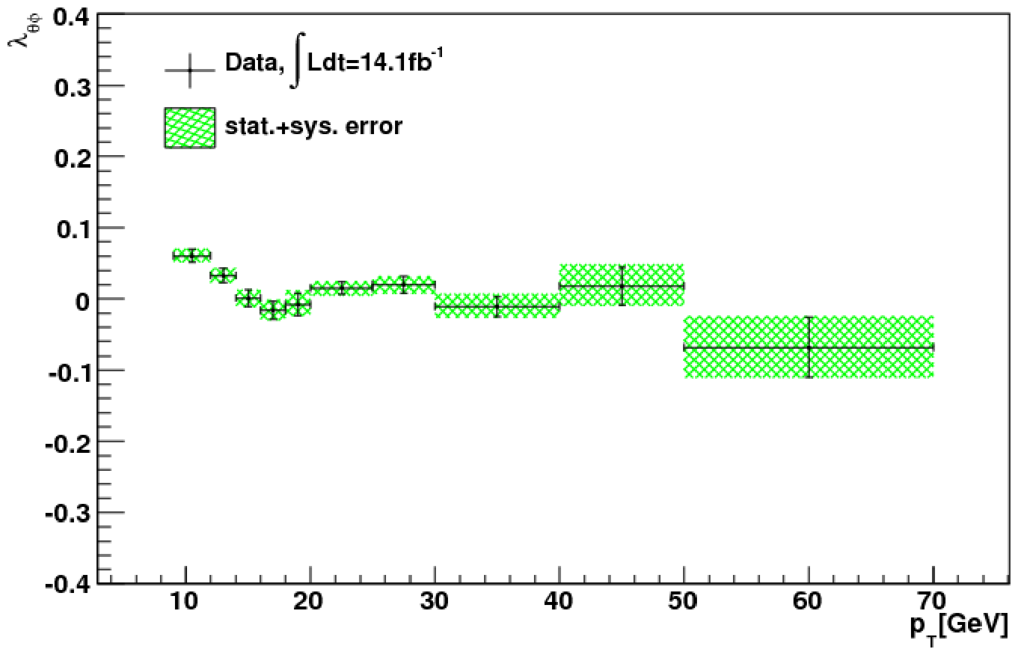

Figure 7.10.: Final fit results for $\lambda_{\theta^*\phi^*}$ with respect to the J/ψ p_T. Black points represent fit result and their statistical uncertainties, and green bands represent the total uncertainties.

Chapter 8.

Summary

This thesis presents the first measurement of prompt J/ψ spin-alignment done in proton proton collision at a center of mass energy of 8 TeV. The analysis is preformed on the data collected by the ATLAS experiment in 2012, with a total luminosity of 14.1 fb^{-1}. The measurement was preformed on prompt J/ψs decaying into $\mu^+\mu^-$.

In order to measure the spin-alignment of a pure prompt J/ψ sample, without other sources of background and non-prompt J/ψs (coming from B-decays), a complementary analysis had to be made. For this purpose a measurement of the production ratio of prompt to non-prompt J/ψ was done. This measurement is a direct continuation of the measurement preformed on the 7 TeV data that was published based on the early data taking of 2010 [10], and on ongoing measurement that is about to be published based on a 7 TeV data that was collected during 2011.

The results of this analysis showed consistency with previous measurements. From this analysis the fraction of each type of data is extracted, as mentioned above in the signal region. An analysis based on a division on dedicated control regions results in a high purity signal region of prompt J/ψ sample. As shown in the previous chapters, this part is crucial, since every source may have totally different angular behaviour. Without this step one would have measured an average spin-alignment of all three sources. The measurement was performed separately in different transverse momentum regions, showing the spin-alignment p_{T} dependence.

On the high purity prompt J/ψ sample, a measurement of the spin-alignment was made in the helicity frame, for a rapidity region between 0.2 to 0.8, and in p_{T} spectrum between 9 to 70 GeV. This rapidity region was selected in order to reduce possible biases due to very low efficiency regions around the $|\eta| \approx 0$.

For measuring the J/ψ spin-alignment template χ^2 fit was used. The templates were formed combining two unpolarized MC samples. One sample was generated using muons with p_{T} above 4 GeV, and the other sample using muons with p_{T} above of 6.5 GeV. Each sample was used in different p_{T} region, where the lower threshold sample was used in the region of J/ψ p_{T} up to 20 GeV, and the second sample was used from 20 GeV up to 70 GeV.

The MC samples were re-weighted to compensate for the data-MC discrepancies in acceptance, efficiency, luminosity, resolution and pileup effects.

The outcome of this analysis is a measurement of the three spin-alignment parameters and their p_{T} dependence. The λ_{ϕ^*} and $\lambda_{\theta^*\phi^*}$ found to be very small throughout the whole p_{T} region. The λ_{ϕ^*} tends to small negative values at low p_{T}, and small positive at the higher p_{T} region. $\lambda_{\theta^*\phi^*}$ is consistent with zero in most of the p_{T} slices. The λ_{θ^*} tends to negative values in the lower p_{T} regions and positive values in the higher p_{T} regions. Overall the statistical error increases with p_{T}, this is due to the lower statistics in the data sample with the increase of p_{T}.

A careful study of systematic uncertainties was performed. It was found that for the λ_{ϕ^*} and $\lambda_{\theta^*\phi^*}$ the different systematics sources are very low, and are within the statistical errors. For the λ_{θ^*}, most of the systematic sources are negligible, except for the systematic uncertainty due to the trigger efficiency maps. This systematic is the dominant source of uncertainty mainly in the low p_{T} region. When considering the total uncertainty, one can say that the λ_{θ^*} is consistent with zero for the low J/ψ p_{T} region and it increases to positive values (around 0.2) in the higher p_{T} region. Namely assuming $\lambda_{\phi^*} \approx \lambda_{\theta^*\phi^*} \approx 0$, one can conclude that the measured λ_{θ^*} can be interpreted as a direct measurement of the J/ψ polarization, which was found to be slightly transversely aligned above p_{T} of 20 GeV.

These results are consistent with the latest CMS results preformed on the 7 TeV data [28]. The NLO NRQCD predict polarization of ~ 0.2 from low J/ψ p_{T} with slight increase in the higher p_{T} region [29]. The present results tend to disagree with the NLO NRQCD prediction at the low p_{T} region, although one can not exclude the NLO NRQCD due to the high systematic uncertainties in this region.

In order to improve the measurement and reduce the total uncertainties, one needs larger MC sample with low p_{T} threshold. This will reduce both the statistical and systematic uncertainties. One will gain more statistics in the higher p_{T} slices (due to the lower muon p_{T} threshold) in the data sample, which dominates the statistical error, and improve the templates in the lower p_{T} region, which control the systematic uncertainties.

Chapter 9.

Small Thin Gap Chambers

The luminosity levels foreseen for the LHC after the 2018 LHC upgrade will tighten the demands on the ATLAS first level muon trigger system. A finer muon selection will be required to cope with the increased background and to keep the trigger rate for 20 GeV/c p_{T} muons as before. Some of the present Muon Spectrometer components will fail to cope with these high rates and will have to be replaced. In particular, the expected rate of neutrons with energies above 100 keV may exceed $10^5 Hz/cm^2$. A small Thin Gap Chamber (sTGC) was develop and proposed to replace the small wheel of the ATLAS detector. This proposal was accepted by the collaboration this year and the Technical Design Report was released on July 2013 [30].

This chapter briefly describes my work on the sTGC project. This work was an effort of three Israeli Institute, Tel-Aviv University, Weizmann Institute and the Technion-Israel Institute. Under my responsibilities were the design and implementation of the data acquisition, the online monitoring and various physics analysis for the different tests that are described in the following sections. The work described here was publish in 2011 and 2013 [31, 32]

9.1. Introduction

The ATLAS experiment [17] was designed for a broad physics programme, including precision measurements of the Standard Model (SM) and search for the Higgs boson, SUSY or Exotics new particles accessible at the Large Hadron Collider (LHC). Once such particles are discovered, their properties have to be studied as is currently the case with Higgs boson discovered by the ATLAS and the CMS collaboration during 2012. These studies require very large data samples. For that reason, upgrades are needed of both the LHC (to increase the luminosity) and of the ATLAS experiment (to be able to cope with higher collision rates and radiation background). The large integrated luminosity eventually available will also provide access to rare processes and to higher centre-of-mass energies of colliding partons, extending the reach of the searches for heavy new particles.

The LHC complex will be upgraded in several phases. Following the long shutdown of 2013/14 (LS1), the accelerator energy will be increased to close to 7 TeV per beam, and the luminosity will reach or exceed the nominal value of $1 \cdot 10^{34}\,\mathrm{cm}^{-2}\mathrm{s}^{-1}$. Major upgrades are planned starting from the 2018 shutdown with which the LHC luminosity will substantially exceed the initial design values. At the second long shutdown in 2018 (LS2), the accelerator luminosity will be increased to 2 to $3 \cdot 10^{34}\,\mathrm{cm}^{-2}\mathrm{s}^{-1}$, allowing the ATLAS experiment to collect $\sim 100\ \mathrm{fb}^{-1}$/year. The last upgrade will introduce significant changes to the interaction point (IP) region so that the luminosity will reach up to $7 \cdot 10^{34}\,\mathrm{cm}^{-2}\mathrm{s}^{-1}$ ($5 \cdot 10^{34}\,\mathrm{cm}^{-2}\mathrm{s}^{-1}$ with luminosity leveling) aiming to an integrated luminosity of $3000\ fb^{-1}$ in approximately 10 years of operation after that upgrade. Figure 9.1 shows an approximate timeline for the planned LHC and ATLAS upgrades. The ATLAS detector will also be upgraded following the same time schedule as the LHC upgrades.

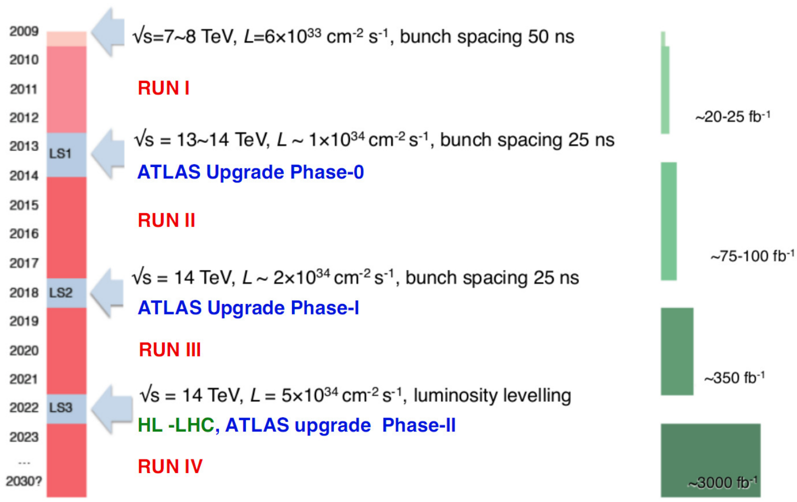

Figure 9.1.: An approximate timeline of the scheduled LHC and ATLAS upgrades.

A major goal of the Phase-I upgrade [33](2018) is improving the Level-1 trigger in order to maintain the low transverse momentum (p_T) threshold for single leptons (e and μ) while keeping the Level-1 rate at a manageable level. Upgrades are planned for both the muon and the calorimeter trigger systems, without which the single lepton triggers would have to be either pre-scaled or its p_T threshold raised, resulting in a significant loss of acceptance for many physics processes of interest.

9.2. Upgrade of the Muon Spectrometer: New Small Wheels

The Phase-I upgrade of the ATLAS muon spectrometer [34] focuses on the end-cap region. Figure 9.2 shows a cut-out of the ATLAS detector in z-y plane. The barrel and end-cap system consist of three stations each, measuring the muon momentum based on the curvature in the ATLAS toroid magnets.

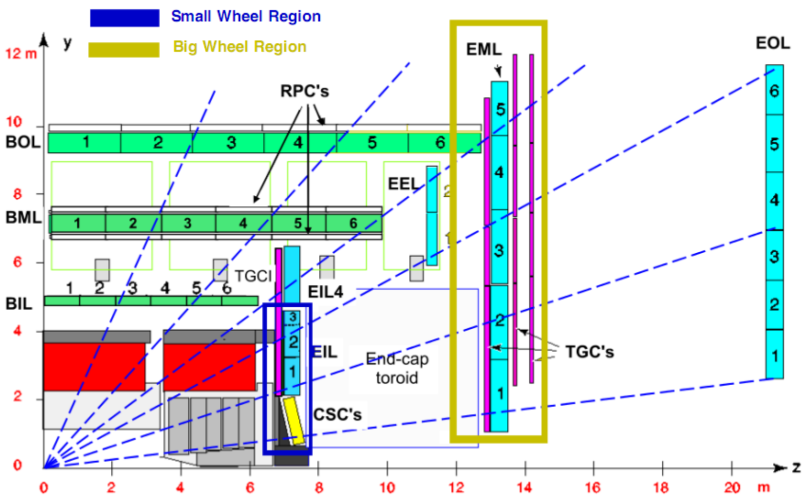

Figure 9.2.: A z-y view of 1/4 of the ATLAS detector. The blue boxes indicate the end-cap Monitored Drift Tubes (MDT) chambers and the yellow box Cathode Strip Chambers (CSC). The green boxes are barrel MDT chambers. The trigger chambers, Resistive Plate Chambers (RPC) and Thin Gap Chamber (TGC), are indicated by the grey and the magenta boxes. This is a cut-out on the muon spectrometer at the large sectors, hence the names 'End-cap Inner Large', 'End-cap Middle Large' (EML) and 'End-cap Outer Large'.

At high luminosity the following two points are of particular importance:

- The performance of the muon tracking chambers (in particular in the end-cap region) degrades with the expected increase of cavern background rate [33]. An extrapolation from the observed rates at the lower luminosity conditions of the 2012 to high luminosity conditions indicates a substantial degradation of tracking performance, both in terms of efficiency and resolution in the the inner end-cap station (at z=7 m), the 'Small Wheels'. Given that high resolution muon momentum measurement is based on the presence of measuring points at the Small Wheel level (i.e. in front of the end-cap toroid magnet), this degradation is detrimental for the performance of the ATLAS detector.

- The Level-1 muon trigger in the end-cap region is based on the track segments in the TGC chambers of the middle muon station (End-cap Muon detector, EM) located after the end-cap toroidal magnet [17]. (The TGC of the Small Wheel is only used as a rough confirmation that a particle has traversed the end-cap toroid zone. It cannot provide a precise muon trigger as, being a doublet plane, it cannot reconstruct a track segment.) The transverse momentum p_T of the muon is determined by the angle of the segment with respect to the direction pointing to the interaction point. A significant part of the muon trigger rate in the end-caps are fake muons. Low energy particles generated far from the IP and out of time of the triggered bunch crossing, produce fake triggers by hitting the end-cap trigger chambers at an angle similar to that of real high p_T muons. An analysis of 2012 data demonstrates that $\sim$ 90% of the muon triggers in the end-caps are fake. As a consequence the rate of Level-1 muon trigger in end-cap is 8 to 9 times higher than that in the barrel region.

Both of these two issues represent serious limitation on the ATLAS performance at high luminosity: reduced acceptance of good muon tracking, and loss of low p_T single muon Level-1 triggers.

In order to address the two problems, ATLAS proposes to replace the present muon Small Wheels with the 'New Small Wheels' (NSW). The NSW is a set of precision tracking and trigger detectors able to work at high rates with excellent real-time space and time resolution. These detectors can provide the muon Level-1 trigger system with online track segments of good angular resolution to confirm that muon tracks originate from the IP. In this way the end-cap fake triggers will be considerably reduced.

9.3. Impact on physics performance

The importance of having a high efficiency Level-1 trigger for inclusive leptons with $p_T <$ $20 \sim 25\,\mathrm{GeV}$ has been shown in the Higgs boson searches through the WW$^* \to \ell\nu\ell\nu$ decay in the low Higgs mass range. This situation will become even more crucial for the high luminosity running of the LHC. Given the recent discovery of the Higgs boson, this is particularly true. Large integrated luminosity (a few 100 fb^{-1}) will allow the precise determination of its couplings to gauge bosons and fermions using production processes independent of the decay mode, such as Higgsstrahlung from W ($pp \to WH$), where triggering on the W by leptons of $p_T \sim 20\,\mathrm{GeV}$ is needed to investigate the Higgs decays into WW, b$\bar{\mathrm{b}}$ and $\tau^+\tau^-$ final states. Table 9.1 shows a comparison of efficiency and Level-1 rate from a simulation study for the

Table 9.1.: Expected Level-1 rate at $3 \times 10^{34}\,\mathrm{cm}^{-2}\,\mathrm{s}^{-1}$ for different p_T threshold with and without NSW. Columns 3–4 show the efficiency for WH associate production $pp \to WH$ with two decay modes of the SM Higgs boson of the mass 125 GeV into $H \to b\bar{b}$ and $H \to W^+W^- \to \mu\nu qq'$.

L1MU threshold (GeV)	Level-1 rate (kHz)	$H \to b\bar{b}$ (%)	$H \to W^+W^-$ (%)
$p_T > 20$	60	82	89
$p_T > 40$	29	50	64
$p_T > 20$ with NSW	22	78	86

present detector and the upgrade with NSW. At the instantaneous luminosity $3 \times 10^{34}\,\mathrm{cm}^{-2}\mathrm{s}^{-1}$, the single muon Level-1 rate of the present system will become as high as 60 kHz, dominating the allowed total Level-1 rate of 100 kHz. The Level-1 rate may be reduced significantly by raising the p_T threshold to 40 GeV, but with the high cost of reduced efficiency to the WH production channels. The NSW will allow ATLAS to keep the Level-1 rate, for single muons above 20 GeV, at 22 kHz with very limited loss of efficiency. The same argument applies also to the ZH associated production.

Low p_T lepton triggers are also important for many SUSY searches where leptons are produced through cascade decays. The kinematic distribution of the final state objects depends on the mass relation between particles in the cascade as well as the couplings. Any increases in the lepton trigger threshold (and other objects like jets and E_T^{miss}) lead to a reduction of experimental sensitivity in the parameter space of SUSY models [33]. Efficiency is generally lower with higher p_T threshold, and it is particularly true for the parameter space of small mass difference. Similar situations are found in other SUSY processes such as the searches for sleptons and electroweak gauginos.

9.4. Muon small wheel detector requirements for run III

The highest counting rates in the muon spectrometer is observed in the Small Wheel region. A large fraction of that is due to low energy photons and neutrons. They are generated by synchronous proton collisions with the bunch crossing that triggers the ATLAS data-taking mechanism (in-time background), or by collisions that happen one to several bunch crossings earlier (out-of-time background). This background radiation originates from the whole ATLAS detector volume, and hence escapes capture by the radiation shielding around the beam pipe and the ATLAS calorimeters. The resulting particles are generically referred to as cavern background.

9.4.1. Operating conditions for run III

In order to predict reliably the expected cavern background rates after the various accelerator upgrades, two elements are required: an accurate measurement of the observed background at the current operational conditions and a reliable Monte-Carlo extrapolation to higher energy and luminosity. Figure 9.3 shows the ratio of the measured hit rates to the corresponding simulation values for the existing muon Monitored Drift Tubes (MDT) chambers. This ratio is in general between 0.5 and 1.4. As a consequence this current background simulation can be reliably used to predict counting rates in the muon system for different detector geometries and beam energies.

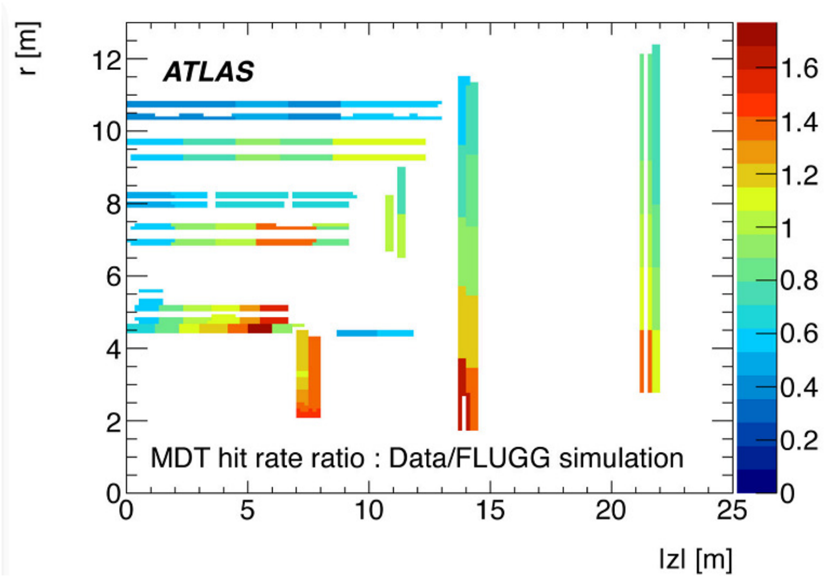

Figure 9.3.: Ratio of measured to simulated MDT hit rate during a 7 TeV run at an average luminosity of $1.9 \times 10^{33}\,\mathrm{cm}^{-2}\mathrm{s}^{-1}$ (50 ns bunch spacing) [35].

The background level is a steep function of the distance from the beam line, being highest for the detectors closer to the beam pipe. Direct hit rate measurements using the muon detector have been performed at the current luminosities to study this dependency. Figure 9.4 (a) shows the measurements in the Small Wheel region for MDT and CSCs (Cathode Strip Chambers), used, instead of MDT, in the inner part of the present end-cap Small Wheel (since they can cope better with high radiation environments). The discontinuity at R=210 cm is caused by the different sensitivity of MDT and CSC to cavern background particles. The expectation by FLUGG [36] simulation is also shown in the same figure. The measured radial dependence reasonably agrees with Monte-Carlo predictions. The measured results are then used to estimate the background rate on the Small Wheel as a function of radial distance from the beams, assuming that the same technology is used over the full acceptance of the Small Wheel. In Fig. 9.4 (b) the observed rates in MDT (R>210 cm) and CSC (R<200 cm) are scaled to the values corresponding to the nominal luminosity of $1 \times 10^{34}\,\mathrm{cm}^{-2}\mathrm{s}^{-1}$. In addition the CSC curve is scaled to have the same value as the MDTs one at their boundary to simulate the condition of an all MDT-type detector scenario. Similarly, the MDT curve is scaled to simulate the all CSC-type detector case. The difference between these two curves indicates a possible dependency of the background hit rate on the detector technology. Figure 9.4 (b) indicates that at a luminosity of $1 \times 10^{34}\,\mathrm{cm}^{-2}\mathrm{s}^{-1}$ the current MDT system will operate near its limits, and well beyond that for a luminosity of $7 \times 10^{34}\,\mathrm{cm}^{-2}\mathrm{s}^{-1}$.

The expected hit rate at the maximum Phase-II luminosity of $7 \times 10^{34}\,\mathrm{cm}^{-2}\mathrm{s}^{-1}$ will be $\sim 14\,\mathrm{kHz/cm}^2$ assuming conservatively the MDT sensitivity for the future detector. The extrapolation to high luminosities is simple as the rate of cavern background is proportional to the beam luminosity. This has been established experimentally by studying hit rates and currents in several muon detectors at LHC runs of various luminosities. All the above is based on the measurements at $\sqrt{s}$=7 TeV. The ratio of background rate at $\sqrt{s}$=14 TeV and 7 TeV is about 1.3 in the Small Wheel region according to the Monte Carlo simulation using FLUGG.

Any new detector that might be installed in the place of the current Small Wheel should be operational for the full life time of ATLAS (and be able to integrate 3000 fb^{-1}). Assuming 10 years of operation and the above expected hit rate per second, approximately $10^{12}\mathrm{hits/cm}^2$ are expected in total in the hottest region of the detector [37].

The proposed detectors should be validated for ageing effects at a level of $\sim 1\, Coulomb/cm^2$ (or higher) for a planar detector or the equivalent for a wire chamber, and in case the required performance is difficult to achieve, the possibility of replacing chambers, especially in the very forward region, should be envisaged. The trigger and read-out electronics should also be validated in the same conditions.

9.4.2. Physics performance and precision tracking

It has been shown that the current muon detectors in the NSW region cannot operate efficiently in the high background environment expected with the various LHC upgrades. A new detector needs to be built which will give high detection and reconstruction efficiency, even at the

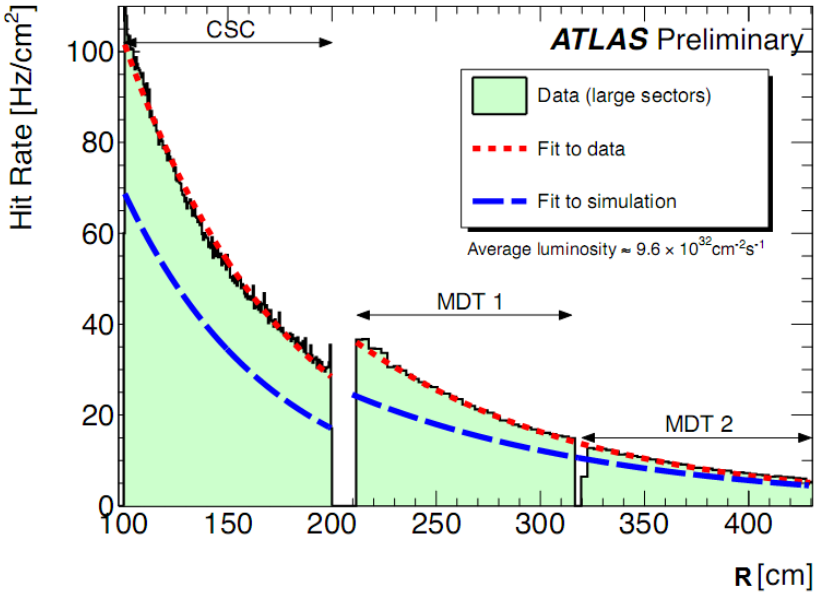

(a) $\mathcal{L} = 9.6 \times 10^{32}\,\mathrm{cm}^{-2}\mathrm{s}^{-1}$, $\sqrt{s}$=7 TeV.

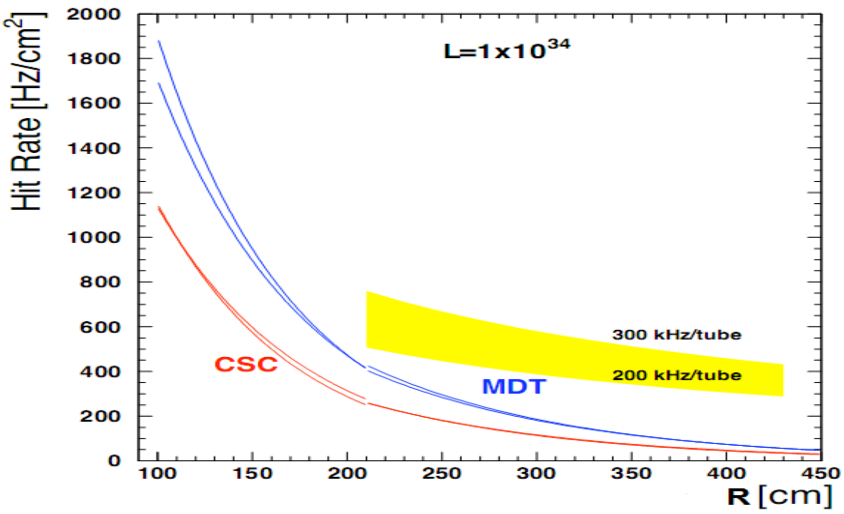

(b) Scaled to $\mathcal{L} = 1 \times 10^{34}\,\mathrm{cm}^{-2}\mathrm{s}^{-1}$, $\sqrt{s}$=7 TeV.

Figure 9.4.: Measured Cavern background at the level of the muon Small Wheel. Figure (a) shows measurements and a simulation estimation of the background. Given the small discrepancy between measurements and simulation the measured values have been used for subsequent extrapolation to higher luminosities. Figure (b) shows an extrapolation to a luminosity of $\mathcal{L} = 1 \times 10^{34}\,\mathrm{cm}^{-2}\mathrm{s}^{-1}$, $\sqrt{s}$=7 TeV. [35]

highest particle fluxes expected. The performance of the new detector at high luminosity should be at least as good as that of the current detector at low luminosity, and be able to measure the transverse momentum (p_T) of passing muons with a precision of 10% for 1 TeV muons in the full pseudorapidity coverage of the Small Wheel (up to $\eta = 2.7$). In particular such a detector should have the following characteristics:

- Measure hits with a position resolution in the bending plane of $< 100\,\mu$m per measurement;
- Angular resolution of ~ 0.3 mrad;
- Segment finding efficiency of more than 97% for muons with p_T more than 10 GeV (the segment finding efficiency for the current MDT system), and track segment resolution of less than 50μm including all alignment and calibration errors;
- Efficiency and resolutions should not degrade at very high momenta (due to δ rays, showers etc);
- Measure the second coordinate with a resolution of 1–2mm.

9.4.3. Trigger selection power

Trigger simulations show that for selecting muons with $p_T > 20$ at Level-1 (L1MU20) one would get a trigger rate at $\sqrt{s}$=14 TeV and at an instantaneous luminosity of $3 \times 10^{34}\mathrm{cm}^{-2}\mathrm{s}^{-1}$ of approximately 60 kHz, to be compared to the total allowed Level-1 rate of 100 kHz. Due to the limited p_T resolution of the Level-1 muon trigger system, raising the threshold above 20 GeV does not further improve significantly the signal to noise ratio.

In order to reduce the low p_T components, the p_T resolution of the muon Level-1 system needs to improve significantly. A precision angle measurement at the Small Wheel level can be used to improve the p_T resolution of the Level-1 trigger in the end-cap. In the present layout, the contributing factors to the p_T resolution are: i) angular resolution of the current Big Wheel trigger station (~ 3 mrad), ii) multiple scattering in the end-cap toroid (~ 0.5 mrad for high p_T muons), iii) multiple scattering in the calorimeters (~ 2 to 3 mrad for low energy muons and considerably less than 1 mrad for high energy ones), and iv) finite size of luminous region of p-p collision (corresponds to 1–2 mrad depending on η). A precision angle measurement by the Small Wheel can be used to eliminate the contributions iii) and iv) by correcting for these effects track by track, thus removing part of the smearing effects to improve the p_T resolution. To be compatible with the performance of the Big Wheel, a resolution of 3 mrad or better is required for the determination of the track segment angle (angle relative to the pointing direction to the IP) at the level of the Small Wheel. However the ATLAS Phase-II upgrade will probably improve part of the Big Wheel trigger resolution to 1 mrad. Hence a similar resolution of 1 mrad is required at the level of the Small Wheel for a detector that will have to perform adequately for the whole lifetime of the ATLAS experiment.

9.5. System overview

The NSW system consists of sTGC and micro megas (MM) detectors. Figure 9.2 shows the location of the NSW with respect to the Big Wheel, and the end-cap toroid magnets. Each technology is composed of eight detection layers. There are two sTGC quadruplets in the outer layers and inside are two MM layers. Although both technologies can provide both trigger and precision measurements, the sTGC is the primary trigger and the MM are mainly used for precision measurement. The NSW trigger system provides candidate muon tracks to the TGC Sector Logic which uses them to corroborate trigger candidates from the Big Wheel TGC chambers. The Sector Logic then sends Level-1 trigger candidates to the ATLAS Muon Central Trigger logic. The radial coordinate of tracks found in the NSW is measured by high precision strips. The azimuthal, ϕ coordinate is determined by the triggering tower of NSW pads for sTGC and by small angle stereo strips for the MM. A line from the interaction point through the R-ϕ point of a track in the NSW is projected onto the Big Wheel's R-ϕ array of Regions-of-Interest (RoI). Tracks within a ± 7.5 mrad angle of this line are passed to the Sector Logic which attempts to match it to an active RoI in the Big Wheel. Confirmed hits become Level-1 candidates sent to the Muon Central Trigger Interface.

In addition to a precision track coordinate for projection to the Big Wheel, the NSW trigger measures the polar angle of the track inside the Small Wheel, i.e. before the end-cap toroid, to an accuracy of <1 mrad. This is done by calculating the track position in two virtual planes within the Small Wheel. For the sTGC these are located on either side of the MM chambers separated by about 30 cm (See Fig. 9.2.). For MM the separation is less, resulting in poorer pointing resolution. For sTGC, each of these two radial coordinates is calculated by averaging up to four centroids of strip signals from four sTGC detectors. The centroids are calculated by the sum of strip position weighted by charges. Finally, the radial position and angle θ, between a track in the NSW and an infinite momentum track from the interaction point, are calculated from these two coordinates. The azimuthal coordinate, ϕ, is defined by the pad tower that triggered the sTGC trigger. For the MM one takes advantage of the 0.5 mm strip pitch and use the strip address of the earliest arriving hit in a given bunch crossing to obtain the radial coordinate with sufficient resolution in each plane in order to calculate the polar angle. The ϕ coordinate is obtained by a lookup table addressed by the strip addresses of two small angle stereo views. A stereo angle of just 3° is sufficient to determine the ϕ coordinate with the required precision. The angle θ is passed to the Sector Logic, but will not be used until Phase-II when the New Big Wheel trigger will provide an angle of similar accuracy; the two angles can then be used to calculate a much more accurate p_{T} for the Level-1 trigger than the current one. For Phase-I the improved p_{T} can be calculated by Level-2 using MDT data.

The sTGC NSW trigger logic uses pad tower triggers to drastically reduce the amount of sTGC data to be processed on each bunch crossing for the Level-1 trigger. Three-out-of-four coincidences are made in pad towers in each sTGC quadruplet; these are then combined to choose a band of strips in each of the eight sTGC layers to be readout to the trigger processors in USA15[1]. The details are described in [30].

There are no plans to use the wires in the sTGC trigger, but they are read out in response to a Level-1 ”Accept signal” and are therefore available to the Level-2 trigger. Only the outer two detectors of each layer have wire readout. For the inner two, the pad segmentation provides a fine enough ϕ coordinate.

9.6. sTGC detector technology

The basic Small strip Thin Gap Chamber (sTGC) structure is shown in Fig. 9.5[a]. It consists of a grid of 50 µm gold plated tungsten wires with a 1.8 mm pitch, sandwiched between two cathode planes at a distance of 1.4 mm from the wire plane. The cathode planes are made of a graphite-epoxy mixture with a typical surface resistivity of 100 kΩ/□ sprayed on a 100 µm thick G-10 plane, behind which there are on one side strips (that run perpendicular to the wires) and on the other pads (covering large rectangular surfaces), on a 1.6 mm thick PCB with the shielding ground on the opposite side (see Fig. 9.5[b]). The strips have a 3.2 mm pitch, much smaller than the strip pitch of the ATLAS TGC, hence the name ’Small TGC’ for this technology.

A similar type of structure was used in the past for the OPAL Pole-Tip calorimeter, where 400 detectors were constructed and run for 12 years.

9.7. Results from different tests

Several large Prototypes, that can be assembled into a full size detector, 1.2×0.8 m^2 each, were constructed. Each prototype includes four layers of TGCs (their layout is shown schematically in Fig. 9.5[a].) and fit within a total thickness of 50 mm. Each layer contains a series of

[1]The USA15 cavern next to the ATLAS experimental cavern hosts most of the electronics in the experiment and it is accessible during the runs of the LHC.

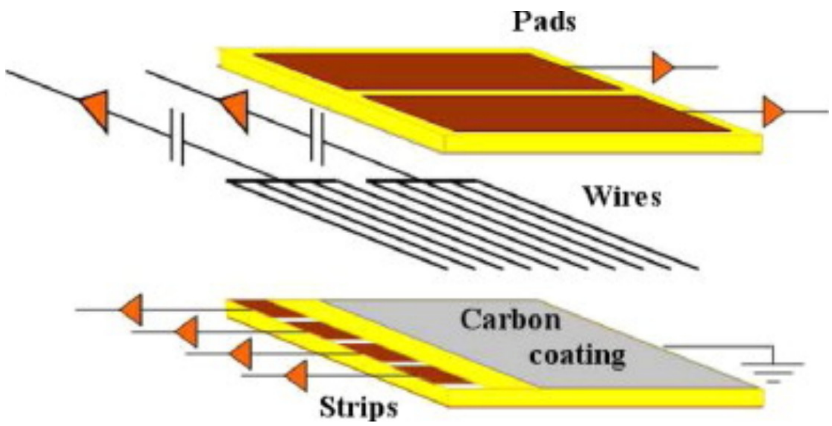

(a)

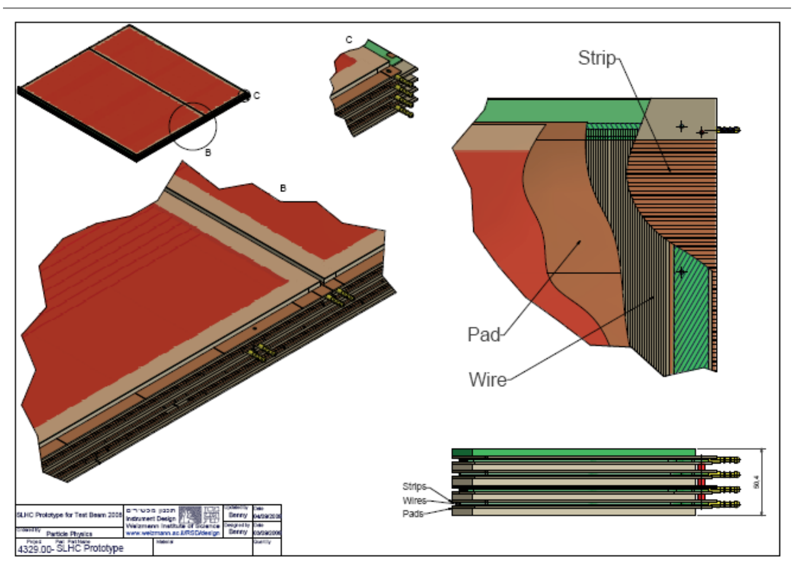

(b)

Figure 9.5.: The sTGC internal structure: (a) basic sTGC single layer structure. (b) schematic view of the sTGC quadruplet.

Large prototype parameters	
Strip-carbon gap	0.1 mm
Strip pitch	3.2 mm
Inter-strip gap	0.3 mm
Wire length in 4 layers	0.4, 0.5, 0.6, 0.7 m
Number of wires ganged together	5 (9 mm granularity)
Strip length	1.2 m
Pad size	40×10 cm^2
Carbon surface resistivity	50 kΩ/square
HV blocking capacitance	470 pF
Readout electronics parameters	
Preamplifier gain	0.8V/pC
Integration time	16 ns
Main amplifier gain	7
Equivalent noise charge	7500 electrons at CD=150 pF

Table 9.2.: *Large prototype parameters.*

pads for local trigger coincidence and strips, perpendicular to the wires, for high precision position measurement as well as local precision trigger elements. The wires are used for second coordinate measurement. The large Prototype parameters are shown in table 9.2.

9.7.1. Position resolution test beam at CERN

The position resolution of one of the large prototypes was measured using 100 GeV muons from the SPS-H8 test beam at CERN in June 2009. Previous CERN pion test beam result with smaller prototypes are described in [38]. The main goal of the test was to determine the position resolution in each of the layers using analog and fast readout, as well as its dependence on the muon incidence angle. Each detector was equipped with 16 strip analog and digital readout channels of similar type as those used in the ATLAS TGC [39].

The external trigger was provided by a coincidence of two plastic scintillators. The position resolution is directly related to the profile of induced charge on the strips and the accuracy of charge measurement. The actual charge on each of the strips was measured using two 32-channels, 12-bit resolution charge integrating ADC modules CAEN V792. The four ADC count distributions for a typical event is shown in Fig. 9.6. The four track positions Pos_1, Pos_2, Pos_3 and Pos_4 were determined by a Gaussian fit. For each detector the extrapolation of the other three detectors positions was used in order to find the expected position of the fourth detector hit position: Exp. Then the difference between the measured Pos_i and the expected Exp_i positions have provided the residual.

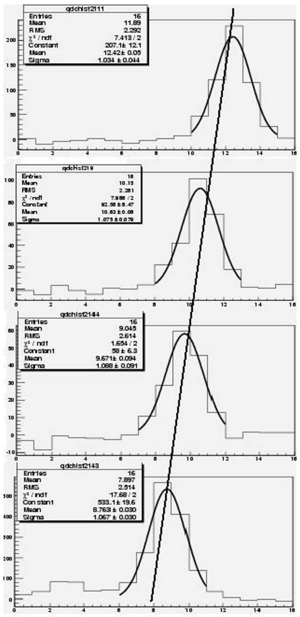

Figure 9.6.: *Typical TGC quadruplet event as seen in the ADC counts histograms.*

Due to the periodic strip structure, the deviation of the expected hit position from the measured one depends on the hit position. This dependence is clearly seen in Fig. 9.7. A sinusoidal fit was applied to correct for this differential non-linearity effect. The final deviation was calculated from the fit curve. The residual distribution for each of the four detectors vs. hit position after this correction is shown in Fig. 9.8. The width of this distribution, $\sigma_{residual}$, is defined as the local resolution for each detector.

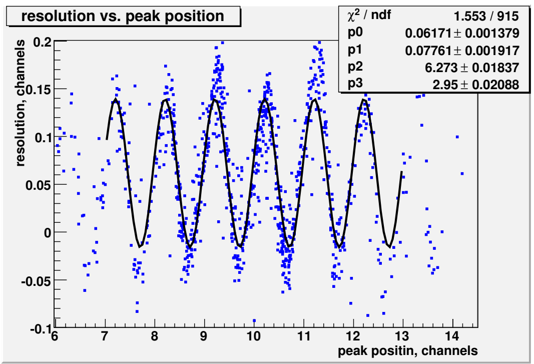

Figure 9.7.: *Residual vs. hit position with sinusoidal fit.*

The resolution is also affected by the incidence angle ϕ, since this angle determines the track projection on the anode wire, as explained in [38]. The angular dependence of the resolution was studied by rotating the chambers with respect to the beam axis. A set of measurements with different anode high voltage (HV) values were performed for incidence angles of: 0, 5, 10,

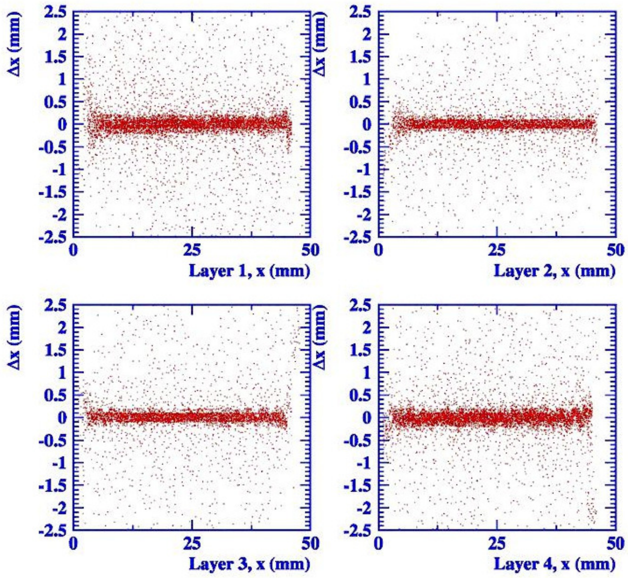

Figure 9.8.: *Residual vs. hit position for the four TGC prototypes after differential non-linearity correction.*

20 degrees. Three HV values were used: 2.9, 3.0 and 3.1 kV. The local spatial resolution vs. incidence angle for different HV values is shown in Fig. 9.9(a). One can see that the resolution deteriorates as the angle increases and improves with higher HV. Single gap resolution of better than 100 μm is achieved for incidence angles of up to 20^0 and HV value of 3.0 kV. These values of resolution meet the sLHC requirements.

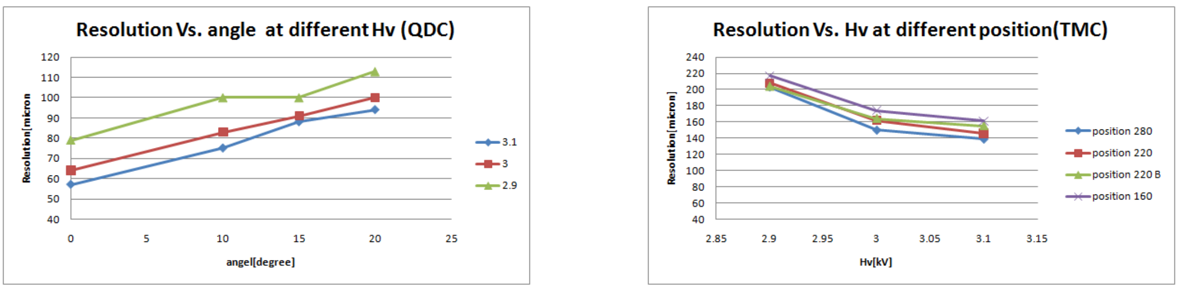

(a) (b)

Figure 9.9.: (a)Local resolution vs. incidence angle for different HV values. (b) Digital resolution vs. HV for four different geometrical TGC positions at zero incidence angle.

In order to confirm the suitability of the TGC as a trigger device, the spatial resolution of the TGC with digital signals from the strips using the time over threshold information for each channel was also measured. The time was measured with a VME 32CH TMC TEG3 KEK module. Determination of the hit position and the resolution measuring were done in the same way as for the analog readout. The obtained digital resolution values vs. HV for four different geometrical TGC positions (in order to avoid the geometrical systematic) at perpendicular incidence are shown in Fig. 9.9(b). At 3 kV the average digital resolution is 160 μm which easily meets the level one trigger angular resolution requirement of 1 mrad for a 200 mm thick detector.

9.7.2. Neutron beam test at Demokritos

Muon detecting capabilities of the TGC were also studied when the detector was exposed to a high flux of neutrons. The test was carried out at Demokritos, Greece in October 2009. The facility at Demokritos consists of MV TANDEM T11/25 accelerator, which uses Van de Graff electrostatic technique with high voltages between 0.4 and 5.5 MeV. The detailed description of the Demokritos facility can be found in [40]. Neutron flux measurement was performed via the ^{191}Ir(n,2n)^{190}Ir activation reaction [41]. Schematic view of the experimental setup is shown in Fig. 9.10. The trigger for cosmic ray muons was provided by a triple coincidence of the so called TGC monitor detectors shown in the figure. The same type of front-end and readout electronics as in the CERN test was used. The procedure to determine efficiency and resolution was identical to the one described in the previous section, by fitting a track over three TGC layers and deriving the predicted position on the fourth. The hit was considered good if the measured position was in the range of 10 mm from the predicted one. Muon detection efficiencies vs. neutron rates are shown in Fig. 9.11. The efficiency deterioration at high rate is not significant. Although there was a concern that neutrons may give rise to large signals, producing HV breakdown (sparks), no such sparks were observed during the five days period of the test.

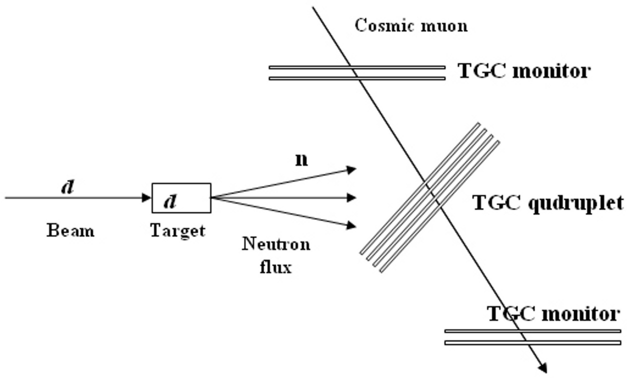

Figure 9.10.: *Experimental setup at Demokritos.*

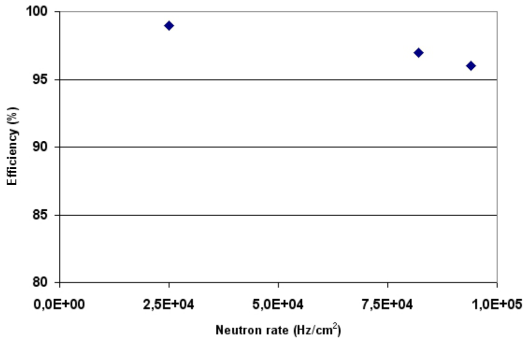

Figure 9.11.: *Muon detection efficiency vs. detected neutron rate.*

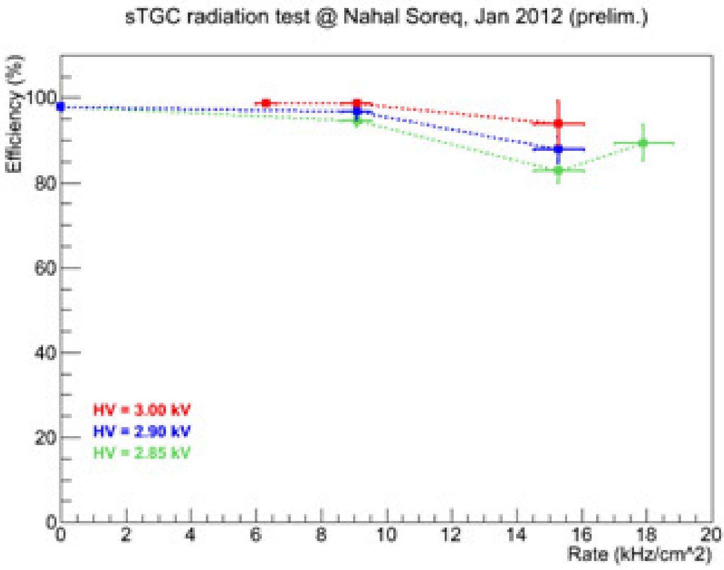

Figure 9.12.: Single layer efficiency for detecting minimum ionizing particles as function of the detected photon rate of a $120 \times 70\,\mathrm{cm}^2$ chamber irradiated at the Soreq Nuclear Center.

9.7.3. High radiation tests

The TGC cosmic muon efficiency was also tested under a high flux of photons from a 47 Ci ^{60}CO source at the Soreq Nuclear Research Center, Israel. While the experimental setup was very similar to the setup at Demokritos (using large prototype instead of the small quadruplet). The large area detectors performed well (i.e. with high single plane efficiencies) up to background radiation levels of approximately $17\,\mathrm{kHz/cm}^2$ of detected photons (see Fig. 9.12).

9.8. Prospect

The proposed NSW will allow the ATLAS muon system to maintain its full trigger acceptance and its excellent muon tracking at the highest LHC luminosities expected. At the same time the Level-1 single muon (typically $p_T > 20\,\mathrm{GeV}$) triggers rate will be kept at an acceptable level. The design of the NSW meets the requirement for very good segment angle resolution of 1 mrad at the Level-1 trigger level. This angular resolution allows for a powerful background rejection in the track density NSW environment. It is also an important step towards a further improvement of the muon Level-1 trigger system foreseen in the Phase-II upgrade for even higher luminosity. This Phase-II upgrade will substantially improve the p_T resolution of the Level-1 muon system.

The NSW project consists of R&D of detector technology and electronics. The schedule for installation is 2018 at LS2.

Appendix A.

Muon trigger efficiency

In this appendix, a more detail description on the creation of the muon trigger efficiency maps, for both data and MC, is presented. The way to determine the efficiency is by using the "tag-and-probe" method, which reconstructs $J/\psi \rightarrow \mu^+\mu^-$ decays to select a very pure dimuon sample. The trigger efficiency is defined as the fraction of events where the muon is matched to the corresponding high level trigger (HLT) objects.

A.0.1. Trigger efficiency

The three terms contributing to our estimate of the dimuon trigger efficiency (ϵ_{RoI} , c_a , and $c_{\Delta R}$ in equations 6.1.2, 6.1.3) are measured in data using offline reconstructed dimuon events (using the same quality cuts mentioned in the section 4) taken with three different types of triggers:

1. `EF_mu18`, `EF_mu20`, `EF_mu24`, `EF_mu36`: a single muon trigger with 18 GeV, 20 GeV, 24 GeV and 36 GeV thresholds;
2. `EF_2mu4_DiMu_NoVtx_NoOS`: a dimuon triggers where both muons are required to have p_{T} $>$ 4 GeV, but where no cuts are made on dimuon vertex quality or on the charge of the two muons;
3. `EF_2mu4_Jpsimumu_L2starB`: the standard dimuon trigger used in this analysis.

Asymptotic dimuon correction

The asymptotic dimuon efficiency correction, c_a , which comes from the vertex and opposite-sign requirements, is measured in three different regions of the detector: Barrel ($0.0 < |y^{\mu\mu}| < 1.0$); Overlap ($1.0 < |y^{\mu\mu}| < 1.2$); and Endcap ($1.2 < |y^{\mu\mu}| < 2.3$); We have verified that the variation of c_a within a region is small for $\Delta R > 0.3$ as shown in Fig. A.1.

The values of the correction in the three regions are derived from the ratio of $J/\psi \to \mu^+\mu^-$ decays fitted from dimuon candidates with $M_{\mu\mu}$ of 2.6–4.1 GeV (excluding the ψ' range, 3.5–3.75 GeV) in samples collected with the `EF_2mu4_Jpsimumu_L2starB` and `EF_2mu4_DiMu_NoVtx_NoOS` triggers:

$$c_a(|y^{\mu\mu}|) = \frac{N_{J/\psi}(EF\_2mu4\_Jpsimumu\_L2starB)}{N_{J/\psi}(EF\_2mu4\_DiMu\_NoVtx\_NoOS)} \tag{A.0.1}$$

In this ratio, all the efficiency terms (RoI, ΔR , etc.) cancel except for effects due to the vertex and opposite sign cuts. Values of c_a are extracted from events with $\Delta R > 0.3$ as shown in Fig. A.2.

Uncertainties on these values come primarily from the statistics of the control samples. We have checked that systematic effects from changing J/ψ fitting assumptions (single vs. double Gaussian signal shapes) are negligible.

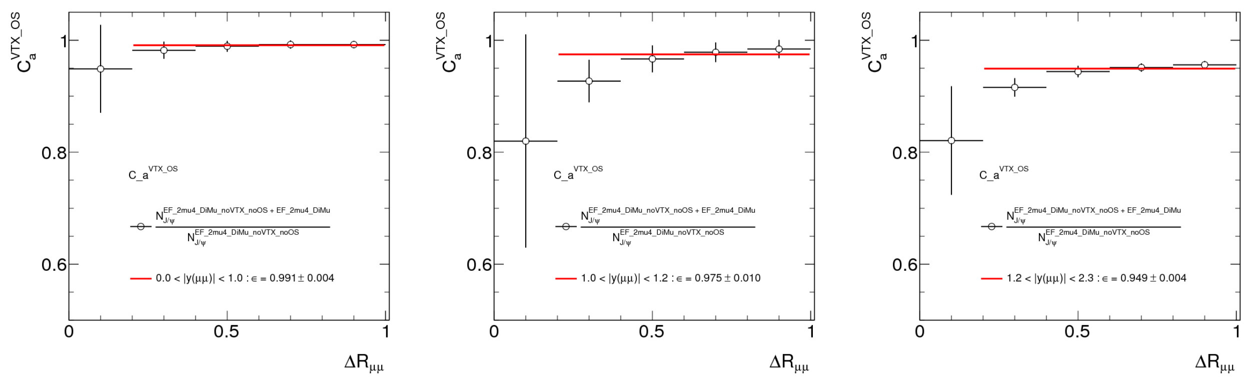

(a) (b) (c)

Figure A.1.: The vertex and opposite sign correction, c_a , as a function of ΔR in the: (a) Barrel; (b) Overlap; and (c) Endcap regions, showing that correction factors are constant in each of the regions for $dR > 0.3$.

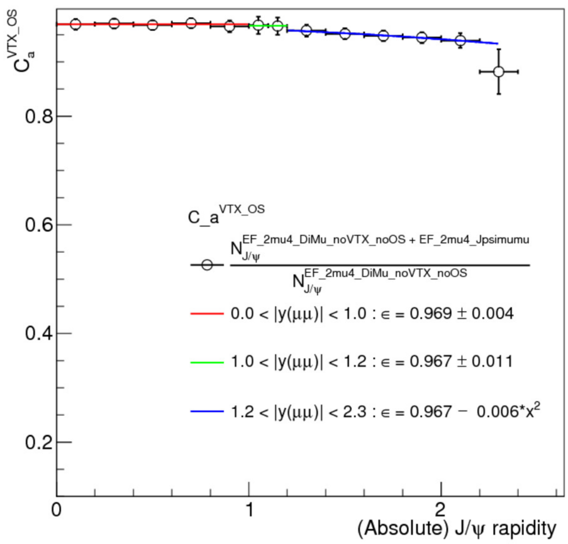

Figure A.2.: The vertex and opposite sign correction, c_a , as a function of $|y^{\mu\mu}|$ in the three detector regions used in the analysis.

The ΔR correction

The dependence of the dimuon trigger efficiency on the spatial separation of the muons, $c_{\Delta R}$, arises from effects of overlapping RoIs. It is derived as a function of the separation, ΔR, between the two muons in the three detector regions used for the vertex and opposite sign correction. To extract this correction we use a sample of dimuon events, with the same quality cuts as in the Υ sample, selected using the `EF_mu18` trigger with the following additional requirements

- $2 < M_{\mu\mu} < 8$ GeV (excluding the J/ψ region, 2.9–3.3) GeV ,
- p_{T} $(\mu_2) > 8$ GeV ,

This control sample is independent of the Υ data sample used in the cross-section calculation and, because of the 8 GeV cut on the lower p_{T} muon, is in the p_{T} plateau of the single muon trigger efficiency for that muon. Distributions of the ratio:

$$\rho_{2-8}(\Delta R, |y^{\mu\mu}|) \equiv \frac{N_{2-8}(EF\_mu18 \cdot EF\_2mu4\_Jpsimumu\_L2StarB)}{N_{2-8}(EF\_mu18)} \tag{A.0.2}$$

are shown in Fig. A.3 for each of the three detector regions. Ratio data in each of the three regions is fit with a function composed of an error function (describing the shape of the ΔR turn-on) and a normalization (corresponding to the plateau value of the data). The fitted error function, which approaches one for $\Delta R \gtrsim 0.3$, corresponds to the correction $c_{\Delta R}$ (ΔR) in each region. The normalization contains contributions from c_a and from the single muon trigger efficiency. It is irrelevant for the extraction of $c_{\Delta R}$ as long as it does not change with the characteristics of the events. This consistency is ensured by the muon p_{T} cut of 8 GeV in this control sample, which puts all of the lower p_{T} muons into the plateau region of the single muon efficiency. Results of these fits are shown in Fig. A.3.

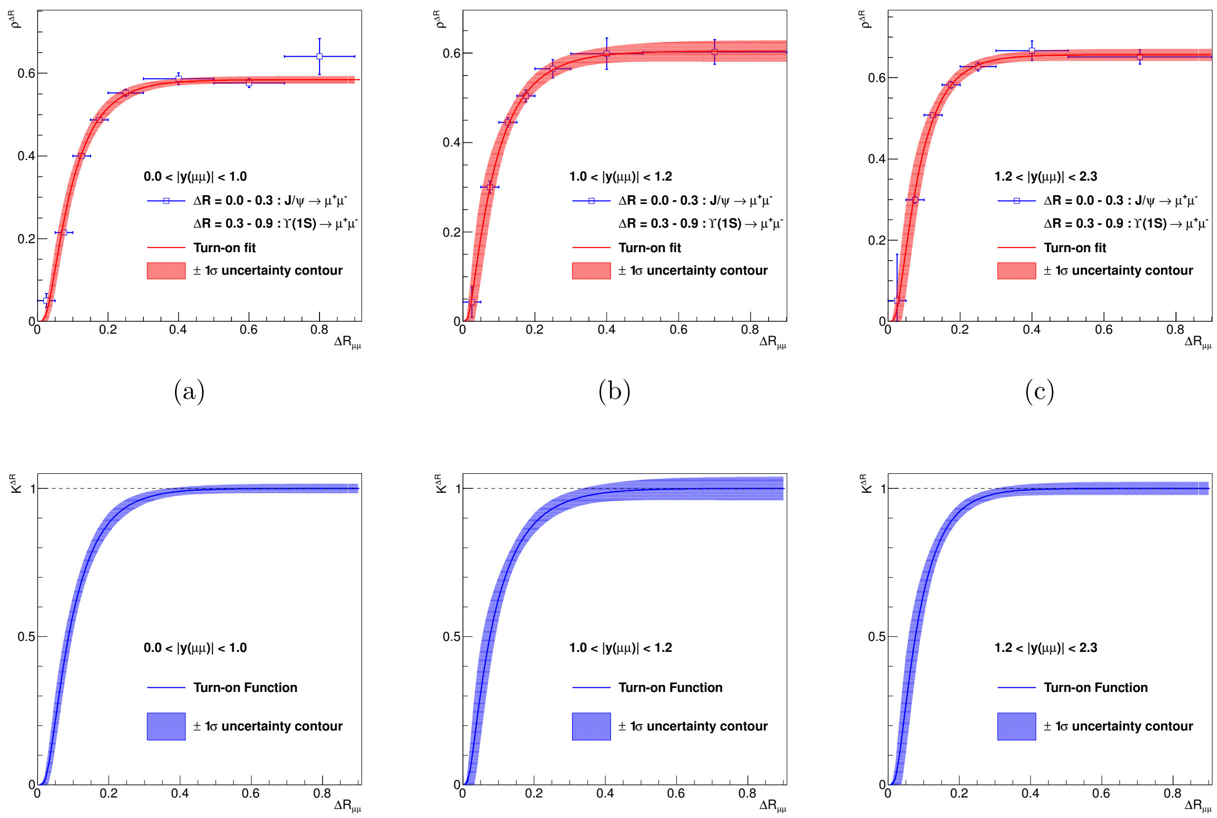

(a) (b) (c)

(d) (e) (f)

Figure A.3.: The ratio, ρ_{2-8}, of dimuon events in the $M_{\mu\mu}$ region 2–8 GeV (excluding the J/ψ range) taken with the `EF_mu18 & EF_2mu4_DiMu` and `EF_mu18` triggers as a function of ΔR between the two muons. Also shown are the correction factors, $c_{\Delta R}$.

The same process was done to the MC samples. For a comparison the same plots are shown in Figure A.4

It can be seen, that the plateau values in the MC are higher by around 30%.

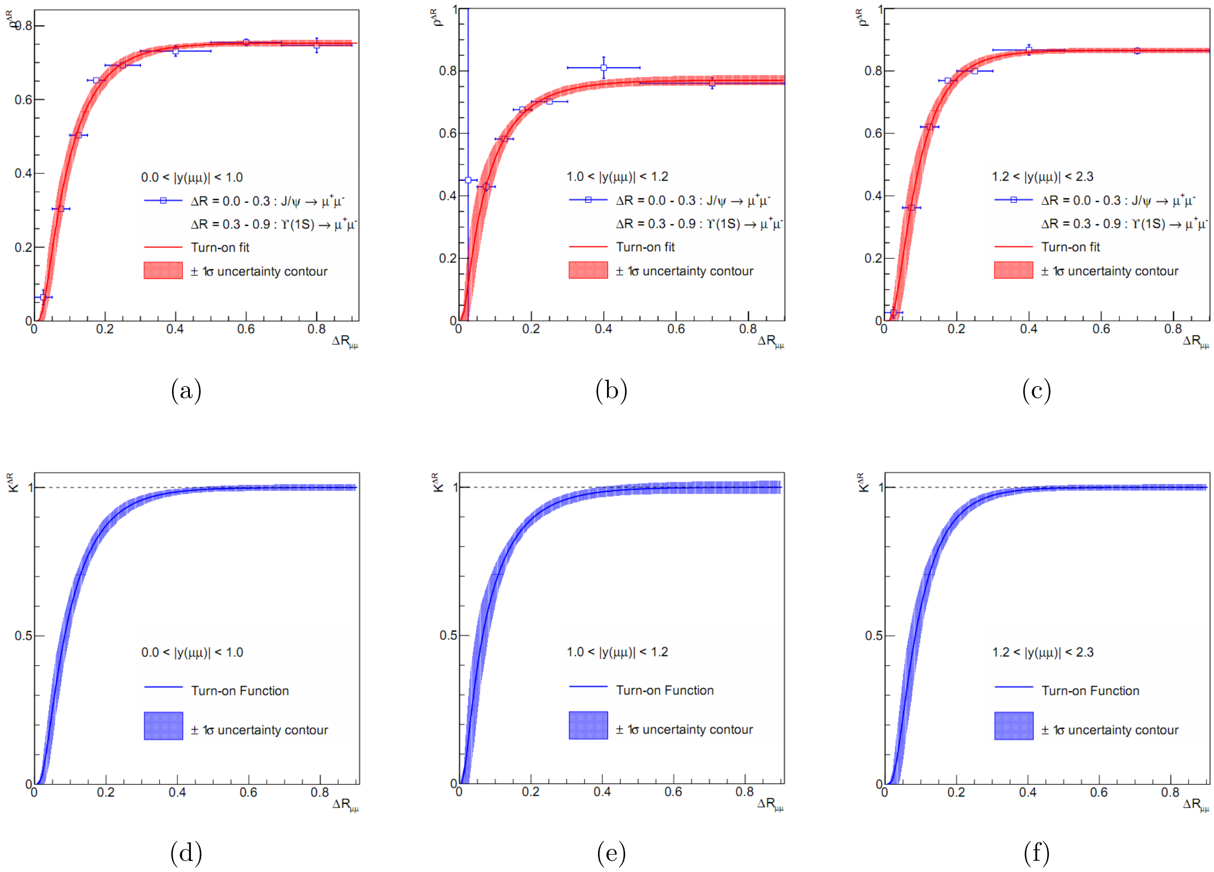

Figure A.4.: The ratio, ρ_{2-8}, of dimuon events in the $M_{\mu\mu}$ region 2–8 GeV (excluding the J/ψ range) taken with the `EF_mu18 & EF_2mu4_DiMu` and `EF_mu18` triggers as a function of ΔR between the two muons. Also shown are the correction factors, $c_{\Delta R}$ for mc.

Total dimuon correction

The total dimuon correction:

$$c_{\mu\mu}(\Delta R, |y^{\mu\mu}|) \equiv c_a(|y^{\mu\mu}|) \times c_{\Delta R}(\Delta R, |y^{\mu\mu}|) \tag{A.0.3}$$

is shown in Fig. A.5 for each of the three regions. Also shown in the figure is the uncertainty band on the correction derived from the uncertainties on c_a and $c_{\Delta R}$.

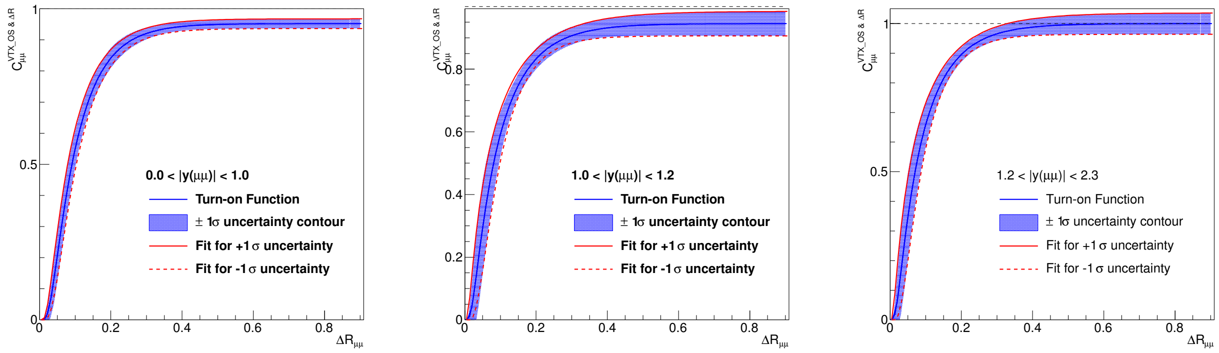

(a) (b) (c)

Figure A.5.: The total dimuon correction factor, $c_{\mu\mu}$, and its uncertainty.

Single muon efficiency

The efficiency to find 4 GeV single muon RoIs is extracted from the ratio:

$$\rho_{J/\psi}(p_{\mathrm{T}}^{\mu 2}, \eta^{\mu 2}, \Delta R, |y^{\mu\mu}|) \equiv \frac{N_{J/\psi}(EF\_mu18 \cdot EF\_2mu4\_Jpsimumu\_L2BstarB)}{N_{J/\psi}(EF\_mu18)} \quad \text{(A.0.4)}$$

derived using $J/\psi \to \mu^+\mu^-$ decays fitted from dimuon candidates with $M_{\mu\mu}$ of 2.6–4.1 GeV (excluding the ψ' range, 3.5–3.75 GeV) in the `EF_mu18` and `EF_mu18 & EF_2mu4_Jpsimumu_L2BstarB` trigger samples. The quantity $\rho_{J/\psi}$ is related to the single muon RoI efficiency, ϵ_{RoI} , by:

$$\epsilon_{RoI}(p_{\mathrm{T}}, q\eta) = \frac{\rho_{J/\psi}(p_{\mathrm{T}}^{\mu 2}, q \cdot \eta^{\mu 2}, \Delta R, |y^{\mu\mu}|)}{c_{\mu\mu}(\Delta R, |y^{\mu\mu}|)} \quad \text{(A.0.5)}$$

We construct ϵ_{RoI} in bins of p_{T} and $q\eta$ by correcting the inputs to $\rho_{J/\psi}$ for $c_{\mu\mu}$ on an event-by-event basis. An examples of these fits, in the range of the analysis (barrel region) are shown in Figure A.6

The resulting efficiency maps, for data and MC are shown in Fig. A.7. Similar charge-dependent pseudorapidity structures and drops in efficiency are seen at low p_T in these single muon efficiency maps and regions of localised efficiency loss can be seen in the barrel-endcap transition region near $|\eta| \sim 1.1$ and the crack at $|\eta| \approx 0$.

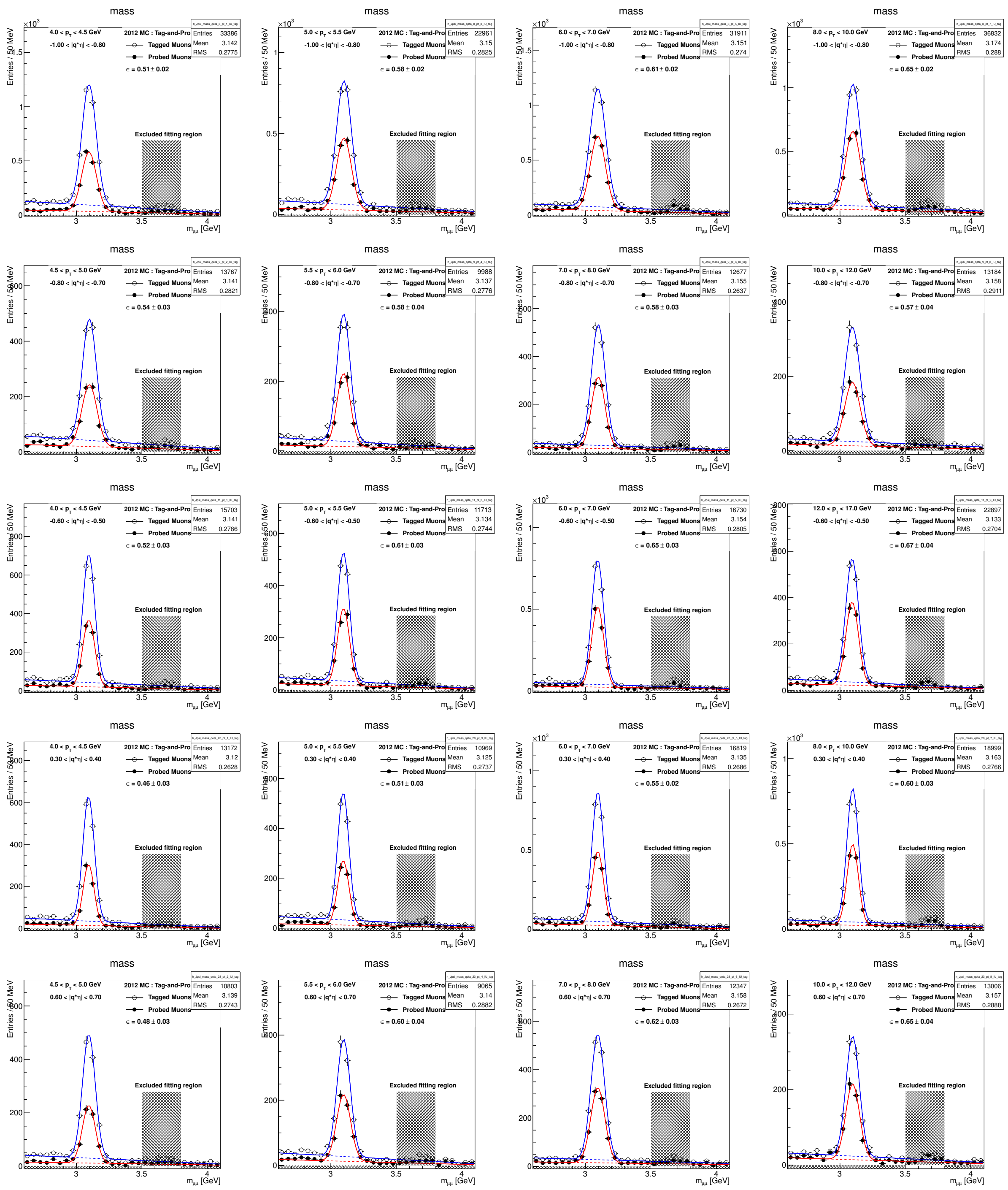

Figure A.6.: An example of the mass fits for the tag-n-prob ratio in the barrel region.

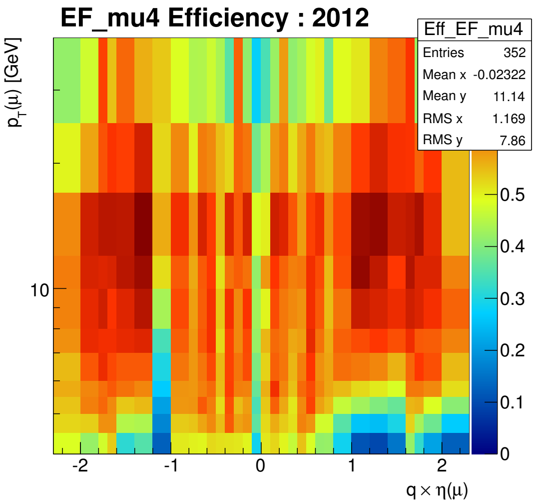

(a)

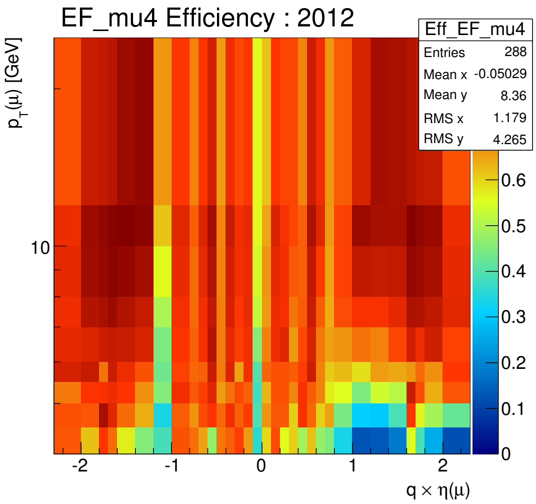

(b)

Figure A.7.: The single muon trigger ROI efficiency, ϵ_{RoI} , for (a) data (b) MC , as a function of muon p_{T} and $q\eta$, to be queried for both muons and combined with the $c_{\mu\mu}(\Delta R, |y^{\mu\mu}|)$ correction factor to arrive at the dimuon efficiency.

Dimuon trigger efficiency

The dimuon trigger efficiency is evaluated for each event in our data sample using:

$$\epsilon_{trig} = \epsilon_{RoI}(p_{\mathrm{T}}^{\mu1}, q \cdot \eta^{\mu1}) \times \epsilon_{RoI}(p_{\mathrm{T}}^{\mu2}, q \cdot \eta^{\mu2}) \times c_{\mu\mu}(\Delta R, |y^{\mu\mu}|) \tag{A.0.6}$$

The technique we use to extract ϵ_{RoI} from $\rho_{J/\psi}$ leads to an anti-correlation between the ϵ_{RoI} terms and $c_{\mu\mu}$. However, the small size of the uncertainties on $c_{\mu\mu}$ compared to those on the binned values of $\rho_{J/\psi}$ means that this correlation produces only a small effect on the size of the uncertainty of ϵ_{trig} . Thus, we neglect this correlation when calculating $\sigma(\epsilon_{trig})$ and derive the uncertainty only from statistical effects on $\rho_{J/\psi}$. This leads to a slight overestimate of $\sigma(\epsilon_{trig})$ because the correlation is negative.

Appendix B.

Muon reconstruction efficiency

This section describes how the ”tag-and-probe” method allows to measure the muon reconstruction efficiency in both data and MC and derive the data/MC scale factors (SF) as a function of p_{T} and $q\eta$.

The basic strategy is to select events with at least one identified and triggered combined muon, and use these tagged events to collect Inner Detector tracks (the “probes”) consistent with coming from a $J/\psi \to \mu\mu$ decay. This method allows measurement of the probe muon efficiency independently from the Muon Spectrometer system.

We use data recorded in 2012 with muon GRL selection.

Using the event selection criteria as described in an earlier section 4 but with requirement of at least one, rather than two, combined muons to be present in the event. Data recorded on the single muon triggers `EF_mu4, EF_mu13, EF_mu15, EF_mu18, EF_mu20` and `EF_mu40` are considered.

The tag muon selection is as follows:

- Identified combined muon associated to a good ID track (described in Section 4 – essentially cuts on SCT, pixel hits and holes and TRT extensions)
- $p_T > 4$ GeV, $|\eta| < 2.5$
- Tag muon must be consistent with having fired the trigger by checking the reconstructed muon is consistent with passing through the $\eta - \phi$ region in the muon spectrometer region of interest corresponding to the trigger muon parameters

Probes are selected by considering any good ID track (defined above) with the following selection:

- $p_T > 4$ GeV, $|\eta| < 2.5$
- Probe + tag must have a successful refit to a common vertex
- A refitted mu+track invariant mass within $2 < m_{mu,trk} < 4.5$ GeV (wide J/ψ signal region)
- $\Delta\eta$ (probe, tag) > 0.4 OR $\Delta\phi$ (probe, tag) > 0.4, to ensure the tag and probe are sufficiently separated in $\eta - \phi$ in the trigger and in reconstruction algorithms

All tag+probe combinations passing the above selection then enter the analysis. We first build the refitted tag+probe invariant mass distribution over the mass window $2 < m < 4.5$ GeV in intervals of probe-charge signed pseudorapidity and probe transverse momentum. A clear J/ψ signal peak is seen over a continuum background originating from real dimuon pairs from heavy flavour decays, Drell-Yan or fakes from decays in flight of kaons and pions, and a large contribution of combinatorial pairs of a single real muon and a non-muon Inner Detector track.

We then query the tag+probe pairs and check whether the probe track was matched to and reconstructed as a combined muon. For those tag+probe candidates where the probe was reconstructed as a muon we build a second invariant mass distribution in the same intervals of probe-charge signed pseudorapidity and probe transverse momentum (still using the Inner Detector track parameters). In this invariant mass spectrum of two identified muons we again see a clear J/ψ signal peak, with reduced background combinatorics.

By fitting the invariant mass spectrum of the unmatched tag+probe candidates (mu+track selection) and extracting a J/ψ candidate yield, and fitting that subset of those candidates where the probe is reconstructed as a muon (the dimuon selection) we can determine the probe muon reconstruction efficiency over the charge signed pseudorapidity and transverse momentum interval considered by taking a ratio of the dimuon J/ψ candidate yield to the mu+track J/ψ candidate yield.

Muon reconstruction binning choice

We consider the following charge signed pseudorapidity and transverse momentum intervals for the efficiency study:

$$q * \eta : -2.5, -2.3, -1.9, -1.7, -1.52, -1.37, -1.3, -1.2, -1.1, -0.8, -0.6, -0.4, -0.2, -0.05, \tag{B.0.1}$$

$$0.05, 0.2, 0.4, 0.6, 0.8, 1.1, 1.2, 1.3, 1.37, 1.52, 1.7, 1.9, 2.3, 2.5 \tag{B.0.2}$$

$$\tag{B.0.3}$$

$$p_T(GeV) : 2.5, 3.25, 4.0, 4.25, 4.5, 4.75, 5.0, 5.25, 5.5, 5.75, 6.0, 6.25 \tag{B.0.4}$$

$$, 6.5, 6.75, 7.0, 7.5, 8.0, 8.5, 9.0, 10.0, 11.0, 12.0, 13.0, 15.0, 17.0, 20.0 \tag{B.0.5}$$

$$, 23.0, 26.0, 30.0, 34.0, 40.0 \tag{B.0.6}$$

Binning is driven by available statistics, balanced against keeping the binning fine enough so as not to integrate over fine (and quickly-varying in η) efficiency structures. Due to the toroidal magnetic field muons with positive (negative) charge are bent toward larger (smaller) pseudorapidity which introduces a charge dependence in the muon reconstruction efficiency. We bin in charge-signed pseudorapidity as negative muons at positive rapidities will be affected in the same manner as positive muons in negative rapidities, so this allows us to combine events and increase our statistical precision where we would otherwise have to bin in three dimensions. The charge dependence is particularly noticeable at very large $|\eta|$ where the muon can be bent outside of the geometrical acceptance of the detector, and at low p_T where the muons (of particular charge) may be bent away from (rather than toward for the opposing charge) the middle/outer spectrometer stations and thus not identified as a muon.

Fitting procedure and efficiency extraction

Refitted (dimuon/muon+track) invariant mass distributions are built over a window of $2-4.5$ GeV. We fit a signal+background fit template from 2.6 GeV to 4.0 GeV in both cases (excluding the mass window $3.5-3.8$ GeV containing the $\psi(2S)$ signal). For the nominal fit we use a single Gaussian for the signal description and a second order polynomial to describe the background. The means of the mu+track and mu+mu fits are allowed to be determined independently. The ratio of integral of the signal yield in the dimuon signal fit to the signal yield in the mu+track signal fit is identified as the probe muon reconstruction efficiency in the charge-signed pseudorapidity and transverse momentum bin studied. Examples of fits to the dimuon mass spectrum in the J/ψ region, from which reconstruction efficiencies are derived are shown in Fig. B.1.

Statistical uncertainties on the two signal yields are taken directly from the fits, and are propagated through to the efficiency measurement taking into account correlations between the mu+track sample and the subset of data contained in the dimuon sample. Systematic

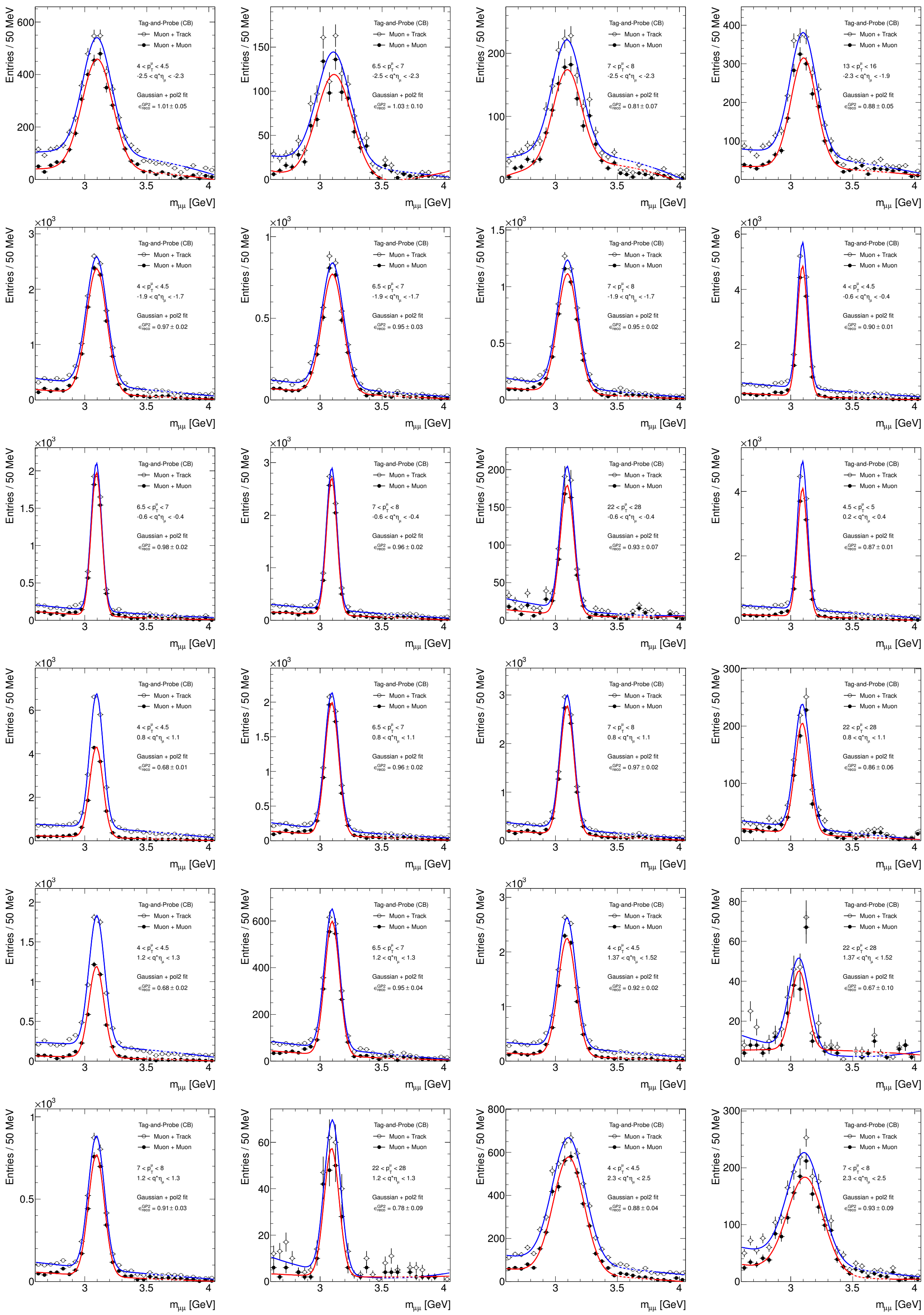

Figure B.1.: Example fits to dimuon mass spectra in the J/ψ mass region used to derive the muon reconstruction efficiency for a set of charge-signed pseudorapidty and p_T intervals.

checks include fixing a common mean between the dimuon and muon+track fits, varying the background shape to a third order polynomial, varying the signal description to a double Gaussian with means and resolutions allowed to vary independently. No noticeable period dependence to the efficiencies was observed over the data periods studied. The maximal variation up and down of the systematic variations was assigned as the systematic uncertainty on the efficiency measurement.

Resultant efficiency measurement

The resultant 2D muon reconstruction efficiency map is shown in Fig. B.2. Slices of the 2D map in $p_{\mathrm{T}}(\mu)$ and $q \cdot \eta$ (which show the overall uncertainties) are shown in Fig. B.3 and B.4. Statistical uncertainties are shown by the black error bars, statistical and systematic uncertainties added in quadrature are shown as a shaded blue region. Statistical uncertainties dominate over systematic uncertainties over the bulk of the phase space, with except at very low p_T and central rapidities.

Significant structure is observed as a function of charge-signed pseudorapidity at low p_T and in some limited areas efficiency drops can be seen in the transition region between the barrel and end-cap, the $\eta = 0$ crack region and at the very edge of geometrical acceptance near $|\eta| \sim 2.5$ over the full p_T region studied.

Charge-dependent effects persist up to $p_T \sim 11$ GeV beyond which efficiencies are largely symmetric in both the positive and negative-signed pseudorapidities. As a function of p_T there are noticeable drops in efficiency at high p_T in the transition region and at the extreme edges of pseudorapidity acceptance (albeit with large uncertainties of order 20% in these regions).

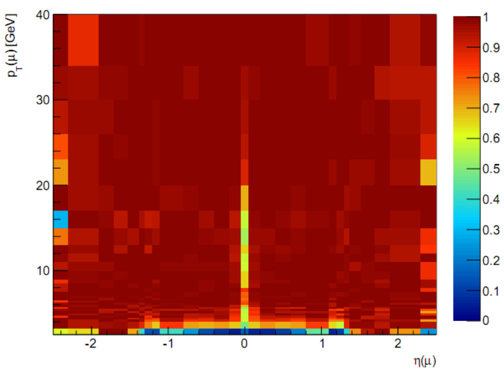

Figure B.2.: The muon reconstruction efficiency map determined from 2012 data as a function of muon pseudorapidity and muon p_T.

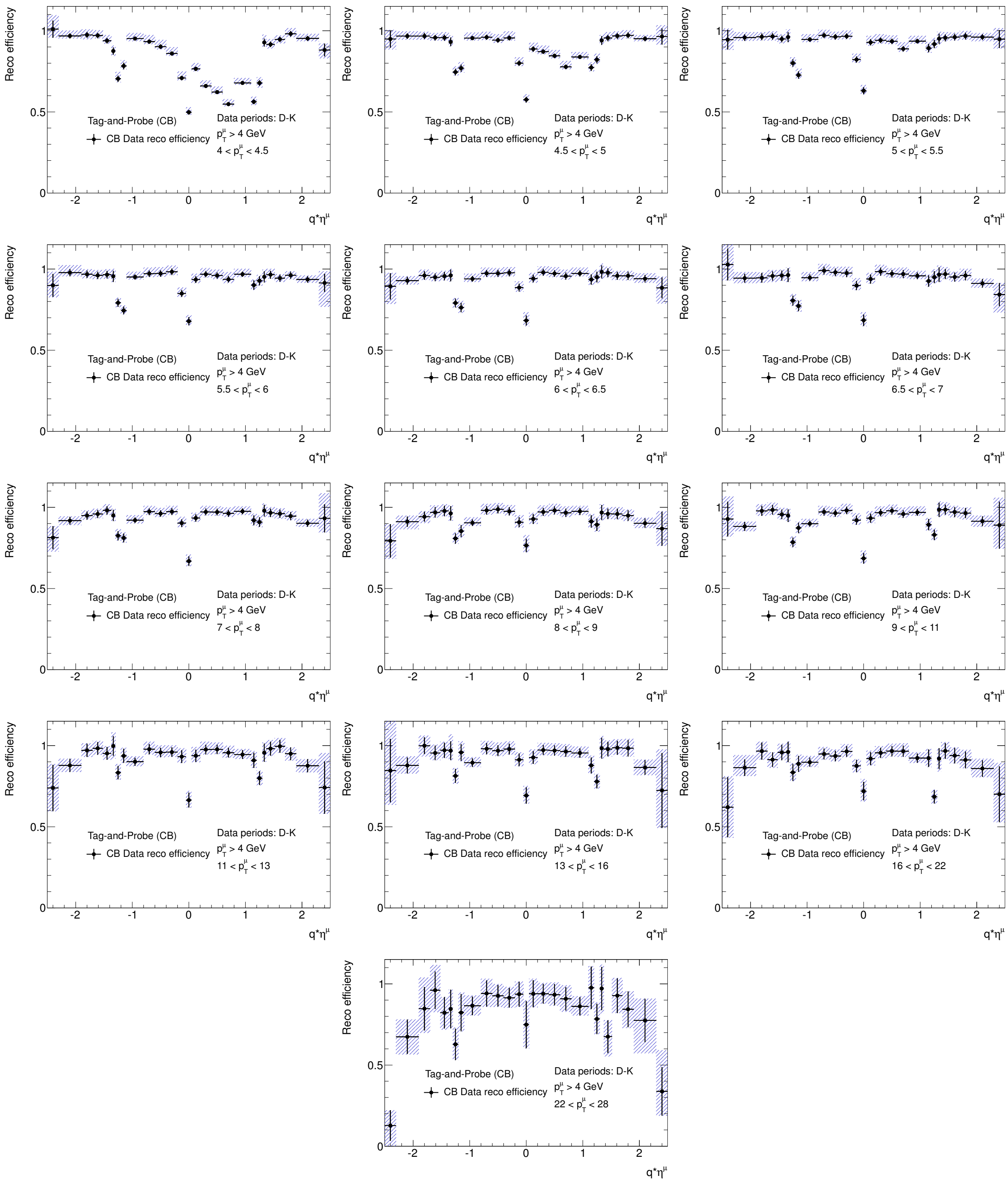

Figure B.3.: Slices of the 2D muon reconstruction efficiency vs. $q \cdot \eta$ for various muon p_T intervals.

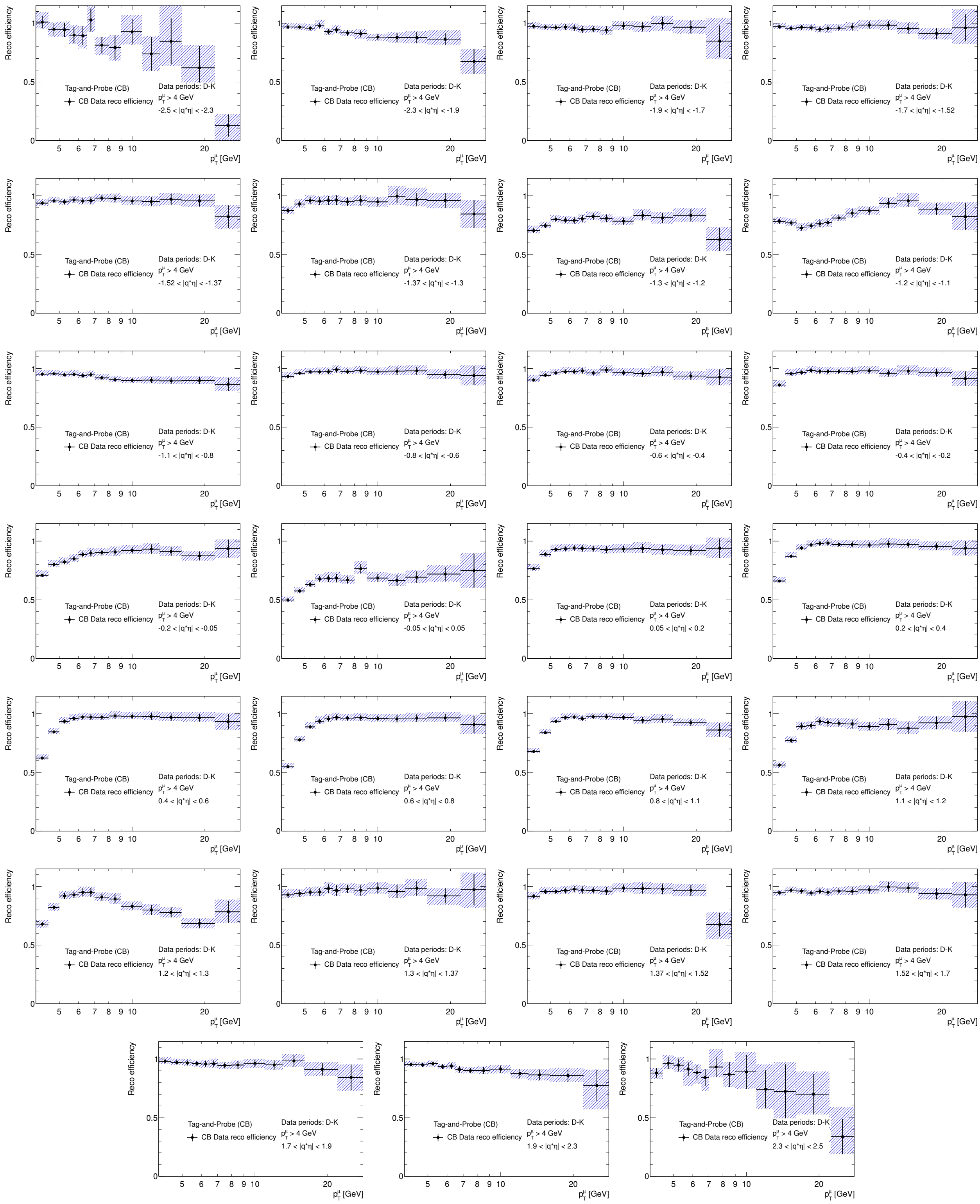

Figure B.4.: Slices of the 2D muon reconstruction efficiency vs. muon p_T for various $q \cdot \eta$ intervals.

Appendix C.

Efficiency validation

The reconstruction and trigger efficiency method has being validated using MC sample. For this purpose we used three MC samples, two sample of J/ψ (that are used and described in section 6.2) and one $\Upsilon(1S) \to \mu 4 mu 4$ sample, needed for the trigger efficiency corrections (as describe in appendix A).

The test of the method was performed in the region of the analysis, i.e. in the rapidity region between 0.2-0.8 and with p_{T} up to 70 GeV.

In order to test the reconstruction efficiency map, we divide two distributions:

- $y - p_{\mathrm{T}}$ of the reweighed reconstructed J/ψs after kinematic cuts and all reconstructed requirements
- $y - p_{\mathrm{T}}$ of truth J/ψs after kinematic cuts

The reconstructed distribution is weighted on event-by-event base by $1/\epsilon_{reco}$, where ϵ_{reco} is the total reconstruction efficiency for the event (see Eq. 6.1.1). A closure is achieved if the result of the ratio is equal to 1 within the uncertainty. In the case:

- Closure > 1, the efficiency is underestimated
- Closure < 1, the efficiency is overestimated

The result of the reconstruction efficiency closure test is presented in Figure C.1.

The green bins represent the values of $1 \pm 5\%$. It can be seen that closure is achieved in all region of the analysis, except the two lowered bins in the p_{T} and $q\eta$ bins, where the efficiency there is overestimated. The errors presented here are only statistical one with no systematics.

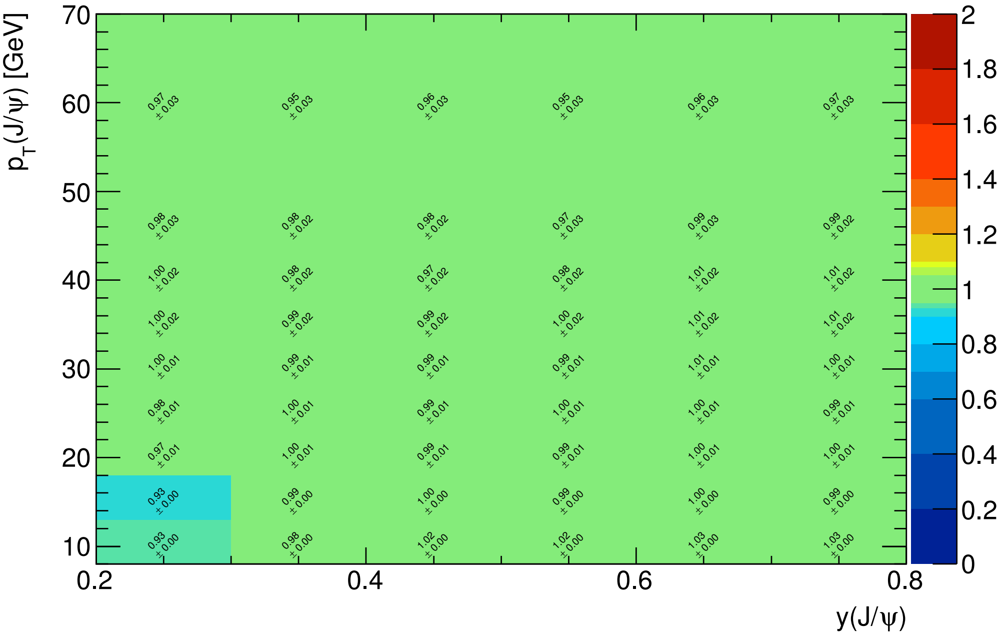

Figure C.1.: The reconstruction efficiency closure test results in bins of J/ψ rapidity and p_{T} in the region of the analysis.

The same test was done in order to validate the trigger efficiency method. This time the two distributions that were divide are:

- $y - p_{\mathrm{T}}$ of the reweighed reconstructed J/ψs after kinematic cuts and all reconstructed requirements that pass the analysis trigger (including trigger matching)
- $y - p_{\mathrm{T}}$ of reconstructed J/ψs after kinematic cuts and all reconstructed requirements

where the reweighing is event base and is 1 over the trigger efficiency (including all corrections).

The closure result are shown in Figure C.2, in bins of J/ψ p_{T} and rapidity.

It can be seen that in most of the bins the values are consistent with 1. In the high p_{T} region the values tend to drop in some of the rapidity bins. Closure that is lower than 1 means that the average weight is too small, that means that efficiency estimate is too high.

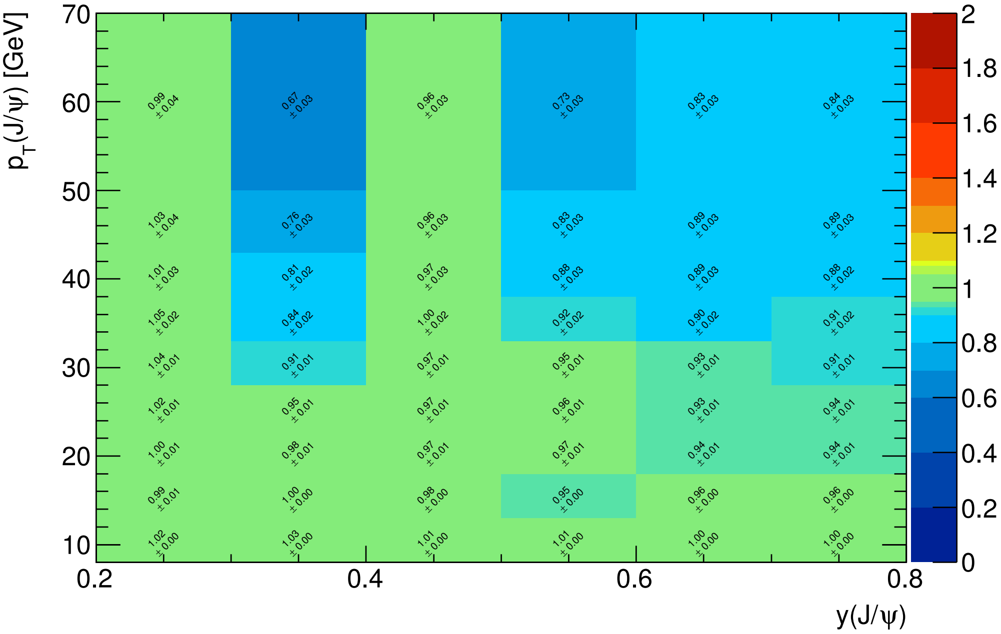

Figure C.2.: The trigger efficiency closure test results in bins of J/ψ rapidity and p_T in the region of the analysis.

Appendix D.

Fraction analysis complementary material

The full parameters results for the fraction analysis are presented in Tables D.1, D.2

Table D.1.: Fraction fit results for the different J/ψ p_T slices. f_{signal} is the relative fraction of the J/ψs in the sample and f_{prompt} is the fraction of the prompt J/ψ from that part.

p_T GeV	f_{signal}	f_{prompt}	f_{Gauss}	μ GeV	σ_{Gauss} GeV	σ_{CB} GeV	σ_{tot} GeV
8.00- 8.50	0.8449 ± 0.0010	0.73903 ± 0.00093	0.542 ± 0.039	3.093052 ± 0.000066	0.03091 ± 0.00050	0.04495 ± 0.00075	0.03799 ± 0.00010
8.50- 9.00	0.8518 ± 0.0012	0.72460 ± 0.00076	0.321 ± 0.018	3.093298 ± 0.000055	0.04839 ± 0.00062	0.03239 ± 0.00022	0.038261 ± 0.000090
9.00- 9.50	0.8506 ± 0.0011	0.71147 ± 0.00070	0.315 ± 0.015	3.093518 ± 0.000049	0.04911 ± 0.00056	0.03260 ± 0.00019	0.0385714 ± 0.0000792
9.50- 10.00	0.8499 ± 0.0010	0.69710 ± 0.00068	0.307 ± 0.015	3.093538 ± 0.000048	0.04995 ± 0.00057	0.03289 ± 0.00019	0.03894 ± 0.00019
10.00- 10.50	0.8457 ± 0.0011	0.68453 ± 0.00069	0.333 ± 0.015	3.093919 ± 0.000048	0.04946 ± 0.00054	0.03259 ± 0.00020	0.03904 ± 0.00019
10.50- 11.00	0.83537 ± 0.00096	0.66972 ± 0.00070	0.572 ± 0.019	3.093791 ± 0.000047	0.03194 ± 0.00027	0.04836 ± 0.00049	0.03980 ± 0.00045
11.00- 11.50	0.8330 ± 0.0010	0.65606 ± 0.00073	0.576 ± 0.027	3.093877 ± 0.000049	0.03195 ± 0.00038	0.04867 ± 0.00069	0.039901 ± 0.000093
11.50- 12.00	0.8311 ± 0.0010	0.64323 ± 0.00077	0.547 ± 0.025	3.094087 ± 0.000052	0.03160 ± 0.00035	0.04816 ± 0.00060	0.039954 ± 0.000094
12.00- 13.00	0.84012 ± 0.00091	0.62329 ± 0.00059	0.266 ± 0.012	3.094130 ± 0.000039	0.05351 ± 0.00061	0.03376 ± 0.00016	0.03997 ± 0.00016
13.00- 14.00	0.8349 ± 0.0011	0.59942 ± 0.00066	0.264 ± 0.011	3.094177 ± 0.000045	0.05418 ± 0.00062	0.03387 ± 0.00015	0.040251 ± 0.000087
14.00- 15.00	0.8329 ± 0.0012	0.57676 ± 0.00075	0.26 ± 0.012	3.094281 ± 0.000050	0.05470 ± 0.00072	0.03408 ± 0.00017	0.04046 ± 0.00010
15.00- 16.00	0.8286 ± 0.0013	0.55415 ± 0.00084	0.25 ± 0.013	3.094484 ± 0.000056	0.05565 ± 0.00086	0.03440 ± 0.00019	0.04073 ± 0.00011
16.00- 18.00	0.8252 ± 0.0012	0.52959 ± 0.00071	0.281 ± 0.012	3.094546 ± 0.000048	0.05457 ± 0.00064	0.03417 ± 0.00017	0.04094 ± 0.00059
18.00- 20.00	0.8214 ± 0.0015	0.49653 ± 0.00089	0.260 ± 0.016	3.094598 ± 0.000060	0.05672 ± 0.00099	0.03486 ± 0.00023	0.04168 ± 0.00013
20.00- 25.00	0.8172 ± 0.0035	0.45102 ± 0.00096	0.718 ± 0.019	3.094628 ± 0.000069	0.03569 ± 0.00030	0.0597 ± 0.0013	0.04381 ± 0.00083
25.00- 30.00	0.7990 ± 0.0027	0.4058 ± 0.0014	0.686 ± 0.036	3.09497 ± 0.00011	0.03592 ± 0.00054	0.0586 ± 0.0018	0.0443 ± 0.0013
30.00- 40.00	0.7905 ± 0.0029	0.3721 ± 0.0017	0.632 ± 0.061	3.09514 ± 0.00013	0.03689 ± 0.00088	0.0574 ± 0.0024	0.04552 ± 0.00033
40.00- 50.00	0.809 ± 0.011	0.3466 ± 0.0034	0.341 ± 0.054	3.09544 ± 0.00028	0.0634 ± 0.0030	0.03890 ± 0.00099	0.04865 ± 0.00055
50.00- 70.00	0.8500 ± 0.0088	0.3284 ± 0.0052	0.144 ± 0.014	3.09558 ± 0.00045	0.0920 ± 0.0079	0.04585 ± 0.00054	0.0549 ± 0.0011

Table D.2.: Parameters of the decay part from the fraction fit results for the different J/ψ p_{T} slices.

p_T GeV	f_{Gauss}	σ_{Gauss1} ps	σ_{Gauss2} ps	σ_{tot} ps
8.00- 8.50	0.7566 ± 0.0055	0.09003 ± 0.00041	2.309 ± 0.015	0.12906 ± 0.00040
8.50- 9.00	0.7195 ± 0.0043	0.08779 ± 0.00033	2.362 ± 0.011	0.13268 ± 0.00033
9.00- 9.50	0.6996 ± 0.0039	0.08550 ± 0.00030	2.3737 ± 0.0093	0.13224 ± 0.00029
9.50- 10.00	0.6920 ± 0.0037	0.08316 ± 0.00029	2.4118 ± 0.0088	0.13106 ± 0.00028
10.00- 10.50	0.6890 ± 0.0036	0.08124 ± 0.00028	2.4325 ± 0.0088	0.12920 ± 0.00028
10.50- 11.00	0.6835 ± 0.0037	0.07908 ± 0.00028	2.4541 ± 0.0090	0.12725 ± 0.00028
11.00- 11.50	0.6824 ± 0.0039	0.07773 ± 0.00029	2.4484 ± 0.0093	0.12499 ± 0.00029
11.50- 12.00	0.6770 ± 0.0040	0.07519 ± 0.00030	2.4745 ± 0.0098	0.12252 ± 0.00030
12.00- 13.00	0.6742 ± 0.0031	0.07311 ± 0.00022	2.4858 ± 0.0075	0.11985 ± 0.00023
13.00- 14.00	0.6772 ± 0.0034	0.07071 ± 0.00025	2.5119 ± 0.0086	0.11649 ± 0.00025
14.00- 15.00	0.6690 ± 0.0039	0.06774 ± 0.00027	2.5430 ± 0.0098	0.11353 ± 0.00028
15.00- 16.00	0.6595 ± 0.0043	0.06491 ± 0.00030	2.555 ± 0.011	0.11020 ± 0.00031
16.00- 18.00	0.6641 ± 0.0036	0.06233 ± 0.00024	2.5928 ± 0.0097	0.10654 ± 0.00026
18.00- 20.00	0.6683 ± 0.0046	0.05908 ± 0.00029	2.651 ± 0.013	0.10231 ± 0.00032
20.00- 25.00	0.6739 ± 0.0047	0.05427 ± 0.00029	2.760 ± 0.015	0.09643 ± 0.00035
25.00- 30.00	0.6711 ± 0.0072	0.04866 ± 0.00041	2.854 ± 0.025	0.08907 ± 0.00053
30.00- 40.00	0.6673 ± 0.0085	0.04361 ± 0.00047	3.020 ± 0.032	0.08390 ± 0.00066
40.00- 50.00	0.694 ± 0.017	0.04069 ± 0.00085	3.077 ± 0.071	0.0771 ± 0.0013
50.00- 70.00	0.673 ± 0.028	0.0339 ± 0.0013	3.16 ± 0.12	0.0674 ± 0.0020

Appendix E.

Spin-alignment complementary material

Results of toy MC tests are presented in Figures E.1 - E.3 of the mean values of λ_{θ^*},λ_{ϕ^*}, and $\lambda_{\theta^*\phi^*}$ respectively. In Figure E.4 all the $\cos\theta^*$ projection of the fit are presented, and in Figure E.5 all the ϕ^* projection of the fit are presented.

Table E.1 summarize all correlation coefficients between the spin-alignment parameters.

Table E.1.: Spin-alignment fit correlation between parameters for the different J/ψ p_{T} slices.

p_T GeV	$\lambda_{\theta^*-\phi^*}$	$\lambda_{\theta^*-\theta^*\phi^*}$	$\lambda_{\phi^*-\theta^*\phi^*}$
9-12	-0.267	-0.018	-0.018
12-14	-0.12	-0.01	0.03
14-16	-0.042	-0.001	-0.009
16-18	-0.01	-0.001	-0.023
18-20	0.021	0.007	0.027
20-25	0.042	-0.001	0.01
25-30	0.08	0.006	0.009
30-40	0.097	-0.007	0.003
40-50	0.124	0.015	0.01
50-70	0.157	-0.052	-0.007

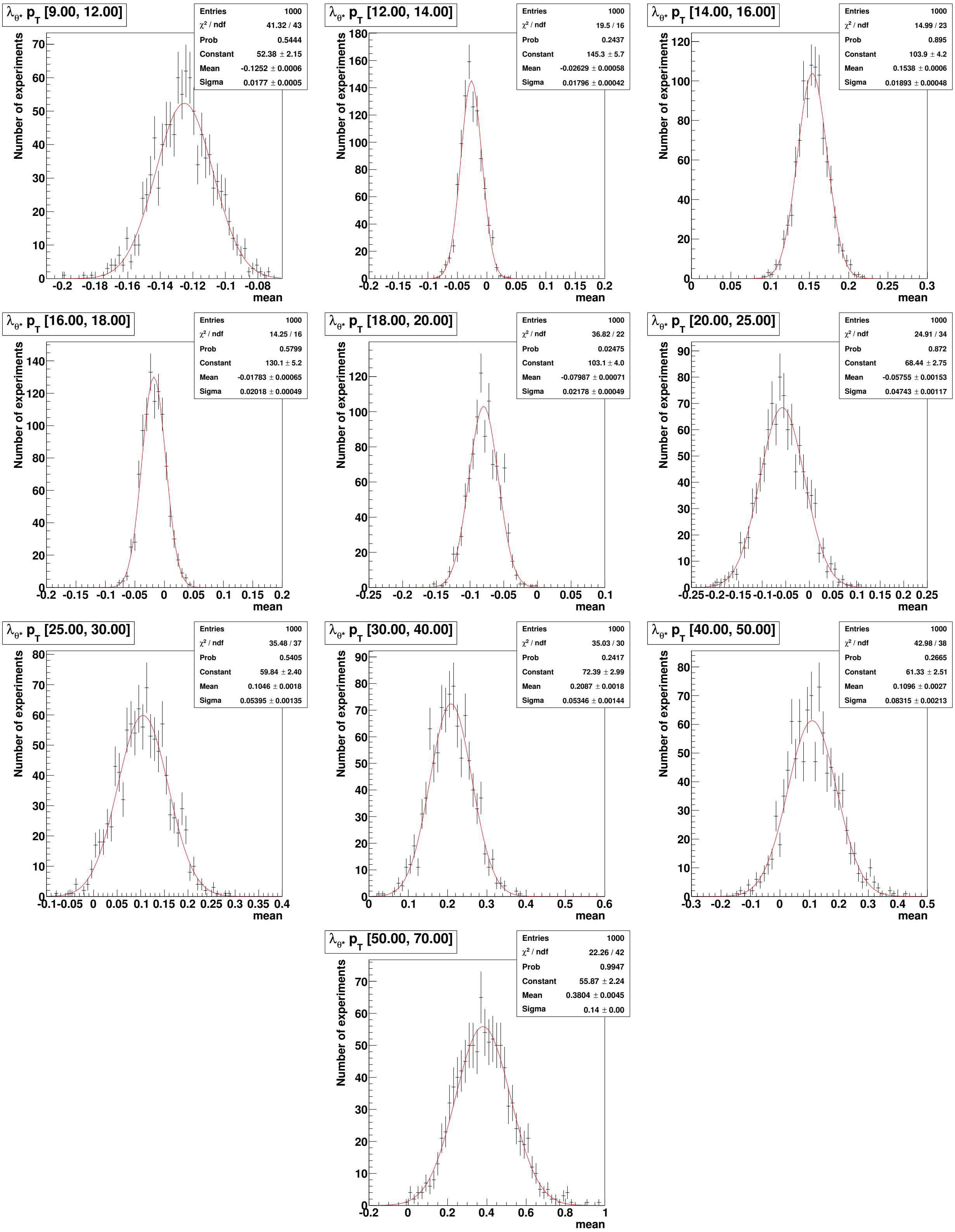

Figure E.1.: Distribution of λ_{θ^*} from 1000 toy MC tests, done with the same statistics of the data sample, and with the same measured polarization.

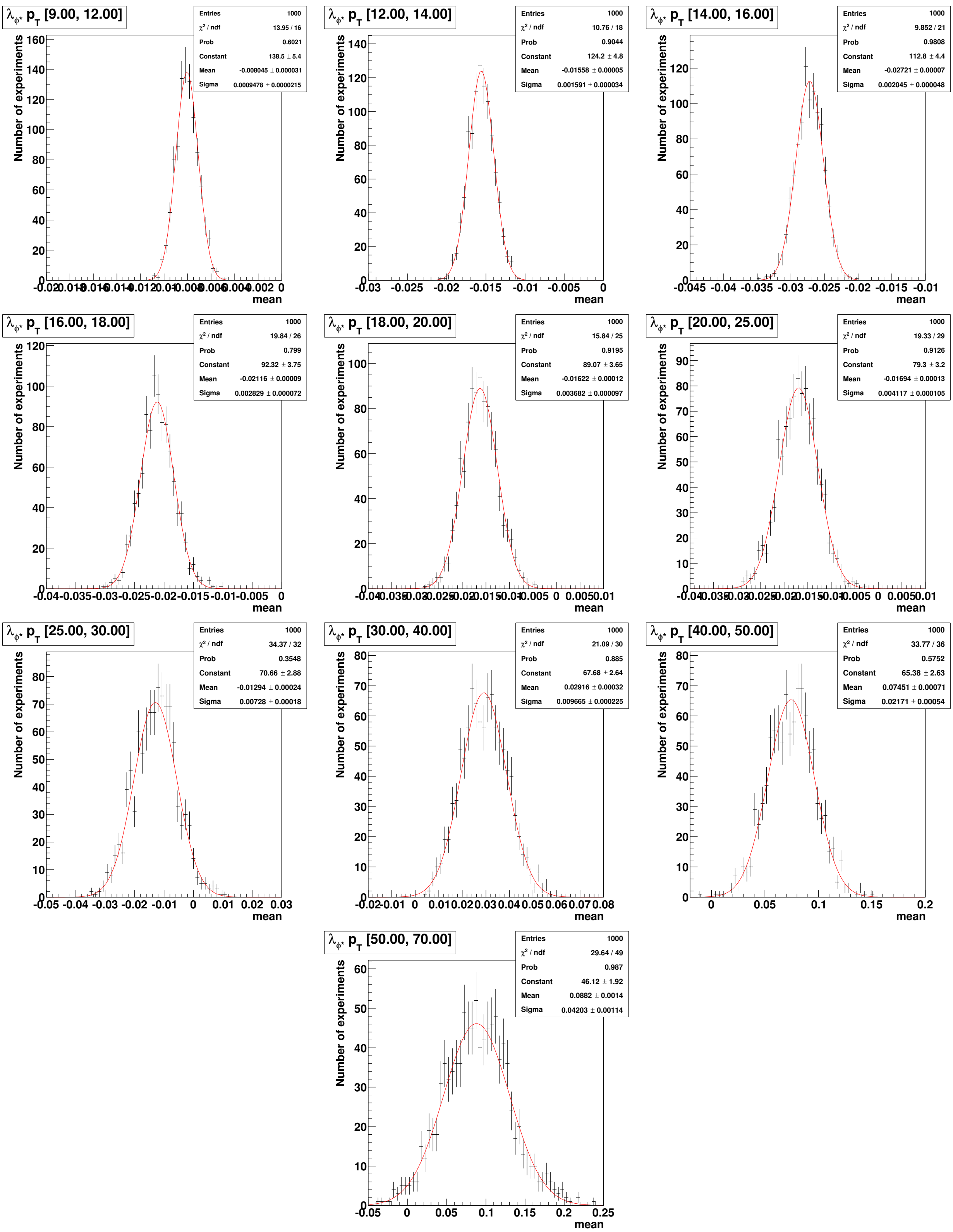

Figure E.2.: Distribution of λ_{ϕ^*} from 1000 toy MC tests, done with the same statistics of the data sample, and with the same measured polarization.

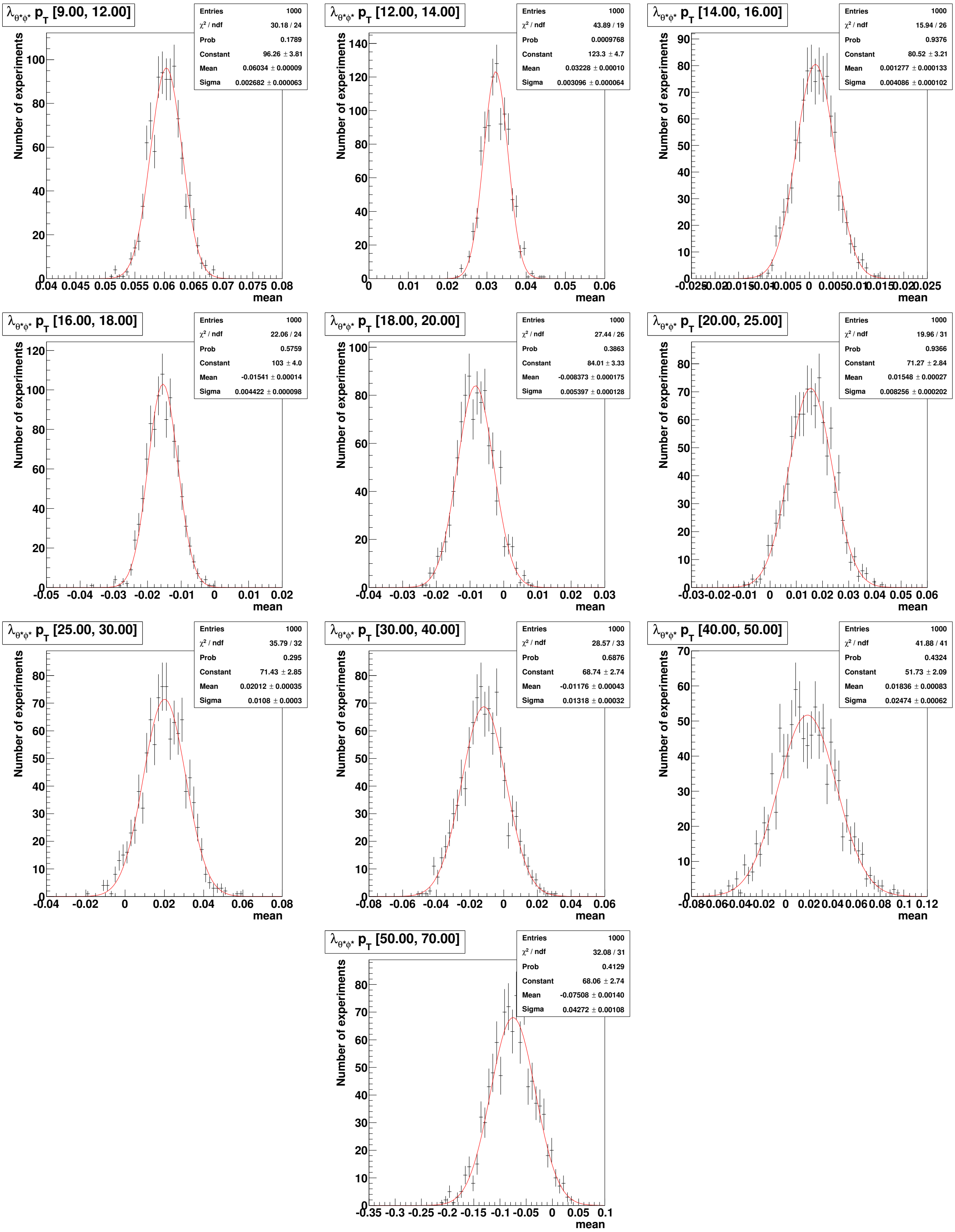

Figure E.3.: Distribution of $\lambda_{\theta^*\phi^*}$ from 1000 toy MC tests, done with the same statistics of the data sample, and with the same measured polarization.

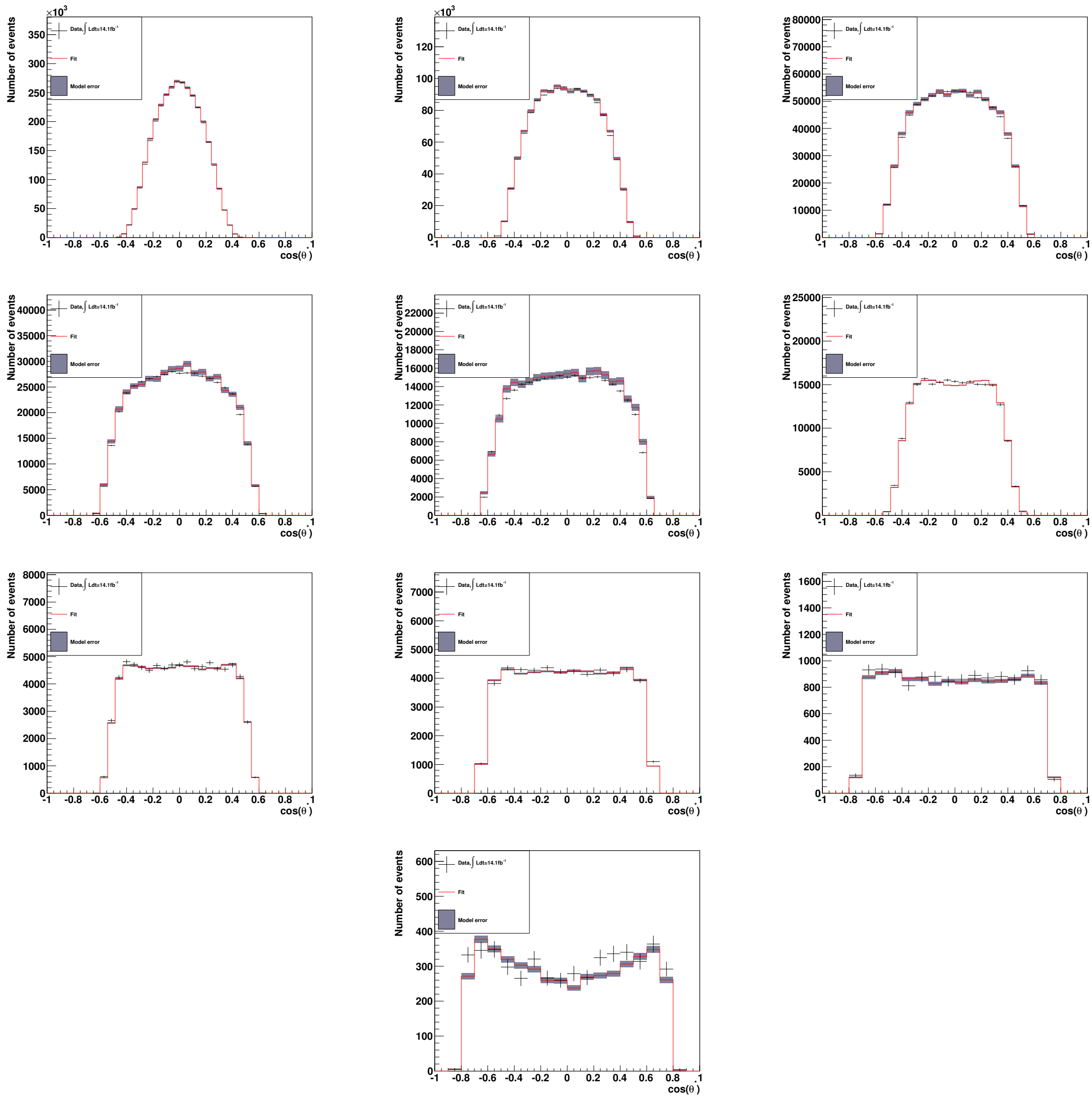

Figure E.4.: Fit projection of $\cos\theta^*$ for all p_{T} slices. Black points represent the data and its statistical errors, red line the fit result, and the gray band represent the error propagation from the model.

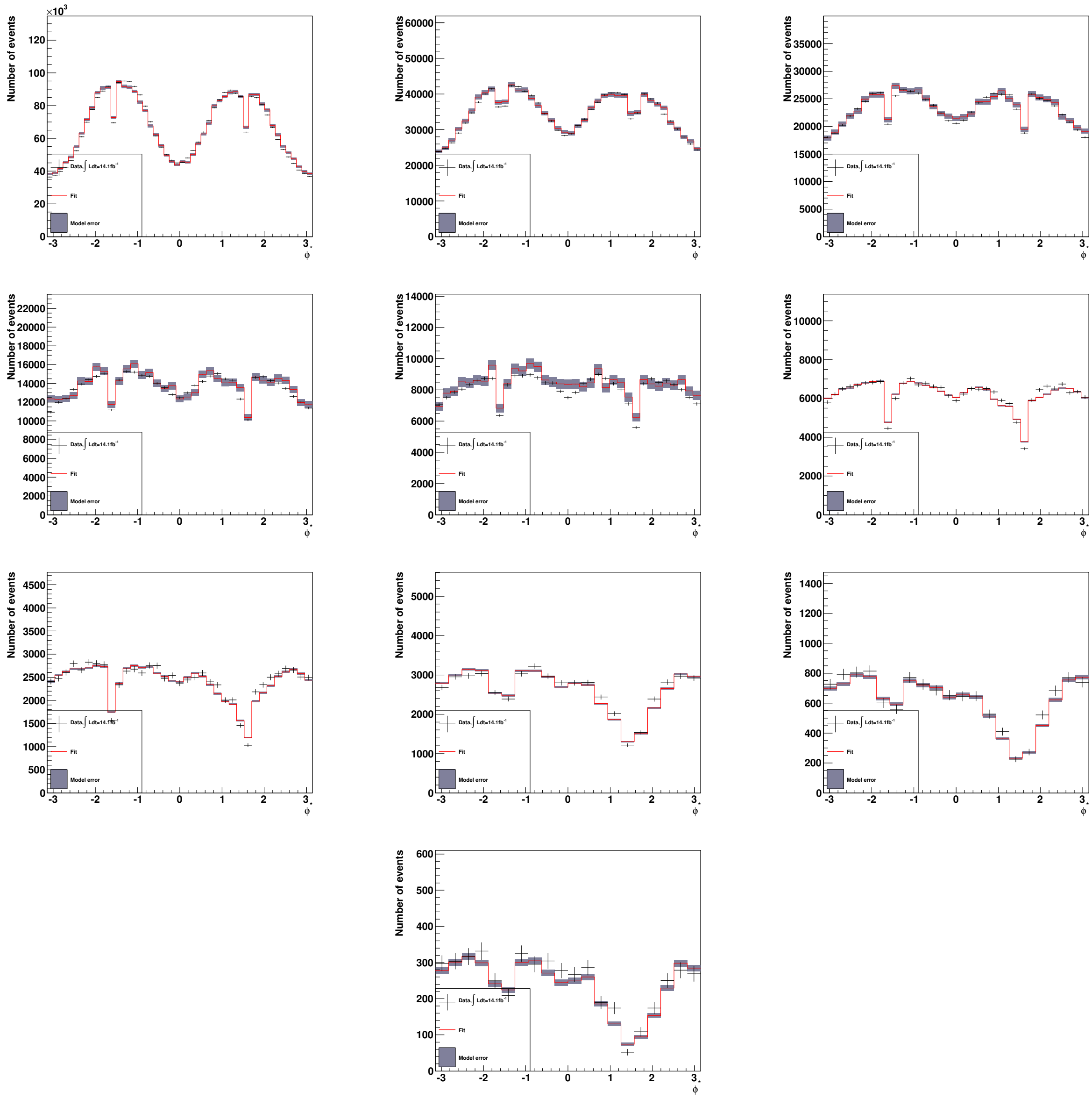

Figure E.5.: Fit projection of ϕ^* for all p_T slices. Black points represent the data and its statistical errors, red line the fit result, and the gray band represent the error propagation from the model.

Bibliography

[1] J. J. Aubert et al., *Experimental Observation of a Heavy Particle J*, Phys. Rev. Lett. **33** (1974) 1404–1406.

[2] J. E. Augustin et al., *Discovery of a Narrow Resonance in e^+e^- Annihilation*, Phys. Rev. Lett. **33** (1974) 1406–1408.

[3] D. Hom et al., *Observation of a Dimuon Resonance at 9.5 GeV in 400-GeV Proton-Nucleus Collisions*, Phys. Rev. Lett. **39** (1977) 252–255.

[4] E. B. G. T. Bodwin and G. P. Lepage, *Rigorous QCD Analysis of Inclusive Annihilation and Production of Heavy Quarkonium*, Phys. Rev. D **51** (1995) 1125–1171.

[5] J. Lansberg, *On the mechanisms of heavy-quarkonium hadroproduction*, Eur.Phys.J. **C61** (2009) 693–703, `arXiv:0811.4005 [hep-ph]`.

[6] Y. Munwes, *My private svn repository*, `https://yonathan-analysis.googlecode.com/svn/trunk/`.

[7] P. Faccioli, C. Lourenco, J. Seixas, and H. K. Wohri, *Towards the experimental clarification of quarkonium polarization*, Eur.Phys.J. **C69** (2010) 657–673, `arXiv:1006.2738 [hep-ph]`.

[8] M. Einhorn and S. Ellis, *Strong production mechanisms and total cross sections of Ψ particles*, Phys. Rev.D (1975) no. 7, 1968–1967.

[9] C. Carlson and R. Suaya, *Hadronic production of the J/Ψ meson*, Phys. Rev. D (1976) no. 14, 3115–3121.

[10] ATLAS Collaboration, G. Aad et al., *Measurement of the differential cross-sections of inclusive, prompt and non-prompt J/ψ production in proton-proton collisions at $\sqrt{s} = 7$ TeV*, Nucl.Phys. **B850** (2011) 387–444, `arXiv:1104.3038 [hep-ex]`.

[11] E. M. G. J. F. Amundson, O. J. P. Eboli and F. Halzen, *Quantitative tests of color evaporation: charmonium production*, Phys. Lett. B **390** (1997) 323–328.

[12] N. Brambilla, S. Eidelman, B. Heltsley, R. Vogt, G. Bodwin, et al., *Heavy quarkonium: progress, puzzles, and opportunities*, Eur.Phys.J. **C71** (2011) 1534, `arXiv:1010.5827 [hep-ph]`.

[13] K.Blum, *Density Matrix Theory and Applications*, Springer **32** (2012) .

[14] K.Gottfried and J. Jackson, *On the connection between production mechanism and decay*

of resonances at high energies, Il Nuovo Cimento Series 10 **33** (1964) 309–330.

[15] J. C. Collins and D. E. Soper, *Angular distribution of dileptons in high-energy hadron collisions*, Physical Review D **16** (1977) no. 7, 2219–2225.

[16] L. Evans and P. Bryant, *LHC Machine*, JINST **3** (2008) S08001.

[17] ATLAS Collaboration, G. Aad et al., *The ATLAS Experiment at the CERN Large Hadron Collider*, JINST **3** (2008) S08003.

[18] CMS Collaboration, S. Chatrchyan et al., *The CMS experiment at the CERN LHC*, JINST **3** (2008) S08004.

[19] LHCb Collaboration, J. Alves, A. Augusto et al., *The LHCb Detector at the LHC*, JINST **3** (2008) S08005.

[20] TOTEM Collaboration, G. Anelli et al., *The TOTEM experiment at the CERN Large Hadron Collider*, JINST **3** (2008) S08007.

[21] ALICE Collaboration, K. Aamodt et al., *The ALICE experiment at the CERN LHC*, JINST **3** (2008) S08002.

[22] Tevatron Collaboration, A. D. Fermi National Accelerator Laboratory, Tevatron *luminosity*, Www. http://www.fnal.gov/pub/now/tevlum.html.

[23] ATLAS Collaboration, G. Aad et al., *The ATLAS Simulation Infrastructure*, Eur.Phys.J. **C70** (2010) 823–874, `arXiv:1005.4568 [physics.ins-det]`.

[24] ATLAS Collaboration, G. Duckeck et al., *ATLAS computing: Technical design report*, .

[25] G. Barrand, I. Belyaev, P. Binko, M. Cattaneo, R. Chytracek, et al., *GAUDI - A software architecture and framework for building HEP data processing applications*, Comput.Phys.Commun. **140** (2001) 45–55.

[26] R. Brun and F. Rademakers, *ROOT - An Object Oriented Data Analysis Framework*, Nucl. Inst. & Meth. in Phys. Res. A. **389** (1997) 81. http://www.fnal.gov/pub/now/tevlum.html.

[27] ATLAS Collaboration, *Search for dilepton resonances in pp collisions at $\sqrt{s} = 7$ TeV with the ATLAS detector*, Phys. Rev. Lett. **107** (2011) 272002.

[28] CMS Collaboration, S. Chatrchyan et al., *Measurement of the prompt J/psi and psi(2S) polarizations in pp collisions at sqrt(s) = 7 TeV*, Phys.Lett. **B727** (2013) 381–402, `arXiv:1307.6070 [hep-ex]`.

[29] B. Gong, L.-P. Wan, J.-X. Wang, and H.-F. Zhang, *Polarization for Prompt J/psi, psi(2s) production at the Tevatron and LHC*, Phys.Rev.Lett. **110** (2013) 042002, `arXiv:1205.6682 [hep-ph]`.

[30] T. Kawamoto, S. Vlachos, L. Pontecorvo, J. Dubbert, G. Mikenberg, P. Iengo, C. Dallapiccola, C. Amelung, L. Levinson, R. Richter, and D. Lellouch, *New Small Wheel*

Technical Design Report, Tech. Rep. CERN-LHCC-2013-006. ATLAS-TDR-020, CERN, Geneva, Jun, 2013. ATLAS New Small Wheel Technical Design Report.

[31] N. Amram, G. Bella, Y. Benhammou, M. A. Diaz, E. Duchovni, E. Etzion, A. Hershenhorn, A. Klier, N. Lupu, G. Mikenberg, D. Milstein, Y. Munwes, O. Sasaki, M. Shoa, V. Smakhtin, and U. Volkmann, *Position resolution and efficiency measurements with large scale Thin Gap Chambers for the super {LHC}*, Nuclear Instruments and Methods in Physics Research A **628** (2011) no. 1, 177 – 181. http://www.sciencedirect.com/science/article/pii/S0168900210015019. Proceedings of the 12th International Vienna Conference on Instrumentation.

[32] Y. Munwes, *Upgrade of the First Level Muon Trigger in the End-Cap New Small Wheel Region of the ATLAS Detector*, Tech. Rep. ATL-DAQ-PROC-2013-005, CERN, Geneva, May, 2013.

[33] ATLAS Collaboration, G. Aad et al., *Letter of Intent for the Phase-I Upgrade of the ATLAS Experiment*, Tech. Rep. CERN-LHCC-2011-012. LHCC-I-020, CERN, Geneva, Nov, 2011.

[34] ATLAS Collaboration, A. Collaboration, *ATLAS muon spectrometer: Technical design report*, .

[35] L. Jeanty, *Data and MC Comparisons for Muon Spectrometer, including Cavern Background*, Presentation at the lpcc simulation workshop, October, 2011.

[36] P. Sala and A. Vannini, *The FLUGG Project*, http://www.fluka.org/content/tools/flugg/, 2013.

[37] ATLAS Collaboration, G. Aad et al., *Letter of Intent for the Phase-II Upgrade of the ATLAS Experiment*, Tech. Rep. CERN-LHCC-2012-022. LHCC-I-023, CERN, Geneva, Dec, 2012. Draft version for comments.

[38] V. Smakhtin, G. Mikenberg, A. Klier, Y. Rozen, E. Duchovni, et al., *Thin Gap Chamber upgrade for SLHC: Position resolution in a test beam*, Nucl.Instrum.Meth. **A598** (2009) 196–200.

[39] O. Sasaki and M. Yoshida, *ASD IC for the thin gap chambers in the LHC Atlas Experiment*, Nuclear Science, IEEE Transactions **46** (1999) 1871 – 1875.

[40] T. Alexopoulos, M. Dris, E. Gazis, E. Katsoufis, M. Kokkoris, A. Lagoyannis, S. Maltezos, P. Savva, and G. Tsipolitis, *Determination of the ATLAS MDT chambers response to 0.5 to 10 MeV neutrons and development of a simulation model*, Nuclear Instruments and Methods in Physics Research Section A: Accelerators, Spectrometers, Detectors and Associated Equipment **575** (2007) no. 3, 402 – 411.

[41] N. Patronis, C. T. Papadopoulos, S. Galanopoulos, M. Kokkoris, G. Perdikakis, R. Vlastou, A. Lagoyannis, and S. Harissopulos, *Activation cross section and isomeric cross-section ratio for the $(n, 2n)$ reaction on* ^{191}Ir, Phys. Rev. C **75** 034607.

List of Figures

List of Tables